SANDIA REPORT
SAND2004-1267
Unlimited Release
Printed April 2004

Deployable Large Aperture Optics System for Remote Sensing Applications

Jeffrey Martin, Benjamin Macke, John Main, Anton Sumali, Pavel Chaplya, and Jordan Massad

Prepared by
Sandia National Laboratories
Albuquerque, New Mexico 87185 and Livermore, California 94550

Sandia is a multiprogram laboratory operated by Sandia Corporation,
a Lockheed Martin Company, for the United States Department of Energy's
National Nuclear Security Administration under Contract DE-AC04-94AL85000.

Sandia National Laboratories

Issued by Sandia National Laboratories, operated for the United States Department of Energy by Sandia Corporation.

Available to DOE and DOE contractors from
U.S. Department of Energy
Office of Scientific and Technical Information
P.O. Box 62
Oak Ridge, TN 37831

Telephone: (865)576-8401
Facsimile: (865)576-5728
E-Mail: reports@adonis.osti.gov
Online ordering: http://www.doe.gov/bridge

Available to the public from
U.S. Department of Commerce
National Technical Information Service
5285 Port Royal Rd
Springfield, VA 22161

Telephone: (800)553-6847
Facsimile: (703)605-6900
E-Mail: orders@ntis.fedworld.gov
Online order: http://www.ntis.gov/help/ordermethods.asp?loc=7-4-0#online

SAND2004-1267
Unlimited Release
Printed April 2004

Deployable Large Aperture Optics System for Remote Sensing Applications

Jeffrey Martin and Benjamin Macke
Mechanical Systems Design

Anton Sumali and Jordan Massad
Structural Dynamic Development & Smart Systems

Pavel Chaplya
Materials Mechanics

Sandia National Laboratories
P.O. Box 5800
Albuquerque, NM 87185-1152

John Main
Mechanical Engineering University of Kentucky
Lexington, KY 40506-0503

Abstract

This report summarizes research into effects of electron gun control on piezoelectric polyvinylidene fluoride (PVDF) structures. The experimental apparatus specific to the electron gun control of this structure is detailed, and the equipment developed for the remote examination of the bimorph surface profile is outlined. Experiments conducted to determine the optimum electron beam characteristics for control are summarized. Clearer boundaries on the bimorphs' control output capabilities were determined, as was the closed loop response. Further controllability analysis of the bimorph is outlined, and the results are examined. In this research, the bimorph response was tested through a matrix of control inputs of varying current, frequency, and amplitude. Experiments also studied the response to electron gun actuation of piezoelectric bimorph thin film covered with multiple spatial regions of control. Parameter ranges that yielded predictable control under certain circumstances were determined. Research has shown that electron gun control can be used to make macrocontrol and nanocontrol adjustments for PVDF structures. The control response and hysteresis are more linear for a small range of energy levels. Current levels needed for optimum control are established, and the generalized controllability of a PVDF bimorph structure is shown.

This page intentionally left blank.

Contents

Figures

Tables

Acronyms, Terms, and Nomenclature

ACRONYMS

CCD	charge-coupled device
DC	direct current
ESPI	electronic speckle pattern interferometry
GPIB	general-purpose interface bus
GUI	graphical user interface
LBT	large binocular telescope
LFTC	Laser Time Flash Control
LWIR	long-wavelength infrared light
MWIR	mid-wavelength infrared light
NASA	National Aeronautics and Space Administration
NGST	Next-Generation Space Telescope
PID	Proportional Integrator Derivative
PVDF	(polyinylidene fluoride) a synthetic polyimide which exhibits piezoelectric characteristics

TERMS

bimorph	two PVDF layers affixed with epoxy
converse piezoelectric effect	electric charge/field application induces material stresses or strains
direct piezoelectric effect	material response due to direct application of pressures/forces which generates electric charge/voltage
lidar	light detection and ranging
secondary yield	those electrons released from the bimorph surface

NOMENCLATURE

b	width of bimorph mirror
e_{31}	piezoelectric constant

d_{31}	piezoelectric voltage constant along length (meter/volt)
d_{32}	piezoelectric voltage constant along length (meter/volt)
e_{31}	piezoelectric field constant along length (coulomb/meter^2)
h	thickness of PVDF bimorph
mJ	millijoule: 1×10^{-3} joules
mm	millimeter:: 1×10^{-3} meters
nm	nanometer: 1×10^{-9} meters
t_g	epoxy layer thickness
t_p	the thickness of one single layer of PVDF in a bimorph
u_3	bimorph deflection in the 3-direction
x	distance measured along the length of the bimorph
y	distances measured in the direction of bimorph deflection
E_3	electric field applied across the thickness of a piezoelectric material
E_I	energy at which the ascending electron yield curve equals one
E_{II}	energy at which the descending electron yield curve equals one
E_{pmax}	energy of the maximum electron yield
$I(x,y)$	ESPI image pixel location
K	intensity scaling constant for ESPI system
V_{bp}	voltage applied to the electrode of the PVDF bimorph mirror (back pressure)
V_{eg}	voltage applied to the electron gun side of the PVDF bimorph mirror
Y	Young’s Modulus
$Z_D(x,y)$	displaced object position for ESPI system
$Z_R(x,y)$	reference object position for ESPI system
$d(x,y)_{\mathrm{mod}(2p)}$	wrapped phase image for the ESPI system
$d(x,y)$	continuous phase image for the ESPI system
λ	wavelength of light
μm	micrometer or micron: 1×10^{-6} meters

Executive Summary

Global monitoring depends on high-powered telescopes that use giant primary mirrors. The larger the mirrors, the more temperature and gravity can distort and hamper their clarity.

One possible solution is the use of primary segmented mirrors, whose computer-controlled sensors and actuators constantly adjust the relative positions of the segments to counteract the varying effects of temperature, gravity, and atmospheric turbulence that blur light from celestial objects.

Space-based optical systems circumvent such handicaps, but currently mirror size in such systems is limited by the size of the space shuttle launch bay, so that adequate ground resolution cannot be achieved from space. Space-based lidar systems could be used to successfully detect and differentiate between materials over the world's surface, but current limitations in aperture size (50 cm) would necessitate the use of >.2-J laser power, which would be too expensive at this time.

If a 5-m primary mirror were used, however, an off-the-shelf 30- to 40-mJ laser could be readily adapted to space applications. The dilemma would be getting a mirror of that size into space, given launch bay size limitations. The cost of assembling rigid, segmented mirrors in space would be prohibitive because of their large volume and weight, so that ultra-large (>10 m) apertures (mirrors) will likely have to be achieved in the form of deployable thin-skin mirrors, whose resolution and sensitivity will be orders-of-magnitude better than current mirrors.

One of the primary concerns with developing these deployable thin-skin, flexible mirrors is the issue of material controllability: given the material's flexibility, can researchers achieve and maintain the optical tolerances and shape necessary for mirrors in high-powered telescopes. This research examines electron gun control techniques. It will show that within specific parameters these techniques may prove applicable for space applications with the possibility of minor modifications.

Introduction

Global monitoring depends on high-powered telescopes with superior resolution. The resolution of an optical system is proportional to the amount of light it gathers. Therefore, the primary mirrors used in these telescopes must be as large as possible to gather the maximum amount of light.

The clarity of an optical system is related to how far it is within the optical prescription tolerances. Depending on the wavelength being gathered, the surface tolerances typically range from fractions of nanometers to tens of nanometers. In addition, the larger the mirrors, the more temperature and gravity can distort them and hamper their clarity. Therefore, as ever-larger primary mirror surfaces are required for optimal resolution, the manufacture of systems with adequate clarity becomes more difficult.

Primary mirrors are still manufactured by grinding and polishing glass to the correct shape, an expensive process that can take more than a year. The resulting mirrors have a relatively small strength-to-weight ratio, and they are brittle and very susceptible to impacts and vibrations. Currently the largest terrestrial single-cell (single-surface) telescope primary mirror is the large binocular telescope (LBT) built by the University of Arizona, measuring 8.4 m in diameter. Because of the mirror's large size and attendant weight, temperature changes and gravity cause distortions that must be counteracted by controls to maintain the mirror's surface tolerances. The cost of the mirror alone was $8 million; the cost of the completed observatory was $80 million (Clark 1997).

Having reached the practical limits of single-cell technology, segmented primary mirrors have been further developed. The largest is the Keck Observatory on Mauna Kea in Hawaii, built at a cost of $140 million. The mirror itself is made up of 36 individual hexagonal 1.8-m segments. The segments form a single-equivalent 10-m-diam hyperboloid surface that is computer controlled to maintain a near-perfect reflecting surface for gathering starlight. Scientific observations would be impossible without this active correction of the primary mirror. A computer-controlled system of sensors and actuators (precision pistons) adjusts the position of each segment relative to its neighbors to an accuracy of four nanometers. These twice-per-second adjustments effectively counter incremental changes due to temperature and the force of gravity, which bends the mirror support structure on this giant telescope (Keck Observatory 1996).

Like many other giant, ground-based optical telescopes, these systems have reached a point at which adaptive optics are needed to correct for atmospheric turbulence that blurs light from celestial objects. Adaptive optics systems analyze the incoming wavefront distortion caused by the turbulent air above a telescope and adjust optical surfaces to correct for the atmosphere's random disturbances.

Mirrors are already pushing the bounds of science here on earth. The Hubble Space Telescope was launched in 1990 to improve on these earth-imposed limits. Hubble uses a 2.4-m single-cell primary mirror to gather enough visible light to crisply resolve some of the most distant celestial bodies ever seen. The Hubble mirror's size was based purely on the size of the space shuttle launch bay.

Recent events (Isaacson 2001) have brought the world's attention to the need for global monitoring from orbital imaging platforms. As on Earth, optical systems in space need to increase in size, resolution, and clarity. The added cost and complexity of launching a system similar to the Keck Observatory into space and assembling it there would be prohibitive. Other approaches must be investigated if a dramatic improvement in space-based optic systems is desired.

Currently the smallest achievable ground resolution on a commercial satellite is 1 m (Space Imaging, Inc. 1999). At 1-m resolution, a satellite cannot tell the difference between a person and the ground he or she is standing on. As seen in Figure 1, a diffraction-limited optical system would need to be approximately 4 m in diameter to achieve a 17-cm ground resolution (Martin et al. 2001b), which would enable analyses such as counting populations in a given area and searching for people in hiding. A 17-cm ground resolution could enable differentiation between individuals' hair color or clothing. Primary mirror aperture sizes must be increased beyond present bounds to enhance ground resolution for viewing the entire surface of the world.

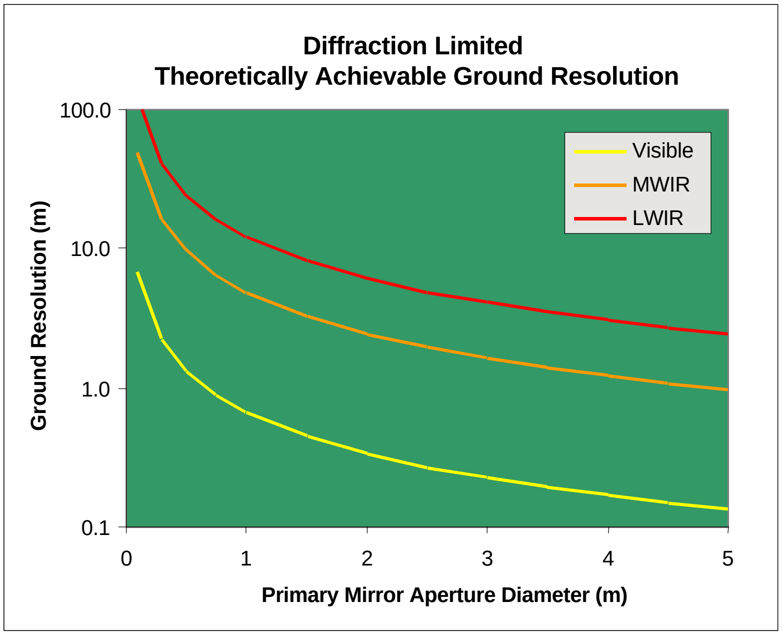

Figure 1. Diffraction-limited ground resolution as a function of primary mirror size. (MWIR: mid-wavelength infrared light. LWIR: long-wavelength infrared light.)

Further, studies at Sandia National Laboratories have shown that lidar (light detection and ranging) systems can be used to remotely detect and differentiate between materials. Analysis has shown that such systems could perform this function from space and search for these materials all over the globe. Unfortunately, given conventional 50-cm aperture capabilities, the required laser power (>2 J) is prohibitive for space applications at this time. A recent examination of this problem using large-aperture optics (a 5-m primary mirror) has shown that lidar could provide ground information with a signal-to-noise ratio of 4:1 (Martin et al. 2001b). This design (see Figure 2) would use an “off-the-shelf” 30- to 40-mJ laser that is readily adaptable to space applications.

Aperture sizes must break the barriers of conventional materials and earth-imposed limits if we are to examine the universe around us more clearly. Maintaining reasonable costs is also a driving factor in the need to package large-diameter primary optics in packages small enough to stow atop a small booster. The immediate goal for NASA's Next-Generation Space Telescope (NGST) program is the development of a primary collector with an areal density of less than 15 kg/m^2. The NASA Gossamer Initiative has a further goal of developing primary mirrors whose areal density is 1 kg/m^2.

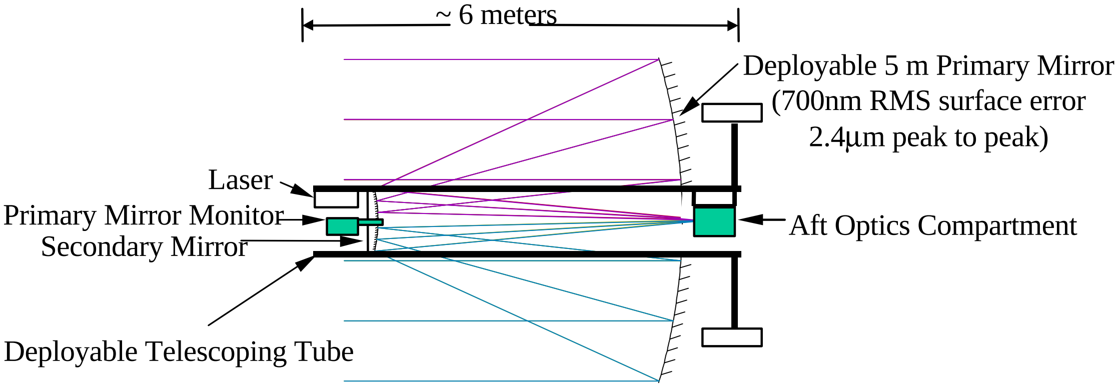

Figure 2. Space-based lidar design concept.

Achieving these dramatic reductions in overall system launch size and mass while maintaining, and even exceeding, present resolution and sensitivity levels may require the development of very lightweight, large-aperture, space-based optics. As mentioned earlier, researchers are considering on-orbit assembly of rigid optical mirror segments to circumvent geometric limitations imposed by launch vehicles while increasing resolution (Bell et al. 1998; Rapp 1996). However, the cost penalties associated with their volumetric and weight constraints limit the aperture diameter to less than approximately 10 m.

Therefore, ultra-large apertures will likely only be obtained by using deployable thin-skin mirror technology (Bell et al. 1998). Such thin films can be compacted for launch and deployed after achieving orbit. For the clearest visual results, active control becomes a necessary component when dealing with deformable optical components, because the mirror could have creases and bumps from the compacting process. One method for achieving active control of the mirror surface uses a piezoelectric material to form the mirror shape. Polyvinylidene fluoride (PVDF), a synthetic polymer thin-film piezoelectric material, has one of the strongest piezoelectric constants of all piezoelectric materials. Furthermore, its flexibility makes it ideal for deformable mirror applications. However, its operating temperature range makes PVDF inadequate for the aerospace environment. Nevertheless, because it is inexpensive and readily available, it was chosen for this work. Elsewhere, research is being done to find other piezoelectric polymers with adequate operating temperature ranges.

Purpose

Ultra-large, deployable thin-skin mirrors can offer an orders-of-magnitude improvement in resolution and sensitivity over what is achievable today (Main, Nelson, and Martin 1998b), yet many technological barriers must be overcome to make this approach a viable alternative for future system designs. Being able to consistently achieve and maintain the optical tolerances and shape of such a large, highly flexible surface is of primary concern and is the focus of this research.

Scope

This report specifically addresses the control response characteristics of thin-film piezoelectric structures subjected to electron flux inputs. A series of experiments were conducted to find the optimal control parameters for electron gun actuation of piezoelectric materials. These parameters optimize the actuation decay rates, hysteresis irregularities, actuation current levels, and actuation energy levels. Further experiments were performed on the materials to characterize their response to different control inputs, such as frequency and amplitude. The macroscale and nanoscale controllability of this approach were also examined. Experiments were also conducted to establish a level of ability to control a PVDF thin film when it has multiple spatial regions of activation. An empirical set of experiments was conducted to study the effects of focusing an electron gun on one region of the thin film to actuate it. In addition, another empirical set of experiments studied the mechanical response of one region as the electron gun was focused onto other regions of the thin film.

Background

Previous Research into Control of Thin-Film Membrane Mirrors

Control of thin-film membrane mirrors has been studied for many years. Research has included applying differential pressures across thin-film membrane mirrors by placing the membrane under vacuum/inflation or applying direct spring forces (Bin-Nun and Dothan-Deutsch 1972; Mikoshiba and Ahlborn 1972) to create a concave/convex shape. Larger versions of these systems have been researched recently (Natori et al. 1988; Utku et al. 1995; Freeland, Bilyeu, and Veal 1996). Difficulties with outer-edge distortions and wrinkling seem to be a major problem with this control method.

Investigations have also been performed on electrostatic thin metallic membranes (Ealey and Wellman 1991) controlled by electrical proximity charges. Results here have shown promise. However, this method has the drawback of needing electrical inputs rather than control surface resolution. Typically, electrodes are placed on either side of the deformable mirror, and a voltage difference is applied to actuate it. Each individual pinhead-size control area needs a control lead, which can cause problems as the number of controllable areas becomes large (Main 1997a). Moreover, this can cause deformation or more “bumpiness” of the thin-film mirror’s surface.

The most promising techniques to date have used piezoelectric materials control techniques (Mikoshiba and Ahlborn 1972; Feinleib, Lipson, and Cone 1974; Adelman 1977; Kokorowski 1979; Steinhaus and Lipson 1979; Sato, Ueda, and Ikeda 1981; Forbes et al. 1989; Ikramov et al. 1992; Rigaut et al. 1994; Susini, Labergerie, and Zhang 1994). Both unimorph and bimorph structures have been investigated for control of mirror curvature as a function of voltage input. The voltage can be used to control the global curvature by means of a single electrode (paired with a ground electrode) covering the entire mirror.Adjustments to the mirror are made through actuating the mirror as a whole (Sato, Ueda, and Ikeda 1990; Susini, Labergerie, and Zhang 1995) or by addressing many smaller areas through the use of discrete electrodes (Feinleib, Lipson, and Cone 1974; Forbes et al. 1989). The present difficulties with these control techniques still relate to their resolution capabilities as a function of control lead wires.

Piezoelectric Basics

A property unique to piezoelectric materials is that material strain induces a buildup of electric charge on the material surface. This charge buildup correlates directly to an electric potential, or voltage, across the material. This effect is known as the direct piezoelectric effect. The converse of this effect, known as the converse piezoelectric effect, is when an applied charge or voltage results in material strain. Both effects have useful applications.

The direct piezoelectric effect is used in sensor applications, such as when a strain gauge is used on a material undergoing strain. When the material is strained, the adhered strain gauge strains, thereby sending a voltage to the strain gauge controller. The controller can then use the relationship between voltage and strain to calculate how much strain the material is experiencing.

The converse piezoelectric effect is used for controls and actuator applications, for example in ultrasound machines. As a doctor moves an ultrasound device over a pregnant woman's abdomen, a block of piezoelectric material in the device vibrates at ultrasonic frequencies in response to the electric signal being sent to it. This converse piezoelectric effect is employed in sending electric signals to thin films to create strain.

Electron Gun Control Basics

Research into electron gun control of piezoelectric materials has increased over the last five years. The earliest known reference is US Patent #3,899,709, held by Patrick Brown and Raymond Sivyer (1974) of EMI Ltd., Hayes, England. This is a control technique whereby charges are deposited on a piezoelectric film using an electron gun for the purpose of acoustic control. No detailed engineering data is available on the work.

Another known work in the public domain was a patent by Hubbard (1992). This patent is for an electron gun control technique that is similar to that of Brown and Sivyer, this time for use as a wavefront sensor. Again, no detailed engineering data is available on the work other than the patent outline and drawings.

The University of Kentucky holds patent #6,188,160 (Main and Nelson 2001), which improves on the earlier control technique. It was found that the film shape could be stabilized when control voltages were applied to the opposite surface from the electron input.

Sandia National Laboratories holds the patent on several actuation and control techniques (Martin et al. 2001c). This patent outlines algorithms and techniques that were developed to create control outputs that allow undesired surface profile inputs to be adjusted to desired surface profiles.

In basic electron gun control, electron guns are used to supply continuous charge to large distributed areas in a number of systems. They have been used for over 60 years. The most common use is in the television. Electrons of three different energies are used to excite a layer of phosphor on the television screen. Each of the three levels of energy excites the phosphor and produces a different color (wavelength) of light. The three electron beams are then scanned across the screen to produce a color image. The science of controlling an electron beam has been perfected over the years by television manufacturers and is therefore not a major part of this body of work.

In electron gun control of piezoelectric materials, the electron gun serves precisely the same purpose as in the television. Unlike the television, where the electrons incident on the front surface of the tube are absorbed by a phosphor layer and quickly reradiated as visible light, electron gun control of piezoelectric materials takes advantage of the fact that piezoelectric materials are dielectrics. Dielectrics accumulate a surface charge when exposed to an electron flux (for an example, see NASA 1994). The charge accumulation remains relatively static upon removal of the electron beam, diminishing very slowly as the charge leaks through the surface.

Conventional piezo elements have electrodes on both external faces. The electric field across the thickness of the material is adjusted through the application of voltages on these electrodes. The net applied voltage across the material induces piezoelectric strains. These strains result in dimensional changes in the material. In electron gun control, electron loss from the surface results in a changed electric field, E_3. This induces piezoelectric strains that are seen through the establishment of piezoelectric bimorph curvature (Martin 1998).

The change in surface charge that results from the collision of the electron with the surface of a piezoelectric material is not as simple as the addition of an electron-size negative charge. An electron is decelerated when it impacts a surface, giving up its kinetic energy to the material. A number of things can happen to that energy, including raising the energy levels of the electrons already present on the surface to the point that they are ejected as secondary electrons (Goldstein and Yakowitz 1977). The number of secondary electrons emitted from a surface due to the impact of a single electron is a function of the energy of the incident electron and the electrode potential (Nelson and Main 2001).

Figure 3 shows a plot of the secondary electron yield for a typical material as a function of the incident electron energy (Bruining 1957; Whetten 1981; and Koshida 1983). The presence of the secondary electron effect gives electron gun control the ability to apply net positive and net negative charges to the surface of the piezoelectric material. In Figure 3, the critical points on the curve, with regard to electron gun control of piezoelectric materials, are the energy of the maximum electron yield (E_{pmax}) and the energy levels at which the electron yield curve equals one (E_I and E_{II}). Applying electrons with energy between E_I and E_{II} is equivalent to applying a net positive charge to the surface facing the electron gun. Charge equilibrium is reached when enough positive charge accumulates on the surface to accelerate the impact energy of the incoming electrons up to E_{II}.

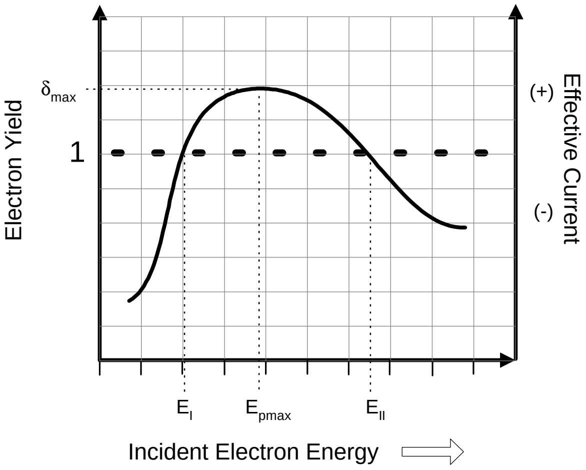

Figure 3. Secondary electron yield for a dielectric.

The approach used in the research described in this report (Main and Nelson 2001) requires only a single-energy electron gun with electron emission energy between E_I and E_{II}. The beam current is used simply to establish current flow between the piezoelectric material surface and the electron gun. The current direction is established by selecting the potential on the other side of the bimorph structure. The incoming electrons "sense" this potential and react by either speeding up above E_{II} (increase in energy level) or decelerating below E_{II} (decrease in energy level). It is this mechanism that is used to cause either large secondary emissions (conventional current toward the piezoelectric material) or little to no secondary emission (conventional current away from the piezo material) (Nelson and Main 2001). The secondary yield is illustrated in Figure 4.

In this method, the electric field is adjusted by varying the potential of the distributed electrode on the surface opposite that of the incoming electrons. Because the current loop is closed only at the location where the electron beam is incident, only that location experiences piezoelectric strain in response to the change in electrode potential (explained in detail in the section entitled "Bimorphs"). This enables direct curvature adjustments of the bimorph. Because the electron gun is used only to close the current loop, point-specific charge adjustments, and therefore curvature changes, can be achieved. This ability to deliver minute charge packets to discrete areas could potentially be used to improve the control flexibility and spatial resolution in active structures.

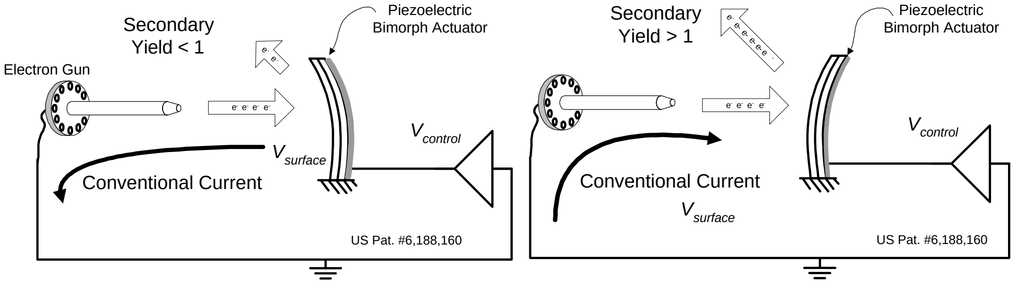

Figure 4. Illlustrations of the conventional current direction as a function of secondary electron yield in electron gun control.

PVDF Research Specimens

PVDF was chosen to function as a shape-controlled membrane mirror for this research. While PVDF may be unsuitable for use in the aerospace environment, it was chosen for this work because it is inexpensive and readily available. Kapton™ is a more stable polyimide for the aerospace environment, but, unfortunately, it has very slight piezoelectric properties.

All piezoelectric materials go through a high-voltage poling process that defines their preferential directions. PVDF is typically stretched along its length during the poling process. This causes its length (or 1-direction) to be preferential. General guidelines for PVDF strain constants are $d_{31} = 23 \times 10^{-12}$ m/V, and $d_{32} = 3 \times 10^{-12}$ m/V (Amp, Inc.). The subscripts refer to a field running perpendicular to a given surface (3-thickness) inducing a strain in the given direction (1-length, 2-width). In piezo materials, the basic material strains to align with electric fields applied through their thickness. These internal strains become evident through measurable changes in the material's dimensions.

Bimorphs

A bimorph comprises two piezoelectric layers epoxied together. When one layer is actuated by applying a positive voltage to one side and a negative voltage (ground/lower voltage) to the opposite side, an electric field is created through the thickness that causes the material to lengthen (or strain positively). If this was reversed and a negative voltage was applied to the positive surface, the material would constrict (strain negatively). The positive and negative surfaces are also referred to as the poles. These poles are predetermined by the materials manufacture and are typically written on the surface by the manufacturer. The bimorphs used in this research are fabricated with the negative surfaces, or poles, epoxied together. This forces one layer to lengthen and the other to shrink in response to the application of any voltage. This design allows the curvature of the bimorph to be manipulated by controlling the electric field across its thickness.

Bimorph Fabrication Process

It is essential to maintain clean conditions, with areas free from lint and oils in which cleaned items can be stored safely, during the manufacture of bimorphs. PVDF is a material with similar adhesion characteristics to Teflon. This means that under the best of circumstances the lamination of two PVDF layers with epoxy can be difficult. Powder-free latex examination gloves prevent oils, which would further hamper the bonding process, from being deposited on the surface of the PVDF. Proper surface preparation must be done in advance.

The first few steps in the fabrication process were performed quite efficiently. The use of two 20-cm square glass plates helped to improve the quality of the finished bimorph. After thoroughly cleansing both PVDF layers and the glass plates with isopropyl alcohol, one of the glass plates was placed on the clean work surface.

The piezoelectric bimorph was made of two 52-µm-thick films of PVDF, oriented so that their poling directions were in opposite directions. Adhering the two strips together was an

~28-µm-thick layer of epoxy, making the overall average bimorph thickness ~132 µm (Figure 5 shows the machine used). Because the bimorph was to be cantilevered, it was made longer than the intended active surface. The extra length was then fixed between two pieces of glass to act as a mount. Excluding the part of the film that was inside the mount, the film was 67 mm long by 22 mm high by 132 µm thick. The outer faces of each PVDF strip were covered with conductive paint to act as electrodes. On both sides of the strip, the entire surface was coated with a conductive paint except for a 1-mm border of clean surface.

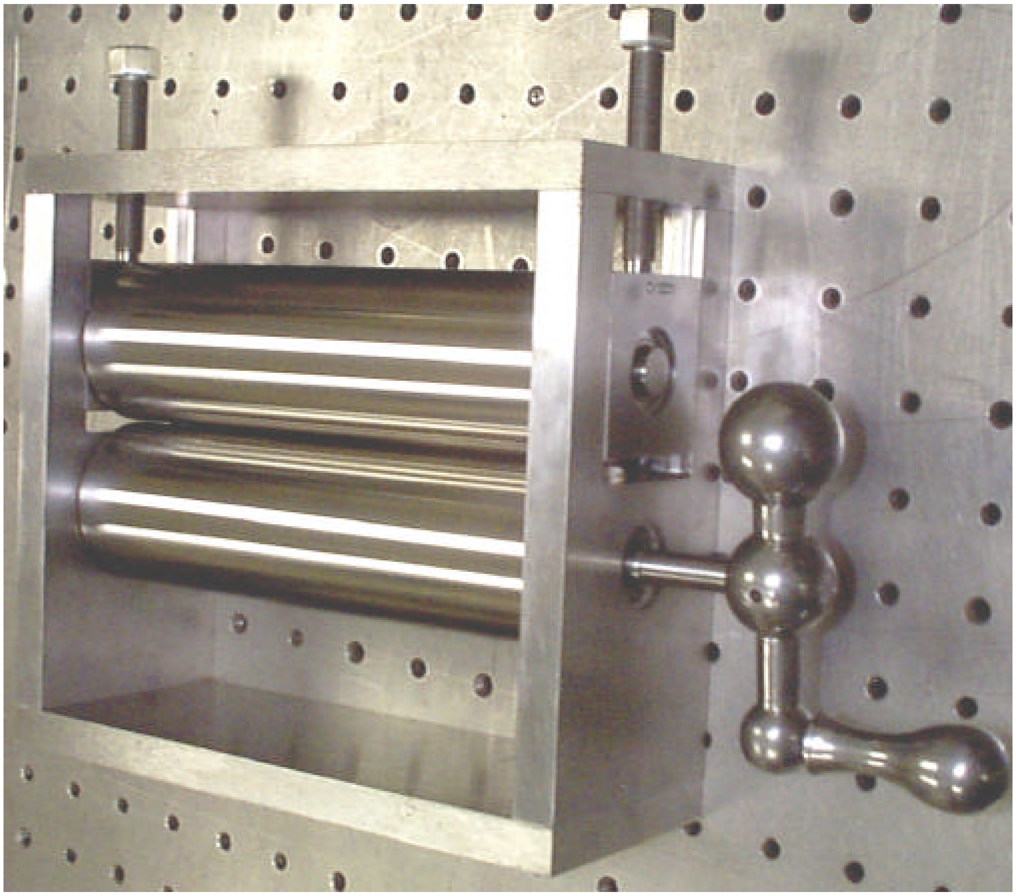

Figure 5. PVDF bimorph laminating machine, designed to make glue layers uniform.

The lamination procedure is very similar to that of mounting strain gauges. Clear tape can be used to attach the end (approximately 6 to 13 mm) of one of the PVDF strips to the glass (being careful to keep track of the bimorph's pole orientation and keeping the negative poles touching). In similar fashion, the second layer should be attached atop the first, with the two layers properly aligned. The second layer should now be folded back so that a bead of epoxy can be applied in the crease.

The smoothing of the two layers is the most important process. Figure 5 shows the lamination machine used to facilitate this process. This system allows for accurate placement of the rollers to create a uniform epoxy layer. For the research described in this report, the machine was set to consistently output bimorphs with a 132-µm thickness. This left 28 µm for the epoxy layer sandwich between the two 52-µm PVDF layers.

For all of the kinds of bimorph specimens used in this research, after the bimorph was removed from the machine, it was carefully cleaned with isopropyl alcohol to remove the excess epoxy residue. After all sides were thoroughly cleaned and dried, the film was mounted between two pieces of glass that would act as the fixed support for the cantilevered film. Glass was used because it is inexpensive, readily available, and an excellent dielectric. The glass-bimorph-glass sandwich was then weighted down. This prevented curl from being established during the curing process.

A picture of the mounting system can be seen in Figure 6. The glass has been colored purple for high visibility and always faces away from the electron gun, toward the chamber view port and the Keyence Laser Sensor. Also, the edge of the bimorph has been artificially colored black in this image using computer software to make it more discernible.

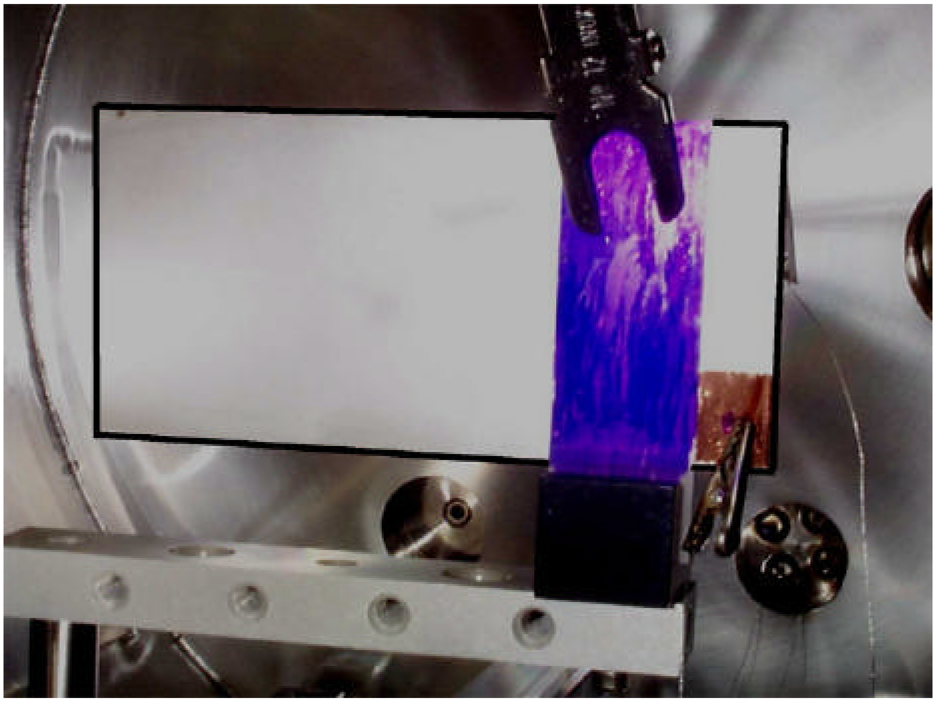

Figure 6. PVDF thin-film bimorph in glass mount.

When the epoxy cured completely, the bimorph remained flat and did not curl. Surface quality was examined carefully. Surfaces with films of light epoxy were polished off using isopropyl alcohol. When the bimorph did not meet the research criteria (if it had bubbles, glue layer irregularities, etc.), it was peeled apart. The leftover epoxy layer was further peeled off, and if no damage had occurred, the bimorph fabrication process was redone.

Several problems in the fabrication process were associated with the quality of the epoxy layer alone. For example, air bubbles in the epoxy made a bimorph unusable in vacuum conditions. A pinhead-size bubble, when placed under high-vacuum conditions (i.e., pressures lower than 10^{-6} Torr) expanded significantly, thereby causing the bimorph to delaminate. This caused the surface to well up, and significant optical distortions resulted. Making a small incision on the opposite side of the optical surface over the bubble relieved this problem. This prevented further expansion under vacuum. Unfortunately, once delamination occured the immediate area did not behave in accordance with bimorph mechanics. Such delaminations caused localized control problems from the loss of the adhesive moment in those areas.

Bimorph Structure and Mechanics

For the purposes of this research it is important to understand that one of the most important concepts related to a bimorph is the orientation of the two layers. The polarization of the two layers in the sample should be opposite one another, so that as one element lengthens, the other shrinks in order to induce bending during piezoelectric control, as mentioned previously. Figure 7 is a cross section of a PVDF bimorph subject to electric field E_3. (The values of the PVDF thickness t_p, glue thickness t_g, total thickness h, and cantilevered length L were given in the previous section.) The figure shows the internal forces that develop from E_3 and the labeled polarization directions of the PVDF strips.

The control voltage is applied to the silver electrode side, and the electrons strike the regions facing the electron gun. The glue causes no internal forces when encountered by E_3 because it is not piezoelectric. However, the internal forces created by the PVDF are a function of the distance from the neutral surface, which for this structure, lies at the center line of the glue layer. This assumes that the bimorph has no initial curvature—if it did, the neutral surface would shift toward the center of curvature of the film.

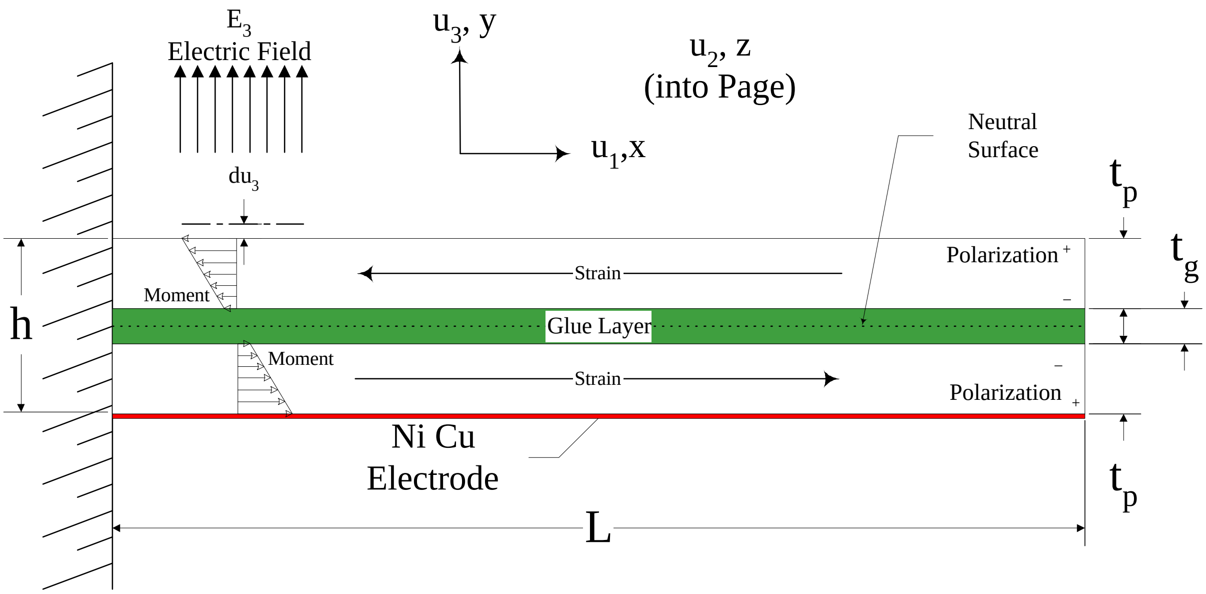

Figure 7. Cross section of PVDF bimorph.

The internal forces created in the PVDF are the same as if a pure bending moment M were applied to the film. The equation for this moment as a function of h, t_g, the film width b (direction going into the page), the piezoelectric constant e_{31}, and E_3 is as follows (Martin 1998):

$$M = 0.25*(h^2 - t_g(x)^2)*b*\mathrm{e}_{31}*E_3(x)\ . \tag{1}$$

It is desirable to see how much transverse deflection $u_3(x)$ can be observed with this bimorph. For a given region, the electric field E_3 is constant (neglecting end effects), and it can be assumed that the glue layer thickness t_g is constant. Transverse deflection can be found by combining Equation (1) with the elementary beam equation

$$\mathrm{d}^2/\mathrm{d}x^2\ [u_3(x)] = M/(\mathrm{Y}*\mathrm{I})\ , \tag{2}$$

where Y is the elastic (or Young's) modulus of the material and I is the area moment of inertia. An understanding of the following basic bimorph equation must be developed before a functional PVDF structure can be developed (Martin 1998):

$$u_3(x) = 1.5*[\mathrm{e}_{31}*E_3*(h^2 - t_g{}^2)/(\mathrm{Y}*h^3)]*x^2\ , \tag{3}$$

where the overall thickness h is found to be

$$h = 2 \cdot t_p + t_g \tag{4}$$

When the epoxy layer is negligible, Equation (3) becomes the following equation, developed by Tzou (1989):

$$u_3(x) = \frac{3}{2} \cdot \left(\frac{\mathrm{e}_{31} \cdot E_3}{\mathrm{Y} \cdot h} \right) \cdot x^2 \tag{5}$$

In Equation (3), all values are known except the electric field strength E_3. If the bimorph were actuated using a known voltage, E_3 could be easily found using the equation for capacitors $E_3 = V/h$. However, in this research, individual electrons are applied to actuate the bimorph. The only way to find the effective electric field resulting from electron actuation is by actuating the surface with electrons and the control voltage, measuring u_3, and then actuating the surface with direct voltages via wire leads until the same u_3 is found. The electric field resulting from direct voltage application can thereby be found; this must be the same electric field as that caused by the electrons on the surface interacting with the control voltage. This information is important for focusing the electron gun beam onto individual regions of a bimorph, as will be shown later in this report.

Equation (6) shows the significant role that the glue layer plays in stiffening the PVDF bimorph beam. In cases where the glue layer is not a substantial factor in the measurement of the bimorph's thickness h (as shown in Figure 7), it can be neglected reliably. Because the PVDF bimorphs used in this research are fabricated from 52-µm-thick sheets, the epoxy layers are a substantial percentage of the overall bimorph thickness; therefore, it is necessary to retain the epoxy layer during calculation.

The basic displacement equation for the case in which both the epoxy layer t_g and the electric field E_3 are uniform is represented by Equation (6):

$$u_3(x) = \frac{3}{2} \cdot \left[\frac{e_{31} \cdot E_3}{Y} \cdot \left(\frac{h^2 - t_g{}^2}{h^3} \right) \right] \cdot x^2 \qquad (6)$$

Experimental Setup

Vacuum System

One constraint for electron gun control of distributed structures is the need for a vacuum. The high temperature of the electron gun element would cause it to oxidize and burn if it were exposed to atmospheric conditions. Most electron guns have an operating pressure lower than 1.0×10^{-6} Torr. It is this rarified atmosphere that prevents oxidation of the gun filament. The basic vacuum setup for this electron gun shape-control research is shown in Figure 8.

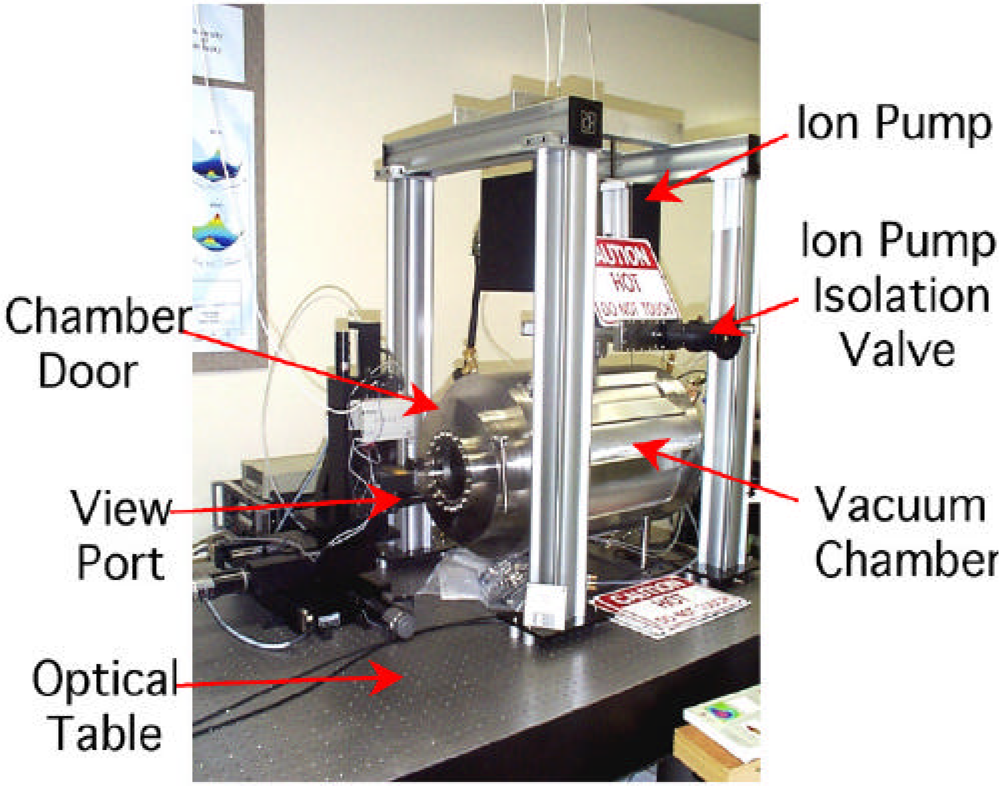

Figure 8. Vacuum system used for thin-film mirror research.

Vacuum Chamber

A stainless steel 0.147-m^3 chamber, rated to hold a vacuum of 1.0×10^{-12} Torr, was used. All fittings were seated using ConFlat flanges with solid copper gaskets to maintain the highest possible vacuum. Access to the experiment between pump downs was facilitated using a 45.7-cm view-port door from Kurt J. Lesker Co. This avoided the tedious removal of the 28 bolts holding down the 45.7-cm flange each time the chamber was accessed.

The vacuum chamber and the optical table are grounded for safety. Grounding the chamber, moreover, serves the second purpose of a secondary electron collector—secondary electrons will be discussed later.

Because PVDF is a pyroelectric material, the chamber was designed with water-circulating channels on its surface. Vacuum chamber temperature fluctuations were minimized through direct water-cooling of the chamber. This dissipated the heat produced during operation of the electron gun.

Observing clean room techniques while working within the chamber prevented contamination. This greatly reduced pump downtime and problems associated with the "virtual leaks" caused by the outgassing of dirt such as fingerprints.

Vacuum Level Measurement

In electron gun control, pressure must remain below the working pressure of the electron gun. An ion gauge is used to accurately measure the pressure within the vacuum chamber. Ion gauges have a working measurement of 1.0×10^{-3} Torr to ultra-high vacuum pressures (1.0×10^{-12} Torr). The element of the ion gauge burns out at higher pressures.

Thermocouples are widely used to measure from an atmospheric pressure of 760 Torr down to 1.0×10^{-3} Torr. A vacuum gauge controller, like the Varian SenTorr, was used to constantly monitor the pressure readings. This controller automatically turned the ion gauge on/off at the correct set-point pressure, preventing damage to the equipment.

Turbo-Roughing Pump Vacuum System

Evacuation of the chamber was done in two stages by the system shown in Figure 9. The initial pump down, or roughing stage, was done using a Varian model DV-2 dry diaphragm pump**.** This model maintained a pressure of 1.0×10^{-3} Torr on the outlet port of the Turbo molecular pump. The Turbo pump, 2nd stage, was a Varian V60 turbo molecular pump. This model was designed to maintain pressures as low as 1.0×10^{-12} Torr in an ideal system.

Ion Pump Vacuum System

Much of the experimental work was done on thin-film mirrors. Vibrations from the turbo pump and the roughing pump caused low-amplitude, high-frequency vibrations that skewed high-resolution data. A 300-L/sec third-stage ion pump, which was manufactured by Varian, was added to the system. This pump was capable of maintaining pressures of up to 1.0×10^{-14} Torr by bonding air molecules to internal cathodes, thereby lowering pressure through nonmechanical means that generated no vibration. When the system reached operating pressures, the chamber and ion pump were isolated, and both the turbo and roughing pumps were removed.

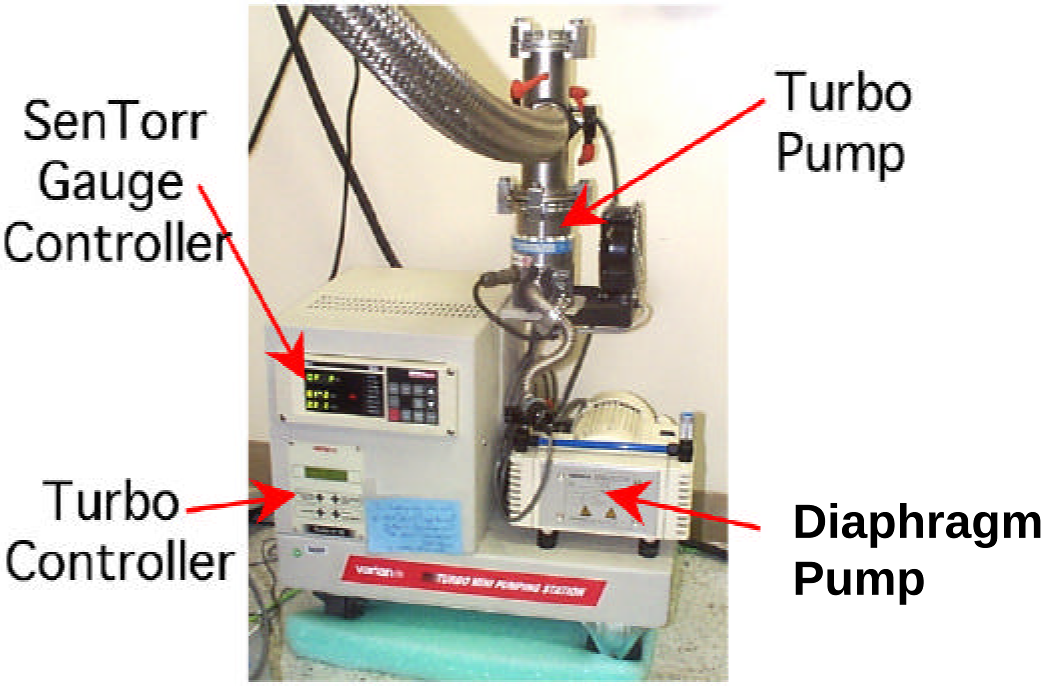

Figure 9. MacroTorr pumping station used for evacuating chamber system.

Electron Gun

Electron gun model EFG-7 (serial no. EFG-7-4690), shown in Figure 10, was manufactured by Kimball Physics, Inc., of Wilton, New Hampshire. This model is capable of placing a ≥1-mm-diam focused electron beam spot, with a variable electron energy range of 400–1500 eV, on any point on the research specimens. This particular electron gun has an operating pressure range of 10^{-5} to 10^{-11} Torr. The electron gun power supply, also manufactured by Kimball Physics, Inc., is a model EGPS-7 (serial no. EGPS-7H-474). This model provided variable energy, focus, source current, and grid voltages.

The beam deflection used a four-pole electrostatic system that, for a 1500-eV electron beam, could also be adjusted in both the x and y directions by a maximum of ±5°. The EFG-7 was designed with a pneumatic actuated Faraday cup option that allowed for instantaneous electron beam current measurements.

The EFG-7 electron gun from Kimball Physics needed seven signals to allow complete computer control of all the electron gun’s operating parameters: energy (beam voltage), current (cathode current), grid, focus, x deflection, y deflection, and Faraday cup actuation (Kimball Physics, Inc. 1997).

The EFG-7 model electron gun achieved an ~1-mm spot size at 800 eV of energy. The settings used to achieve a small spot size for the EFG-7 electron gun are shown in Table 1.

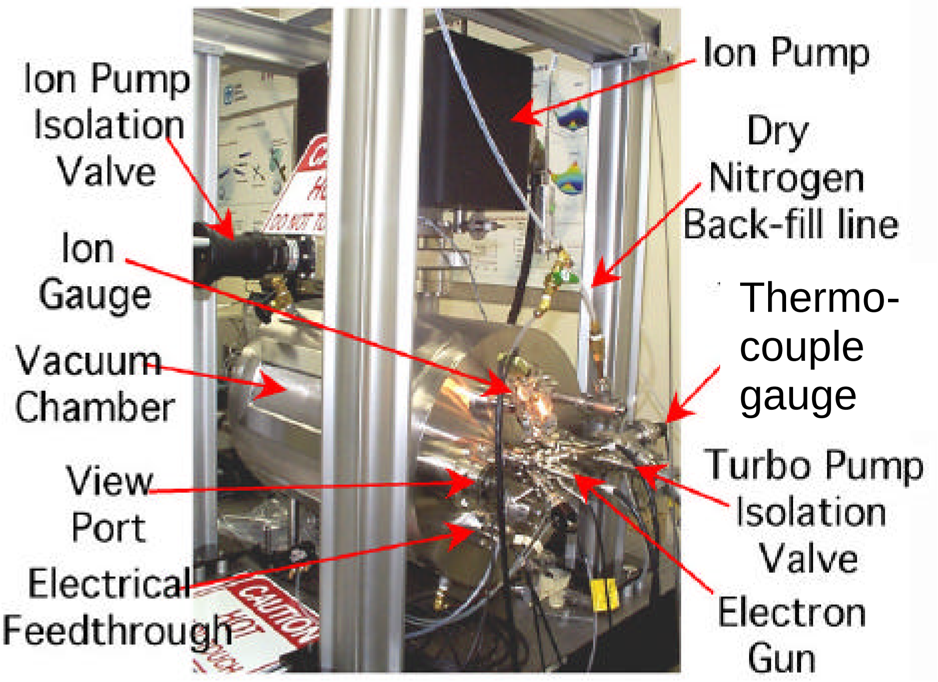

Figure 10. Rear view of vacuum system showing electron gun and equipment.

Support Electronics

The automation of parts of this research required several supporting electronic components, shown in Figure 11. Through a general-purpose interface bus (GPIB) and other control systems (outlined further) all system parameters were adjusted and examined.

Table 1. EFG-7 Electron Gun Settings for a Small Spot Size

Energy (eV)	Current (dial gauge)	Grid (volts)	Focus (dial gauge)	Comments (spot sizes ~1 mm)
1500	9	86	6.502	Small
1400	9	79	6.098	Small
1300	9	74	5.764	Medium small
1200	9	66	5.184	Small
1100	9	60	4.895	Small
1000	9	55	4.408	Small
900	9	47	3.961	Small
800	9	42	3.483	Small
700	9	38	3.001	Small
600	9	29	2.684	Small
500	9	25	2.183	Small
400	9	4	1.880	Large

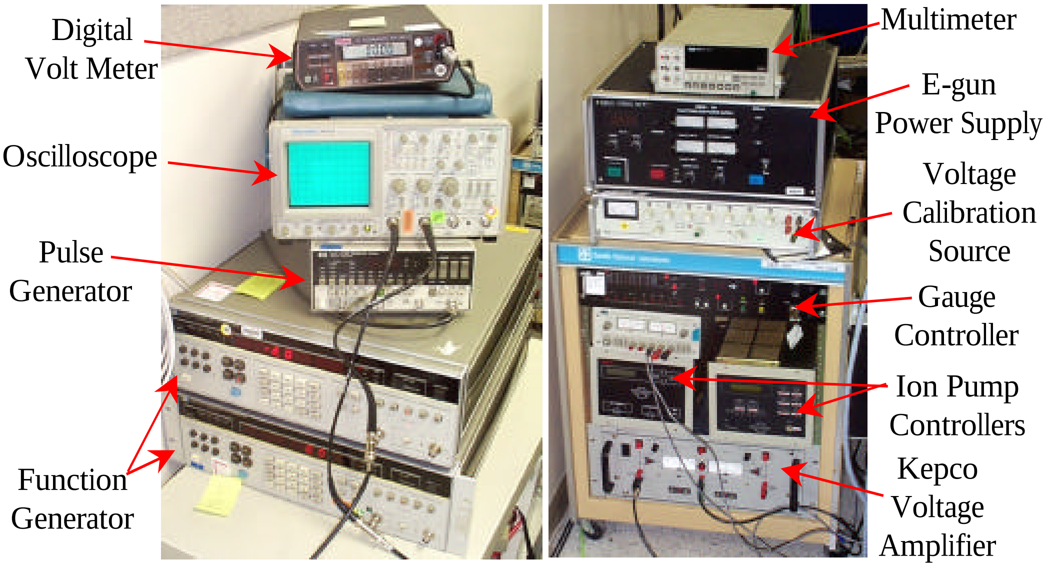

Figure 11. Supporting electronic components used in research.

Power Amplifier

Input control voltages directly applied to the control electrode on the backside of all research specimens were supplied by a bipolar operational power supply: model BOP 1000M, manufactured by Kepco, Inc., of Flushing, NY. This model was able to supply ±1000 V, remotely adjusted by a ±10-V signal input**,** but the operating control voltage range on the film was only –600 to 600 V.

Power Supply

The electron gun power supply (see Figure 11) was used to control all voltages and currents in the electron gun. It was used to set the cathode current, grid voltage, focus voltage, x- and y-deflection voltages, and electron energy.

Picoammeter

A Keithley Model 480 picoammeter was used to directly measure the output beam current from the Faraday cup attached to the electron gun. The cathode current in the electron gun was not an accurate measure of electrons actually emitted from the electron gun, because the vast majority of electrons either hit the interior walls of the electron gun (which was grounded) or were stopped by the grid voltage. Therefore a Faraday cup was placed on the tip of the electron gun and could be controlled to cap off the electron gun for a few seconds to measure the actual electron beam current. Because the stream of electrons heats up the Faraday cup considerably, it could only be used every five to ten minutes. This time limit was only really necessary when finding the proper electron gun settings for focusing on each region of the thin film, when it was vital that the beam current not be great enough to burn a hole in the film. The Faraday cup current was displayed on a picoammeter, shown in Figure 12. Figure 12 also shows the computer workstation for all of the control programming using LabVIEW software.

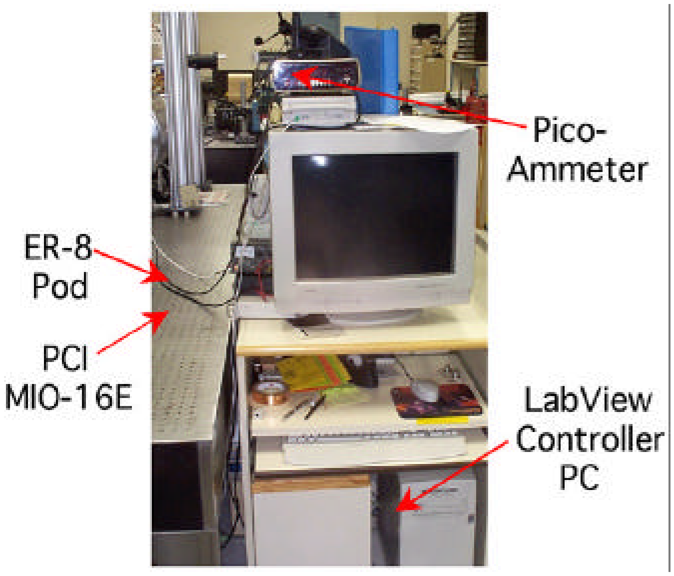

Figure 12. LabVIEW workstation, controller, and Faraday cup picoammeter.

Function Generator

Two Hewlett Packard 3325A function generators controlled the electron beam’s x and y deflections for the purpose of rastoring the electron stream. These GPIB controllable models were capable of producing up to a 10-V amplitude sine wave from 1 MHz to 15 kHz.

Optical Shape Measurement Devices

Noncontact methods of shape measurement were necessary for this work because of the flexible nature of the thin-film structures. Because the research was optical in nature, it was also necessary to perform nanoscale surface characterization at times.

Electronic Speckle Pattern Interferometer

Obtaining optical accuracy from a deployable mirror required a high-resolution sensing system. With traditional interferometry, the number of fringes created across the surface was proportional to the deviation of the surface from the desired shape and the wavelength of light used in the measurement. The surface deviations in these research specimens were too large for conventional interferometers. To analyze these surfaces, an electronic speckle pattern interferometer was used. This technique examined surface profile changes over time and produced a differential surface profile referenced to the original surface profile.

The Electronic Speckle Pattern Interferometer (ESPI) in Figure 13 was developed at Sandia National Laboratories by Bruce Hansche and Mike Valley (Henson et al. 2001).

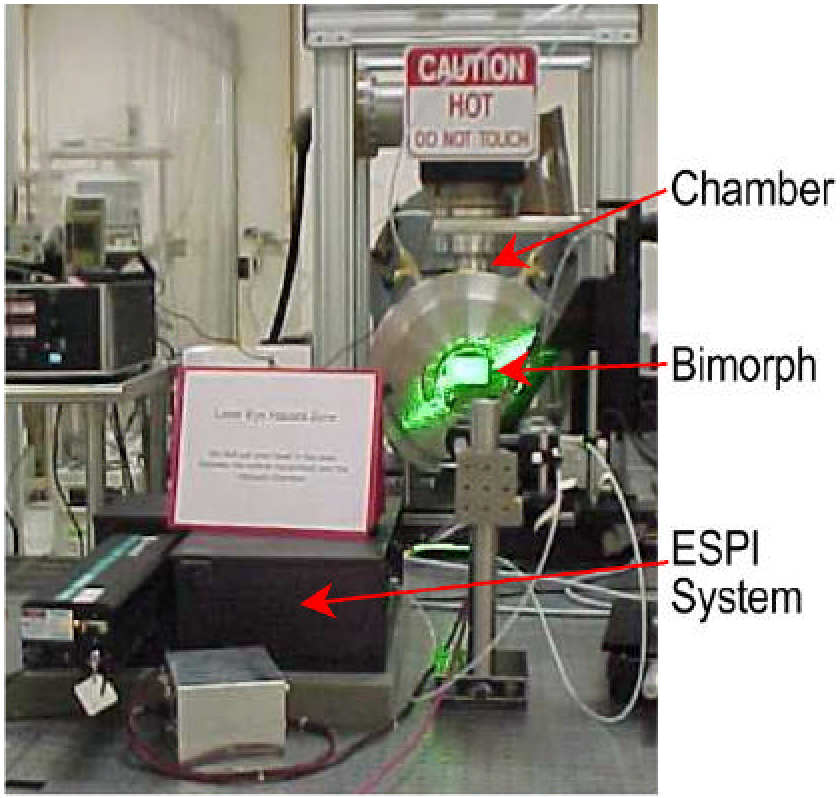

Figure 13. Sandia National Laboratories' ESPI system.

ESPI is essentially a video-based holographic interferometry device, which generates a "wrapped phase" image as its raw data output. That is, for a reference object position $Z_R(x,y)$ and a displaced object $Z_D(x,y)$, illuminated with wavelength l, the image produced is

$$I(x,y) = Kd(x,y)_{\mathrm{mod}(2p)}\ , \tag{7}$$

where

$$d(x,y) = (4p\ /\ l)(Z_D(x,y) - Z_R(x,y)) \tag{8}$$

and K is an intensity scaling constant. This equation assumes illumination and viewing directions essentially normal to the displacement direction.

The wrapped phase image must be "unwrapped" by adding multiples of 2π at the "wrap boundaries." This process converts $d(x,y)_{\mathrm{mod}(2p)}$ to a continuous $d(x,y)$. Multiplying by $[(4\pi/\lambda)/K]$ converts the continuous phase map to a deformation map.

The mirror surface can initially be any shape because measurements are referenced to the initial shape and not to an ideal shape as in traditional interferometric techniques. ESPI is a whole-field technique, allowing measurement of the entire surface simultaneously. This approach offers very high sensitivity, easily measuring deflections on the order of 100 nm, with a theoretical limit approaching 1 nm. This technique has greatly aided the study of surface shape changes initiated by electron gun excitation.

Surface Displacement Mapping System

A coarse sensing approach was used in which a Keyence LK-2500 laser displacement sensor was mounted on a precision Newport stage system. The Keyence sensor provided an absolute measure of the surface position at a single point. Full-surface profiles were obtained from a point-by-point scanning of the sensor over the sample surface. Figure 14 shows the Keyence sensor on the Newport translation stages.

This profiling system was used to measure the absolute change in the mirror shape as a function of electron gun energy and bimorph mirror electrode potential. It was also used to provide real-time tip displacement in a closed-loop shape-control experiment.

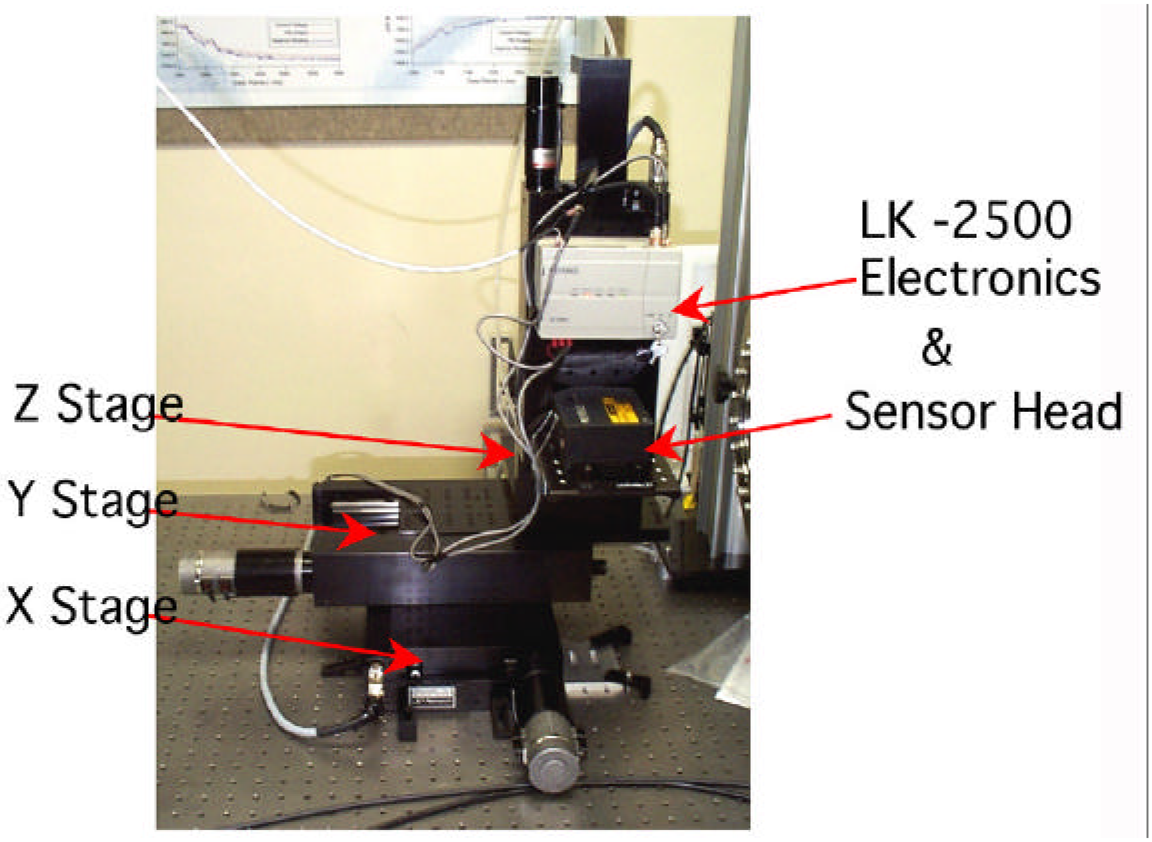

Figure 14. Laser triangulation system. A Keyence sensor was mounted on a Newport stage system.

Displacement Sensor

The LK-2500 uses triangulation measurement principles to measure the perpendicular translation of a point in space. A semiconductor laser beam was reflected off the target surface and passed through a custom-designed receiver lens system that approximated a pinhole. The laser beam passed through the "pinhole" and focused on a linear charge-coupled device (CCD) sensing array. The incoming angle was calculated based on the normal distance from the pinhole to the CCD (which was fixed) and the distance to the laser's crossing along the CCD (which was variable). Using similar triangles and the known point of origination of the laser within the sensor, the distance to the target was triangulated. Displacement changes relative to the LK-2500 sensor head induced position changes of the reflected beam on the CCD array. These positional changes were analyzed by the LK-2500 controller, which resolved positional changes of 10 µm at distances of 250–750 mm. The Laser Time Flash Control (LFTC) facilitated this accuracy regardless of target surface wetness, color, or angle of orientation to the sensor. This large range (5 cm) and high resolution (10 µm) greatly improved the measurement capabilities over those of previous research measurement techniques (Martin 1998).

The LK-2500 includes a Class II red semiconductor laser with a 0.3-mm visible beam spot that easily measures tiny targets and simplifies setup and alignment. Analog outputs of ±5 V, ±10 V, and 4 to 20 mA may be specified. The LK-2500 also performed detection into an enclosure through a glass window as needed to interrogate electron gun controlled films mounted in a vacuum chamber. The laser displacement sensor was capable of sampling at 977 Hz and could therefore be scanned rapidly over a sample to completely map the surface.

Three-Axis Mechanical Stage

The Keyence Laser Sensor measures the transverse displacement at a discrete location along the bimorph's length. As shown in Figure 15, the laser signal sent by the sensor into the chamber bounces off the sample at nearly all angles. However, only the photons bouncing off at a certain angle will make it back to the sensor window, thus allowing the sensor to determine how far away the sample is at that location. To measure the entire contour of the film, then, one would have to measure the location of every point on the film. Because the film shape is always receiving or losing electrons on the surface, the film's entire contour cannot be measured *at one time* in this manner.

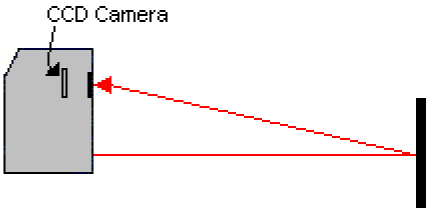

Figure 15. Keyence Laser Sensor striking its target.

However, it is possible to measure the film contour over a period of time. The Keyence sensor's x, y, and z motors are connected to worm gears that move the x, y, and z stages in their respective directions (Figure 14). The precision Newport three-axis translation stage has a positional accuracy of 0.1 µm in the x, y, and z directions, with a 10-cm range. The stages are commanded by means of GPIB controls that scan the Keyence sensor in a 1-mm two-dimensional grid across the bimorph mirror to obtain a surface profile.

Control Systems

Two separate systems were designed and fabricated to enable autonomous experiments. These systems were able to maximize experiment run time by minimizing operator intervention.

National Instruments/LabView Digital Controller

A 600-MHz PC, LabView 5.1 programming language, a National Instruments PCI-6713 A/O board, a PCI-MIO-16E-1 A/I board, an AT-GPIB board, and an ER-8 servo pod were used to develop an easily programmed automated control system. This system (shown in Figure 16) was created to remotely control and take data from the electron gun power supply, KEPCO BOP-1000M power amplifier, Newport precision x-y-z staging system, Keithley 480 picoammeter, and two Hewlett Packard 3325A function generators. Many programs were developed for this body of work.

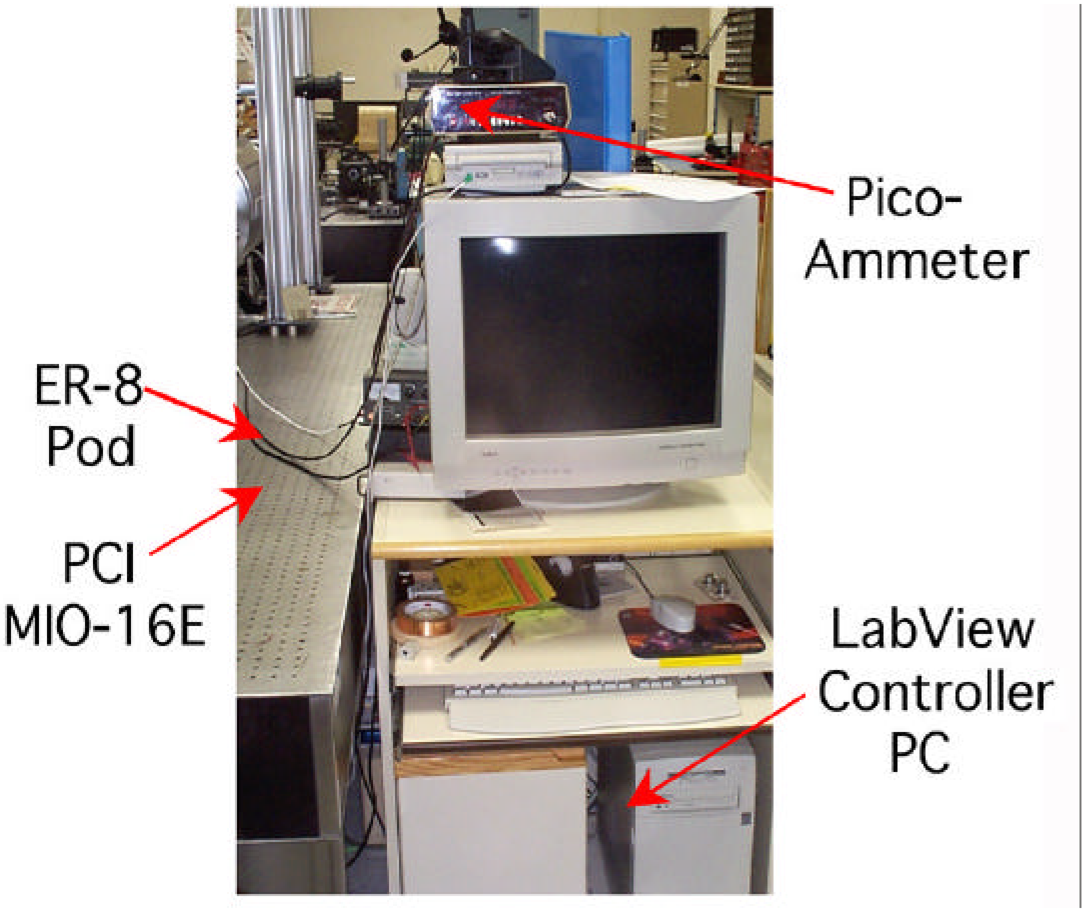

Figure 16. LabView controller system used for research.

A black-and-white camera controlled by National Instruments IMAQ software for LabVIEW programming software and a newly-developed system control program, also created using LabVIEW, were used for the spot location experiments in this report.

dSPACE Digital Controller

Remote operation of the control voltage was performed using a dSPACE six-output-signal processing board and a 32-input-signal processing board interfaced with an 800-MHz Pentium III computer running both Matlab® and Simulink® software. A special Simulink® code was developed specifically to adjust control voltage output synchronized with reading displacement measurements. Control was further developed and refined through the use of special dSPACE control center software programs created for this purpose. This system is shown in Figure 17.

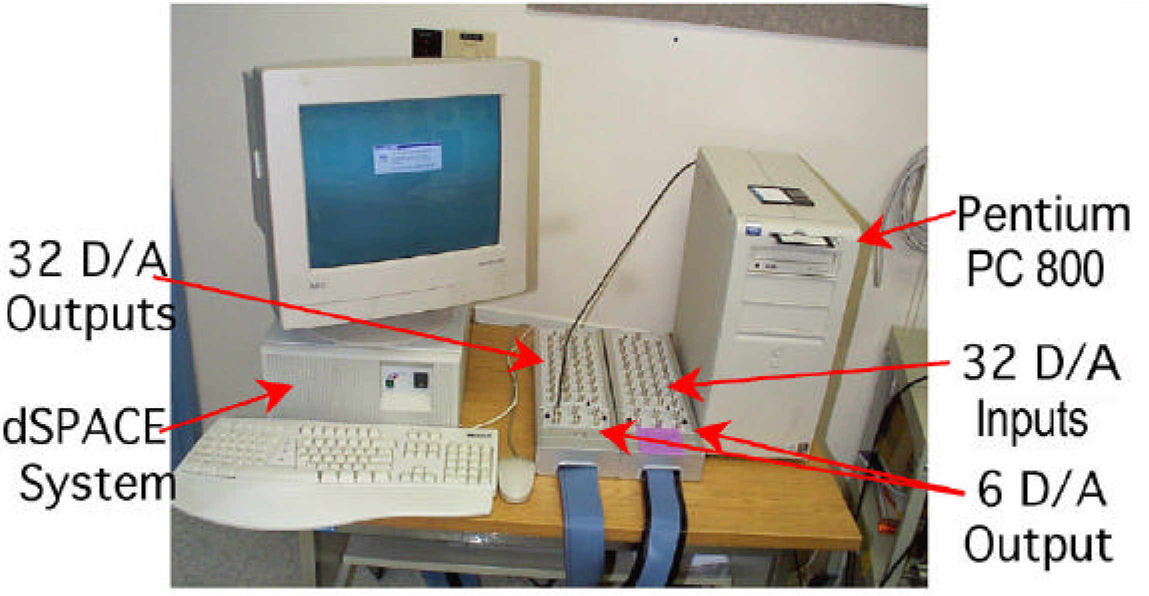

Figure 17. Matlab Simulink and dSPACE controller system used for research.

PVDF Research Specimens

Several bimorphs of differing configurations were used to facilitate this research. All the bimorphs were fabricated from two bonded pieces of poled PVDF, as outlined previously. Each bimorph was bonded with the negative poles toward the bonding layer, purchased from Amp Incorporated of Valley Forge, PA. Any applied voltage induced a positive strain in one layer and a negative strain in the other layer. The design allowed the curvature of the bimorph to be adjusted by controlling the electric field across its thickness.

Type A Bimorph Specimen

The initial portions of the research described in this report were performed using a Type A bimorph. In this configuration, one layer of the bimorph was fabricated from a sheet of plain PVDF without electrodes. The second layer was fabricated from a sheet of PVDF that had a silver ink electrode on the positive face. This electrode, known as the Control Electrode, was used to apply control voltages to the surface of the bimorph with the Kepco power amplifier. Conductive copper tape was used to connect the power amplifier lead to the control electrode with an alligator clip. Figure 18 shows a used Type A bimorph specimen. The silver of the control electrode was “aged” over time by a combination of normal electron radiation exposure and oxidation of the silver electrode. A band of the silver electrode was not aged. This was protected by the location of the glass slides used for electrical isolation purposes in mounting. Type A bimorphs were 12 × 6 cm with an average thickness of 132 µm. A 9-cm segment of the bimorph was cantilevered out from between the glass slides for mounting purposes.

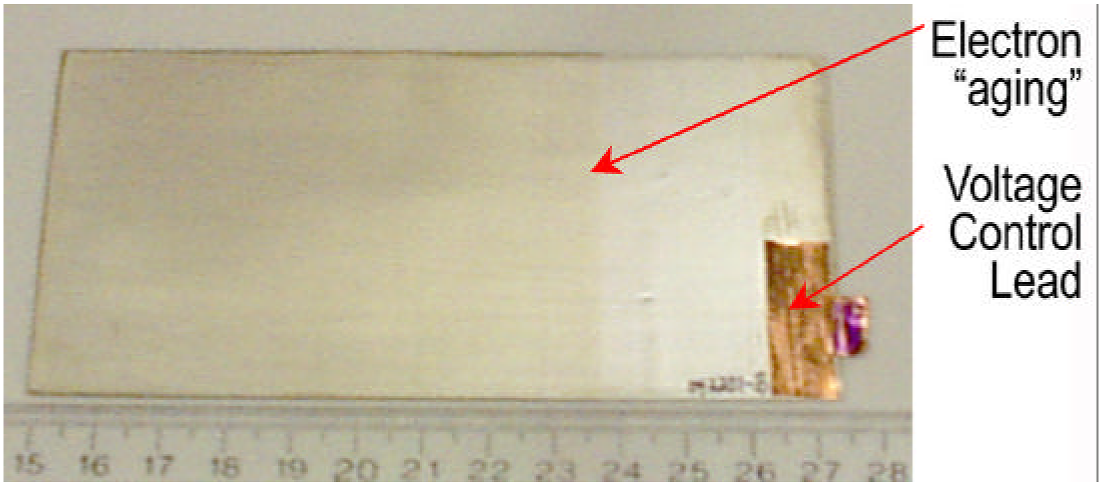

Figure 18. Finished PVDF Type A bimorph.

Type B Bimorph Specimen

The bulk of this research used Type B bimorphs. This configuration differed slightly from the Type A bimorph. The construction in this bimorph used two pieces of PVDF with silver electrodes on the positive faces. Incident electrons spread out across the silver electrode facing the electron gun (or pixel electrode) because of repulsive forces. This maintained an even charge distribution across the entire surface of the bimorph. This even charge distribution, when referenced to the applied voltage on the opposite silver face (the control electrode) created a uniform electric field through the thickness of the bimorph.

An experiment was performed to show this relationship between a Type A bimorph, with a bare face, and a Type B bimorph, with a pixel electrode. When there was no pixel electrode (the surface was bare) the electron gun spot sizes were the critical factor in determining the resolution of the system. With a pixel electrode, the beam spot size needed only to be smaller than the electrode for the control surface resolution to become the pixel electrode size.

In this demonstration, first a Type A, then a Type B bimorph were discretely actuated by 800-eV electrons and 200 control volts from 30 cm away, as diagramed in Figures 19 and 20. The electron beam steering was set to hit the 1-cm position near the cantilever base of the bimorph. The electrons were turned on for just one second with the control voltage set to 200 V. The tip deflection was then recorded.

The control voltage was then changed to 0 V and the electrons were turned back on. The beam steering was used to swipe the 800-eV and 0-V control along the entire bimorph, bringing the bimorph back to a stable reference position. The electrons were then turned off, the control voltage was changed back to 200 V, and the electron beam steering was used to aim at the 2-cm position. The electrons were again turned on for one second, with the control voltage still set to 200 V. Once again the tip deflection was recorded and the bimorph was set back to the reference position.

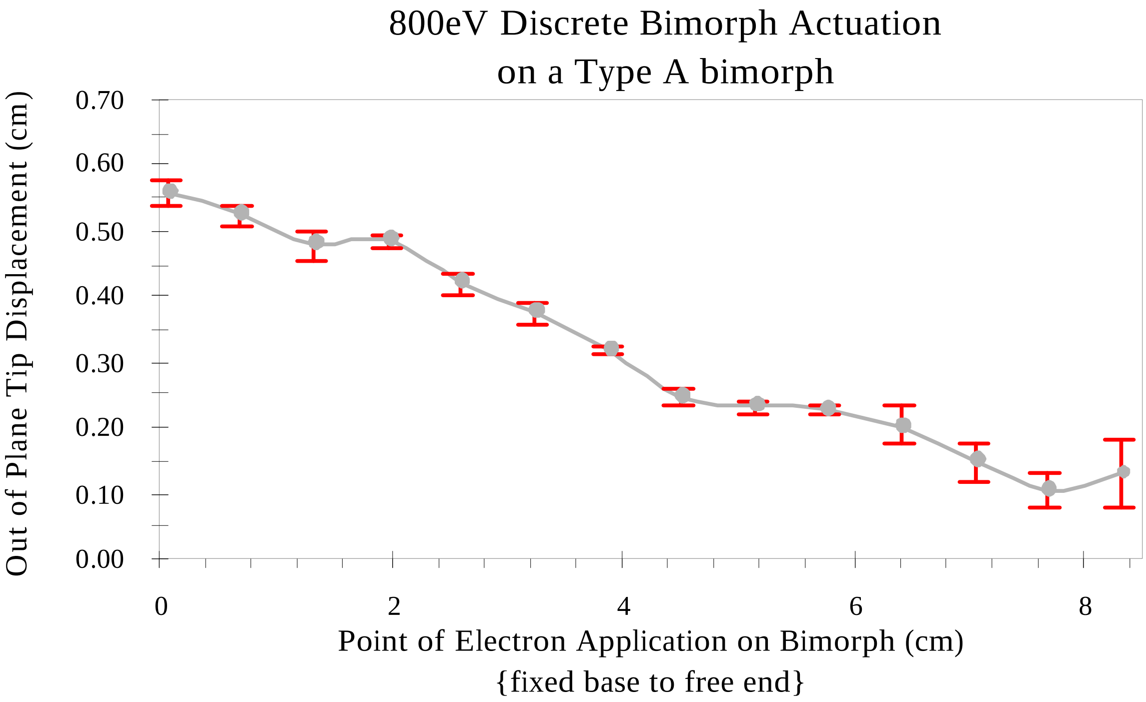

Figure 19. Plot of tip deflections during discrete actuation of a Type A bimorph.

These steps were repeated for several locations along the bimorphs. The tip deflection data for both the Type A and the Type B bimorph were then plotted as a function of the location of the electron beam incidence along the bimorph. As shown in Figure 20, when the bare PVDF (Type A bimorph) was actuated, the tip deflection was dependent on the location of the incident electrons (Martin 1998). However, Figure 21 shows that when the incident electrons on the silver PVDF (Type B) were located anywhere along the bimorph surface, the deflections remained constant. This showed that a Type B bimorph has a uniform electric field regardless of the location of the applied electrons.

Type C Bimorph Specimen

Figure 21 pictures a Type C bimorph. This bimorph was a smaller (therefore more stiff) version of the Type B bimorph with dual silver electrodes. The dimensions of the Type C bimorph were 6.5 cm × 6 cm with an average thickness of 132 μm. Three centimeters of the bimorph were cantilevered out from the glass slides.

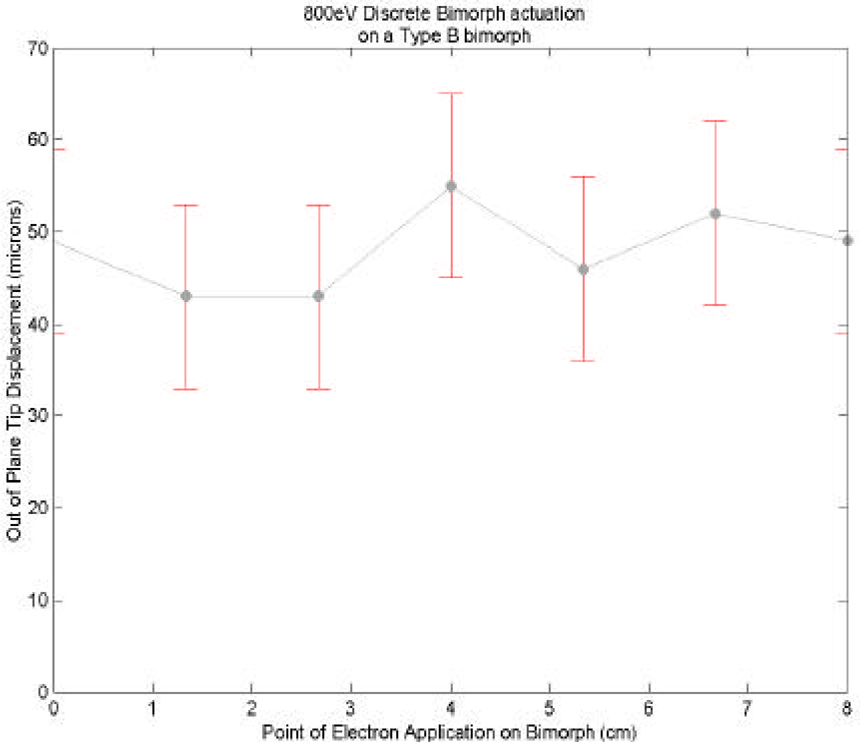

Figure 20. Plot of tip deflections during discrete actuation of a Type B bimorph.

As with the other types of bimorphs used in this research, excluding the part of the film that was inside the mount, the Type C bimorph used film measuring 67 mm long by 22 mm high by 132 µm thick. The outer faces of each PVDF strip were covered with conductive paint to act as electrodes. On the side facing away from the electron gun (hereafter referred to as the backside), the entire surface was coated with a conductive paint, except for a 1-mm border of clean surface. On the side facing the electron gun (hereafter referred to as the front-side), the surface was coated in the same manner as the backside of the other bimorphs used in this research, but here the conductive paint was divided into six equal regions along the length of the film (see Figure 24). In order from the fixed support, the regions were labeled Region 1, Region 2, Region 3, Region 4, Region 5, and Region 6, where Region 6 was the closest to the free end. However, Region 6 was not studied in this research and is not discussed further.

Type M Bimorph Specimen

The Type M bimorph specimens were then uniquely treated: the backside of each was coated with conductive silver paint like the other bimorphs used in this research, but for these bimorphs the conductive paint was divided into six equal regions along the length of the film (see Figure 22). Each conductive region was 10 mm long by 20 mm high, with a 1-mm gap between each region and a 1-mm border around the edges of the film. The border and the gaps were made by wiping off the silver paint with acetone. To achieve straight edges, Kapton^{TM} tape was used as a mask to protect the silver paint that was to remain.

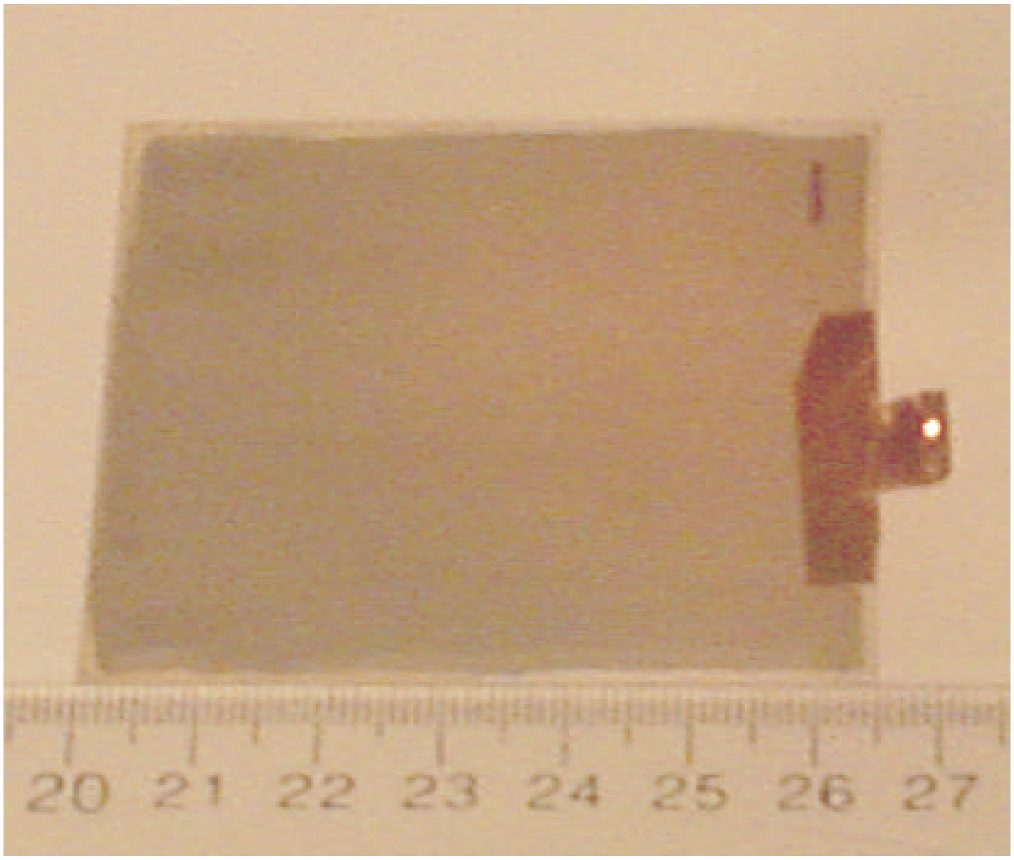

Figure 21. Sample Type C bimorph used for controllability experiments.

Copolymer

A copolymer is a piezoelectric material with approximately equal one- and two-direction (length and width) strain constants. In this case PVDF is poled with equal tension all the way around. This material has piezoelectric strain constants of $d_{31} = d_{32} = 15 \times 10^{-12}$ m/V.

Type D Copolymer Specimen

A Type D copolymer configuration was also used in evaluating electron gun shape control. A piece of a sheet of 52-µm-thick PVDF copolymer was clamped as a single layer in a 29-mm ring mount (see Figure 23). In the ring clamp configuration, these specimens tended to bow out equally, forming a more convex or more concave shape when referenced to the original shape (see Figure 24). The 20-cm × 30-cm × 52-µm specimens were purchased from Ktech Inc. of Albuquerque, New Mexico.

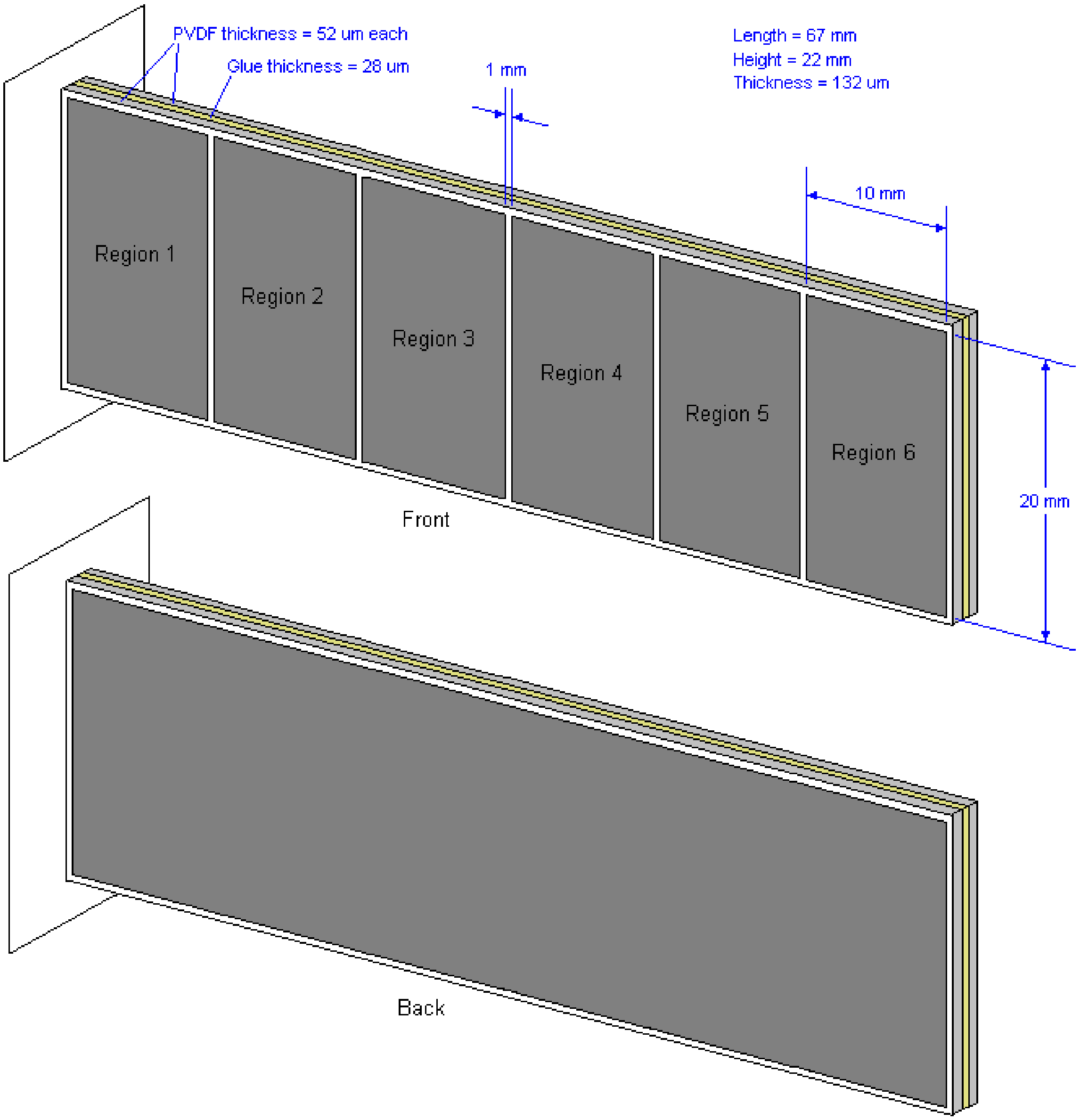

Figure 22. Front and back isometric views of the Type M PVDF thin-film bimorph.

Figure 25 shows a schematic of the top view of the setup used in this research, and Figure 8 shows a picture of the actual setup (Martin 2001). The figures show the vacuum chamber, chamber door (for accessing the vacuum chamber interior), thermocouples (for measuring pressure), nitrogen supply line (for refilling the chamber when making alterations or repairs), ion gauge (for measuring pressures below 1.0E-4 Torr), ion pump and ion pump valve (for rapid reduction of pressure that is below 5.0E-6 Torr), electron gun, laser displacement sensor (for measurement of the film), and x, y, and z stages (for moving the laser sensor).

Figure 23. PVDF Type D copolymer mounted in a 29-mm ring clamp.

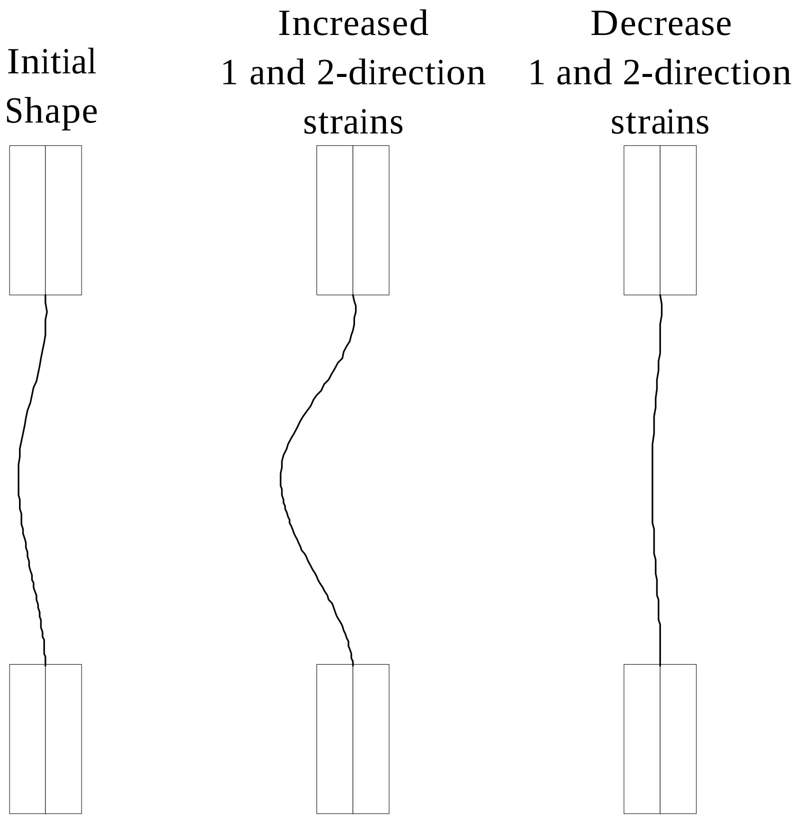

Figure 24. Diagram of the mechanics of Type D copolymer sample.

The vacuum chamber and the optical table are grounded for safety; the grounded chamber, moreover, serves a second purpose as a secondary electron collector—secondary electrons will be discussed later.

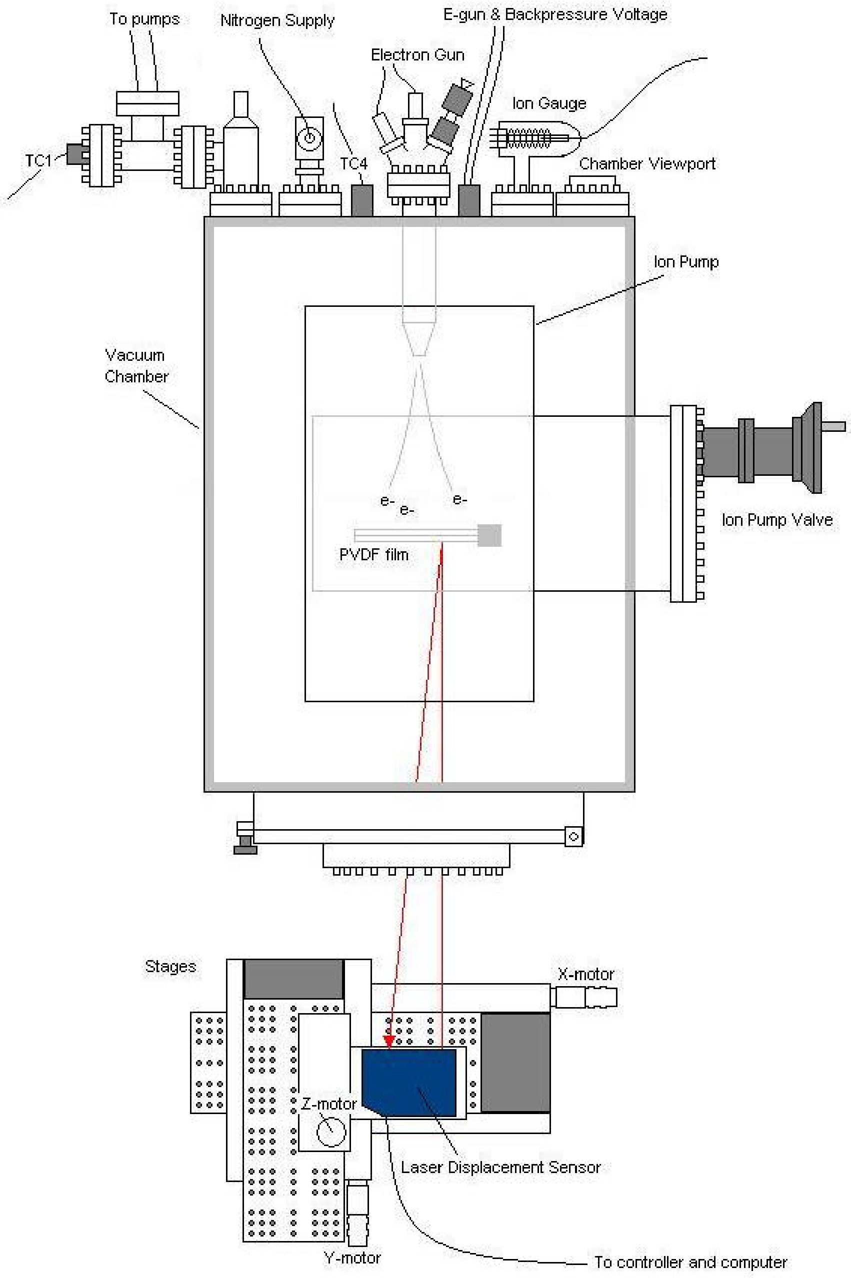

Figure 25. Electron gun controlled PVDF thin-film bimorph system.

Experimental System Overview Summary

The overall system connection diagram for the computer-controlled electron gun research is shown in Figure 26. In this diagram the thick dotted blue lines represent data connections. The thin solid black lines are control connections. The large red dashed lines represent the

Keyence displacement sensor laser. The dashed-dot magenta line shows the lines of GPIB communications.

The computer system controls the power amplifier, the electron gun controller, the X and Y function generators, the x, y, and z stages, and the ER-8 servo pod. The function generators control the X and Y steering of the electron gun controller. The electron gun controller is used to control the current, energy, size, and trajectory of the electron beam. The electron gun sprays electrons on the Pixel Electrode of the bimorph. The servo pod controls the Faraday cup position (in path of electrons, out of path of electrons). When the Faraday cup is in position to read the electron current, the current flows to the Keithley picoammeter and is then read by the computer. The power amplifier applies the control voltages to the control electrode on the bimorph. Displacements of the bimorph are then read by the Keyence sensor and passed directly to the computer system. The x, y, and z stages control the spatial position of the Keyence sensor. The position of the Keyence sensor controls the point being measured on the bimorph.

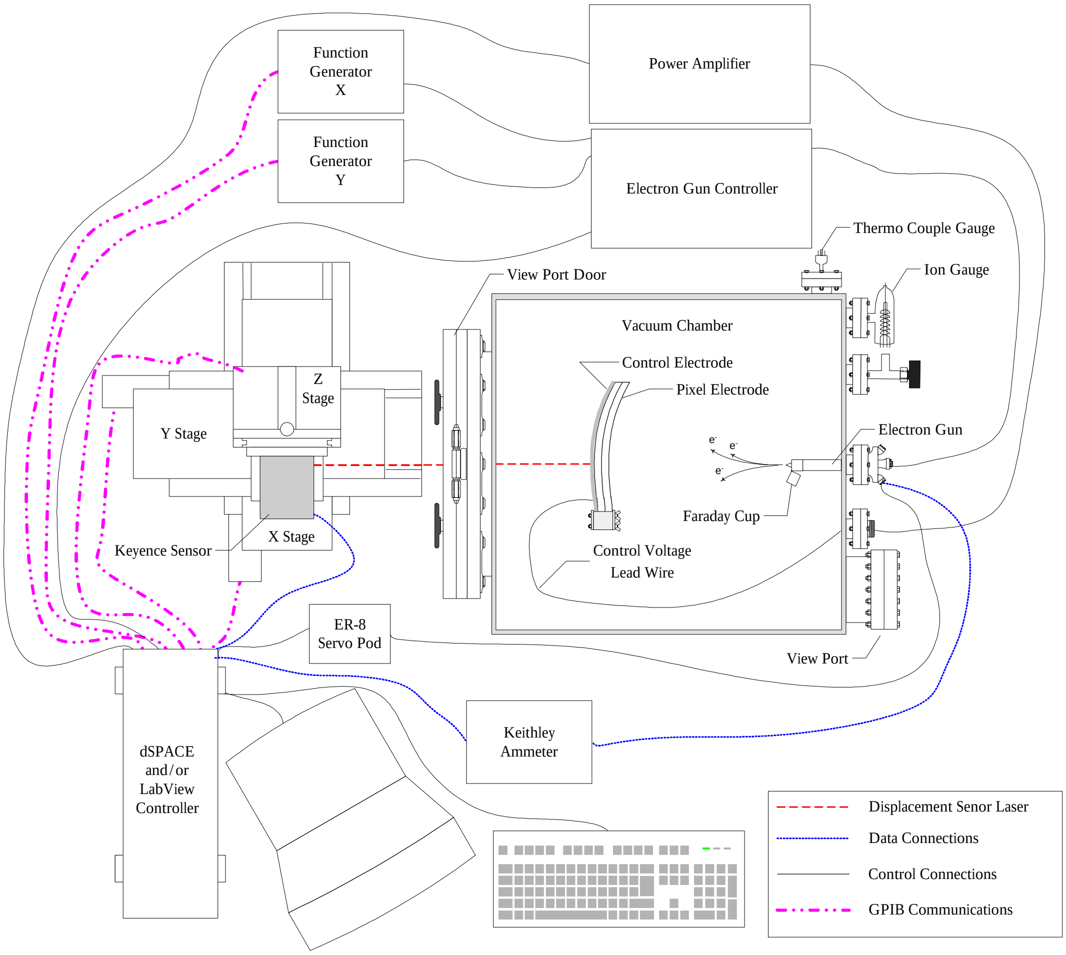

Figure 26. Diagram of computer-controlled connections for electron gun experimentation.

A summary of the research specimens used in this research is shown in Table 2. Note that there is only one copolymer specimen. This specimen was used solely for the purpose of coarsely characterizing the ability to induce nanometer-level surface changes with electron gun control. The ESPI measurement system cannot produce static surface displacements of vibrating surfaces. Because the Type A, B, C, and M bimorphs are prone to vibrational disturbances, the Type D copolymer specimen was designed to be stable at a nanometer measurement resolution. The fixed boundary condition all the way around reduced the vibration noise to acceptable levels for the ESPI system.

Experimentation

Electron gun control was previously shown to be a functional actuation technique for piezoelectric bimorphs (Martin 1998). Characterization and optimization of controls are examined in the first part of this section. Table 3 outlines the experiments performed in this portion of research. Each experiment's variables are defined.

Table 2. Summary of Research Specimens

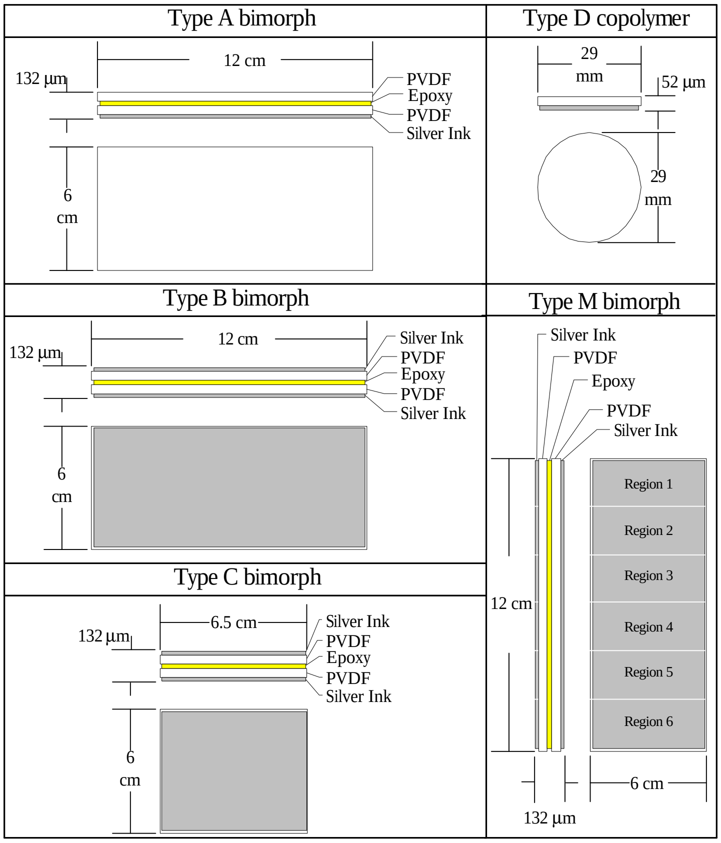

Bimorph MacroControl Analysis

The mirror profile was measured for various electron gun energies and electrode potentials on a Type A bimorph. This was done to analyze the interaction of the electron gun with the bimorph mirrors and to determine the most efficient gun energy level to use in the system as well as to characterize the maximum displacement outputs. This experiment used several different electron energy levels (400, 600, 800, 1000, 1200, and 1400 eV) and control voltage levels between ±600 volts. Each Type A bimorph was mounted between two glass plates (purple) in the vacuum chamber 30 cm from the electron gun, as shown in Figure 27. An 800-eV beam in a 1-mm spot was scanned at 150 Hz in the horizontal direction and 300 Hz in the vertical direction. This beam was used to uniformly excite the bimorph in conjunction with control voltages applied in increments of 100 V starting at zero, going up to 600 V, then down to –600 V, and then back to zero again. At each voltage the bimorph was allowed 5 minutes to reach steady state. At steady state, the Keyence displacement system (outlined previously) was used to take the entire surface profile of the bimorph.

Table 3. Outline of Experiments and Their Variables

	Experimental Specimens				
Experiment Performed	*Type A bimorph*	*Type D copolymer*	*Type B bimorph*	*Type C bimorph*	*Type M bimorph*
Characterization of the control range. Induced displacement as a function of control voltage.	**X**	**X**			**X**
Characterization of the closed-loop control actuation response time to electron secondary emissions from bare PVDF and silver ink.	**X**		**X**		
Optimization of control induced displacement as a function of:					
Electron energy level	**X**		**X**		
Control voltage			**X**		**X**
Electron beam current			**X**		
Characterization of control actuation decay rates as a function of control energy level.			**X**		
Optimization of control displacement hysteresis as a function of control energy level.			**X**		
Characterization of control displacement response as a function of:					
Control voltage frequency				**X**	
Electron beam current				**X**	
Control voltage amplitude				**X**	**X**

Figure 28 shows these data at 800 eV, actuated with ±600 and zero control volts. The data were referenced to an 800-eV and 0-V profile. The direction of motion of the deflection is relative to the Keyence sensor. Negative deflections are deflections away from the Keyence sensor and toward the electron gun in this setup. The 600-V control produced approximately –640 µm of deflection, and –600 V produced approximately 640 µm of deflection at the tip (68 mm from the cantilever). This caused the radius of curvature of the surface to change from 1/0 mm (flat) to approximately 1/3600 mm (0-V to 600-V position). This demonstrated the large shape changes that can be initiated with these controls.

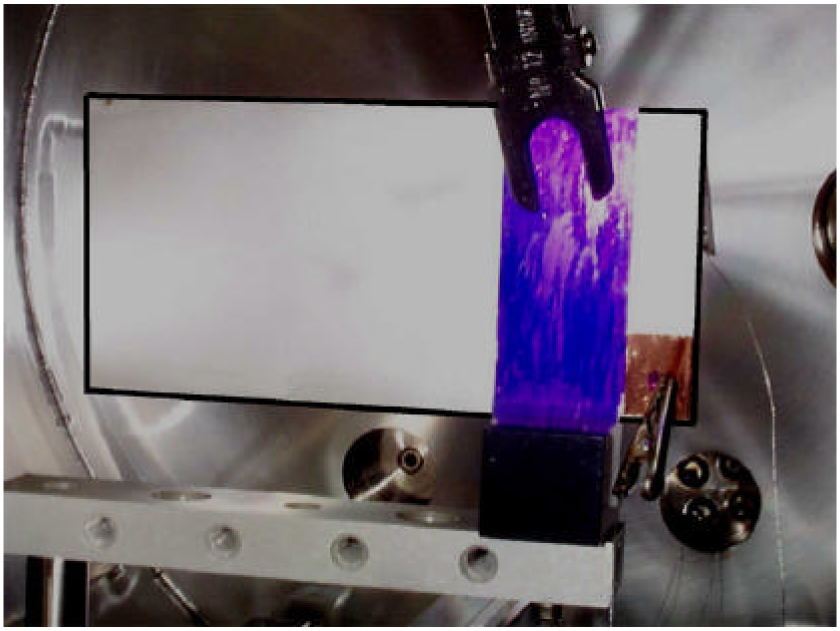

Figure 27. Photo of PVDF Type A bimorph mounted in vacuum chamber.

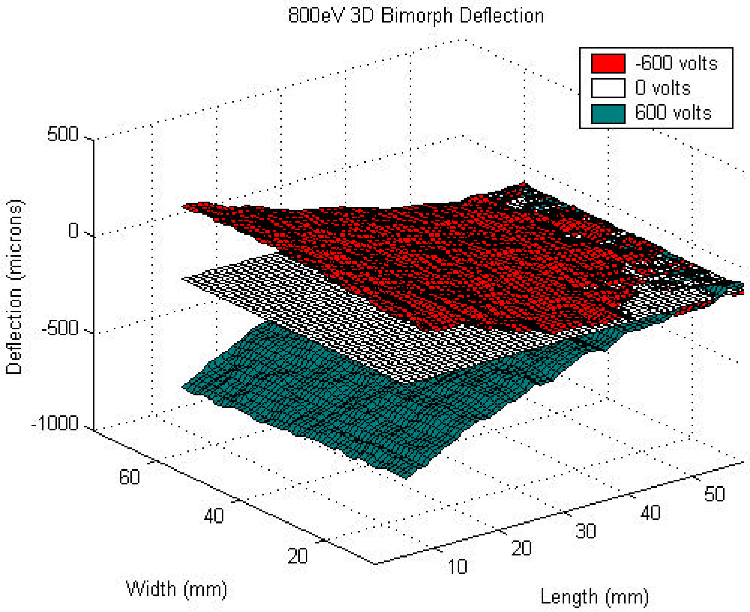

Figure 28. Three-dimensional profiles of 800-eV actuated Type A bimorph with ±600-V controls applied.

This experiment was then performed again for the next energy level being analyzed (1000 eV) to the final energy level (1400 eV). These profiles were plotted to compare energy level actuation. Figure 29 shows 0-V actuation profiles of 400-, 600-, 800-, and 1000-eV electron beams. Because this experiment was comparative in nature, these plots are all normalized to 400 eV with a 0-V surface profile. That is why the 400-eV-beam surface plot shows all zero displacement. Due to measurement resolution errors, other surface plots can be seen to show through the zero baseline at the far right of the figure. An electron beam of 600 eV induces little to no deflection. However an 800-eV beam produces more linear deflections due to positive and negative control voltages. It appears that 800 eV is the most efficient beam energy level. Analysis of the macroscopic control capabilities is further outlined in the discussion.

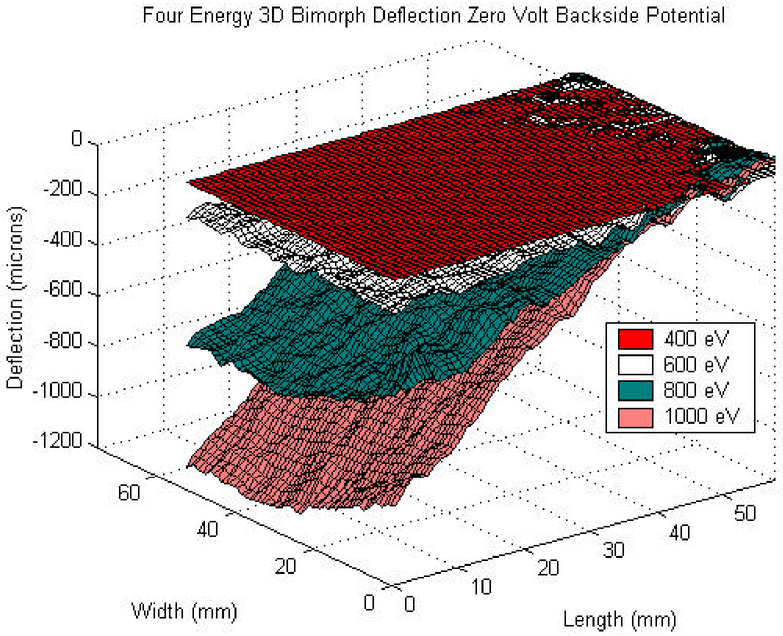

Figure 29. Three-dimensional profiles of 400-eV, 600-V, 800-eV, and 1000-eV beams with 0-V control applied.

Copolymer Nanocontrol Analysis

As previously stated, copolymer research was focused on coarsely characterizing the capabilities of this control technique to induce nanometer level surface changes. A group of ESPI measurements were taken of the 52-µm Type D copolymer. Because the in-plane piezoelectric coefficients are nearly identical in a copolymer, the initially flat, constrained material assumes a convex or concave shape in the presence of an electric field. An 800-eV electron beam was imposed on the 29-mm-diam specimen, which was located 30 cm from the electron gun tip. The electrode potential was varied from –10 to +10 V. The material displaced in a convex shape for positive voltages and a concave shape for negative voltages when referenced to the 0-V, 800-eV-beam surface profile. The maximum deflection in the center of the material was approximately 200 nm for the 1-V electrode potential, 600 nm for the 5-V electrode potential, and 1300 nm for the 10-V electrode potential. The resulting Type D copolymer shape is shown in Figure 30 for ±5-V and ±1-V control excitations. The clamp was located toward the left edge of these images. The irregular deflection here was due to a tighter constraint at this position.

Hysteresis/Electron Energy Analysis

This experiment was designed to establish the optimized electron energy level for actuation of a Type B bimorph. Hysteresis is an important characteristic to analyze in any piezoelectric material. Hysteresis in PVDF results from changes in electromechanical losses in the material. These losses are different for inducing an increase in strain than for inducing a decrease in strain. Bimorphs were actuated, as in the first experiment, with 400-, 600-, 800-, 1000-, 1200-, and 1400-eV electron beams from a distance of 30 cm. Here, however, the control voltages used were in a finer mesh (±600 V at 10-V increments). As previously, between each change in control voltage level the bimorph was allowed 5 minutes to reach steady state. At this point, the midplane (tip to cantilever) was profiled. Because repetition gives better hysteresis data, the 0- to 600- to –600- to 0-V control loop was repeated five times consecutively. The following figures are the color-coded plots of the five loops of this data. It can be seen in Figure 31a and Figure 32a that massive jumps occurred along the hysteresis loop plots of a point 65-mm from the bimorph cantilever.

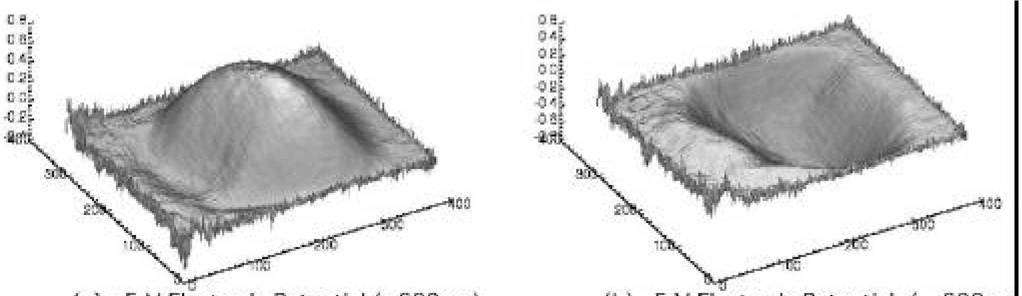

(a) +5 V Electrode Potential (~600nm) (b) -5 V Electrode Potential (~-600nm

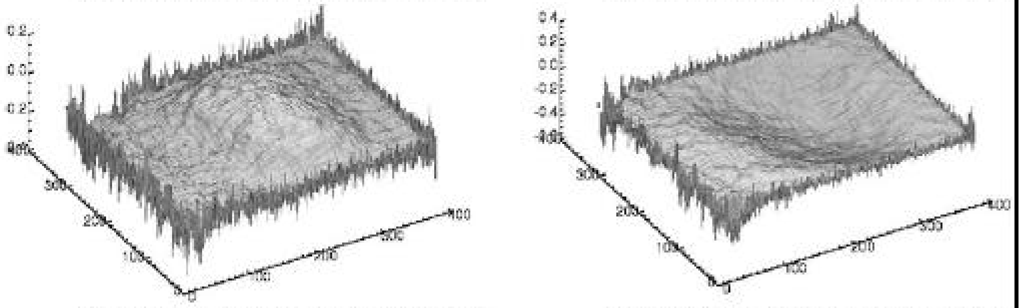

(c) +1 V Electrode Potential (~200nm) (d) -1 V Electrode Potential (~-200nm)

Figure 30. Type D copolymer ring clamp nanocontrol experimental images.

In Type B bimorph #1 poor manufacture caused small stiffness changes across the bimorphs width. This caused mechanical snap through. The hysteresis in the bimorph snap through occurs at two different points (one for changes in a positive direction the other for changes in a negative direction). In this case, for the 400-eV bimorph #1 data, snap through is seen to start at 0 µm and end at approximately –2000 µm with increasing control voltage. Then with decreasing control voltage snap through starts at 0 µ and jumps up to approximately 2000 µm.

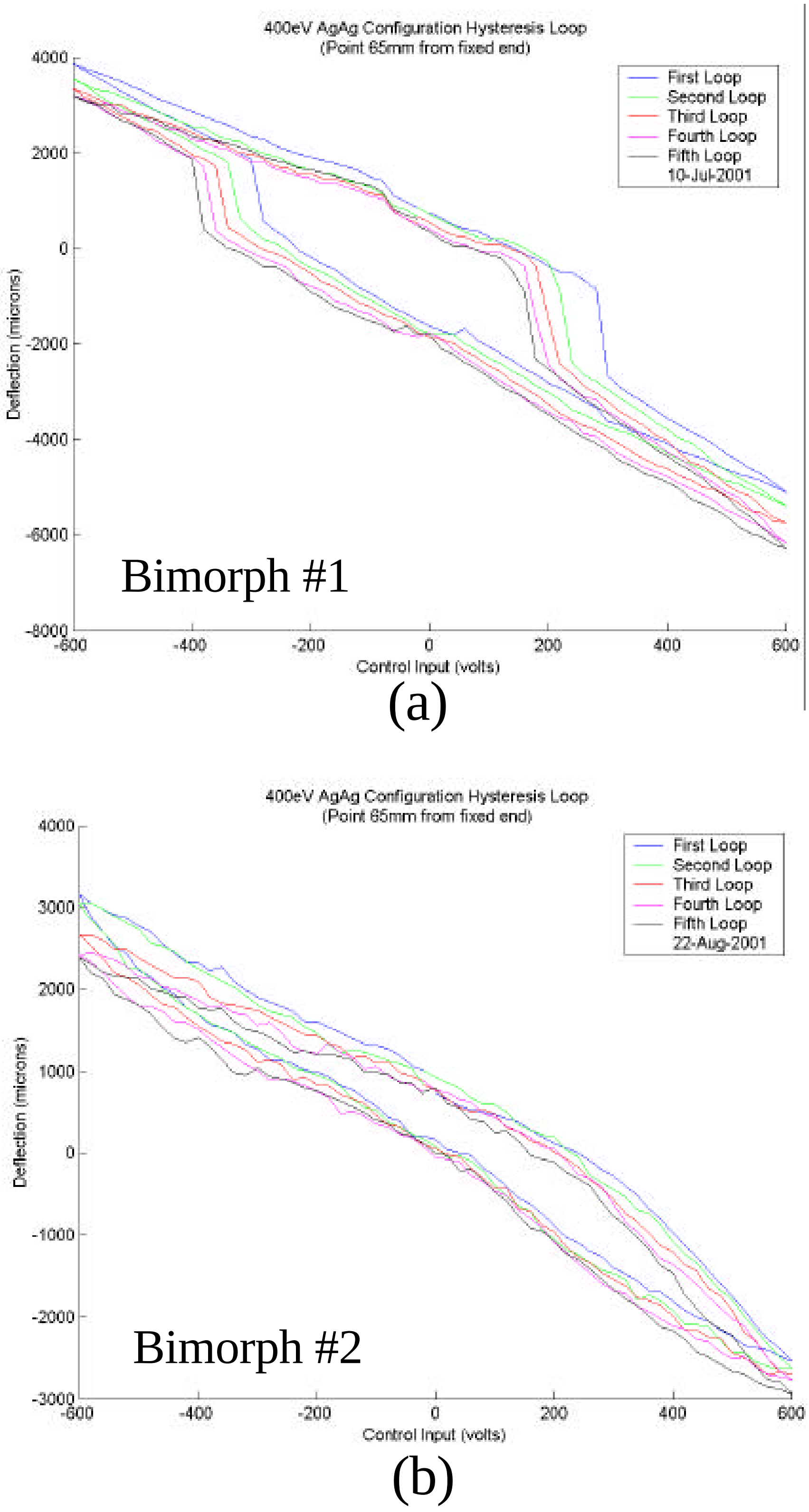

Figure 31. Tip deflection hysteresis plots of the actuation of Type B bimorphs by a 400-eV electron beam.

This 600-eV plot in Figure 32a shows this same behavior. This plot is 200 eV higher in electron energy and the “jumps” have shifted in voltage by 200 V, but the 0- to –2000-μ and 0- to 2000-μm jump behavior remains the same.

Figures 33, 34, and 35 represent the hysteresis of the same point 65-mm from the bimorph cantilever actuated with 800, 1000, and 1200 eV respectively. A decrease in hysteresis in the negative control voltage regime is evident as the energy levels increase, with 1200 eV being very linear. However, a breakdown of both actuation capability and linearity can be seen in Figure 36 at 1400 eV. These data support that 1200 eV is the optimum energy level toward producing linear displacements and minimizing hysteresis irregularities.

Displacement Caused by the Electron Beam Current

This experiment was designed to show the relationship between the electron beam current and the actuation of the bimorph. While the control voltages were maintained at 0 V, constant electron beams of increasing energy level current excited the Type B bimorphs. The bimorph tip deflection was recorded as a function of time after each current change. Because of the pyroelectric properties of PVDF, the electron gun output current was controlled through the use of the cathode grid voltage settings. This maintained a constant current through the cathode, which kept it at an approximately constant temperature while permitting the emitted electron stream current to be varied.

In Figure 37, the tip deflection and electron gun output current are plotted versus the cathode grid voltage for 400 eV. The deflections here are directly proportional to the electron current. Figure 38 is a similar plot for 600 eV. At this point, three distinct regions are starting to become evident (the optimum is shown in Figure 39). Region III has no input current. The electron gun cathode cools due to the effect of electrons removing energy as they are emitted. Region III represents this temperature drift between experiments (higher current at the end of one experiment, zero at the start of the next). When the current was stopped, the cathode temperature drifted to a new steady state. This temperature drift caused deflection in the bimorph as a result of the PVDF’s pyroelectric properties. If given enough time between experiments, Region III would have started at a steady-state temperature and would have been flat in all these experiments.

Regions II and I are the important regions. At the start of Region II, there is a slight change in slope as the cathode temperature drops because of electrons being emitted and the pyroelectric effects are seen once again. When the temperature reaches steady state, the slope becomes completely linear. In Region II, the Type B bimorph surface, which has no charge yet, is filling up to capacity. One electron is attracted to each dipole in the material. After this balance is reached and all dipoles are filled, the field, as a result of the cloud of incoming electrons starts to become a major factor in the overall net field (Region I). At this point, a change in the slope of these curves is evident and represents a DC offset to the system. Figures 39, 40, 41, and 42 are these same plots for 800, 1000, 1200, and 1400 eV, respectively. These three regions become better defined with increasing energy. Displacement DC offset increases with increasing current in Region I. Lower currents (Region II) provide pure actuation response without the added DC offsets to the system.

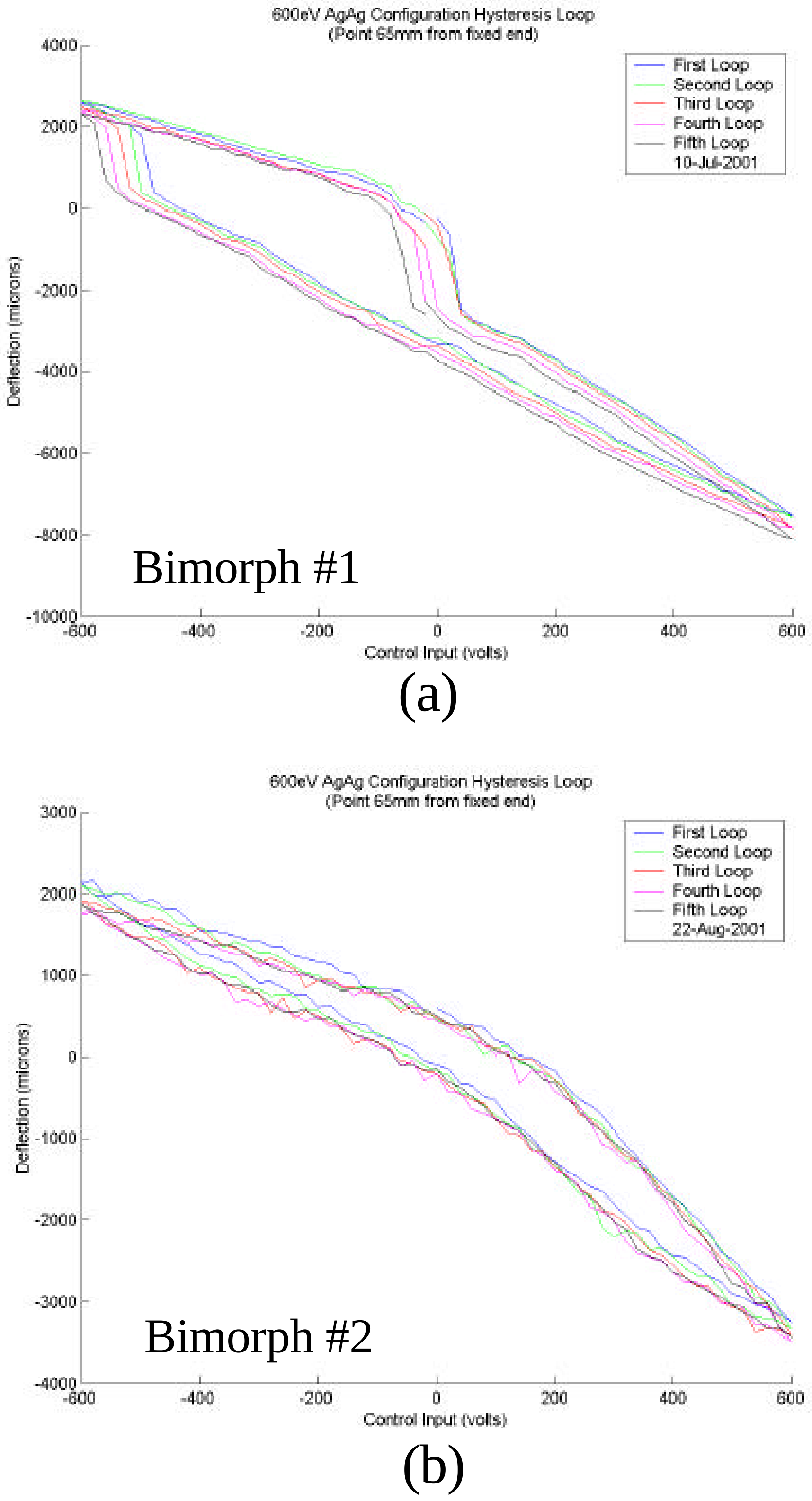

Figure 32. Tip deflection hysteresis plots of the actuation of Type B bimorphs by a 600-eV electron beam.

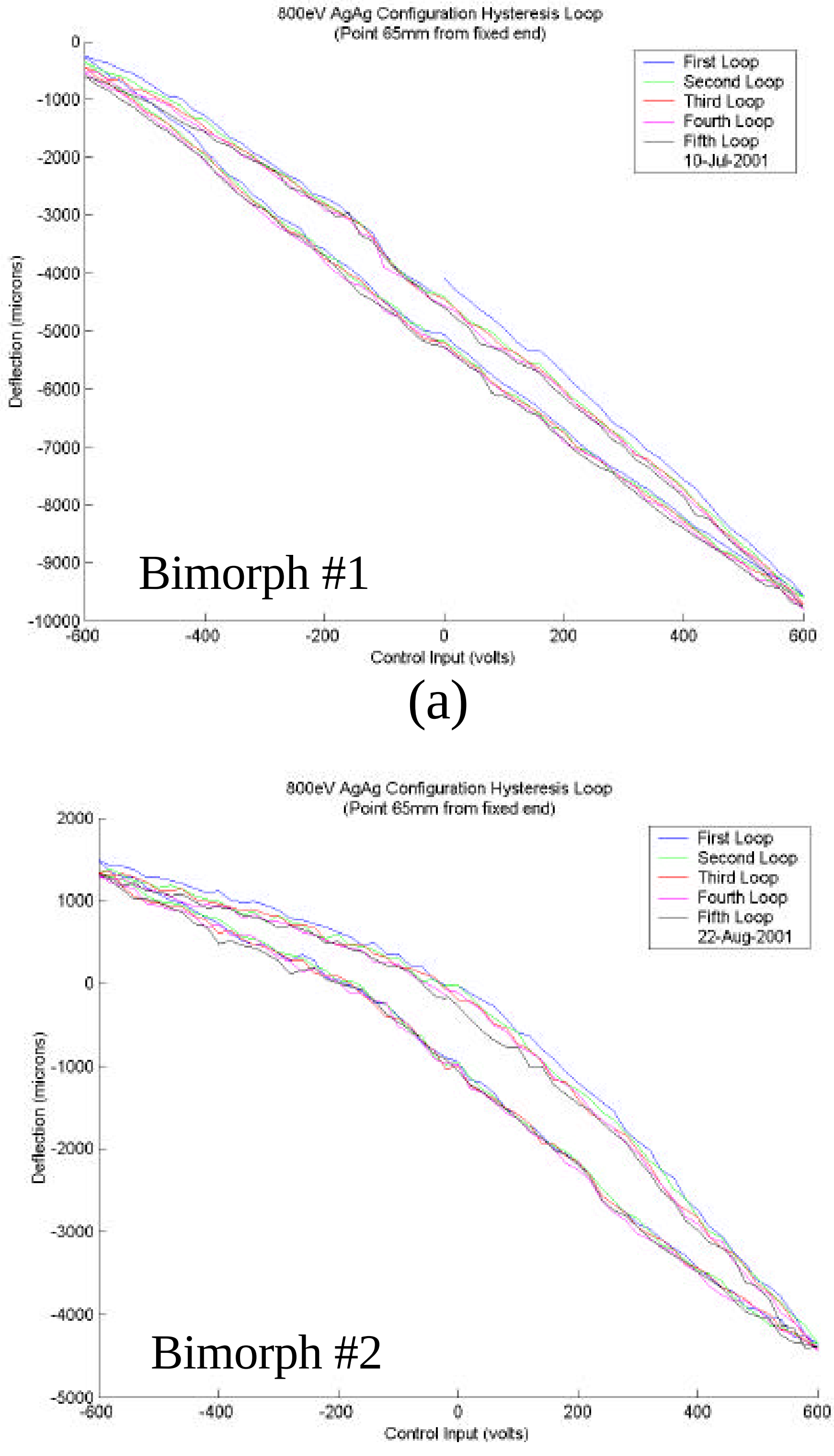

(a)

(b)

Figure 33. Tip deflection hysteresis plots of the actuation of Type B bimorphs by a 800-eV electron beam.

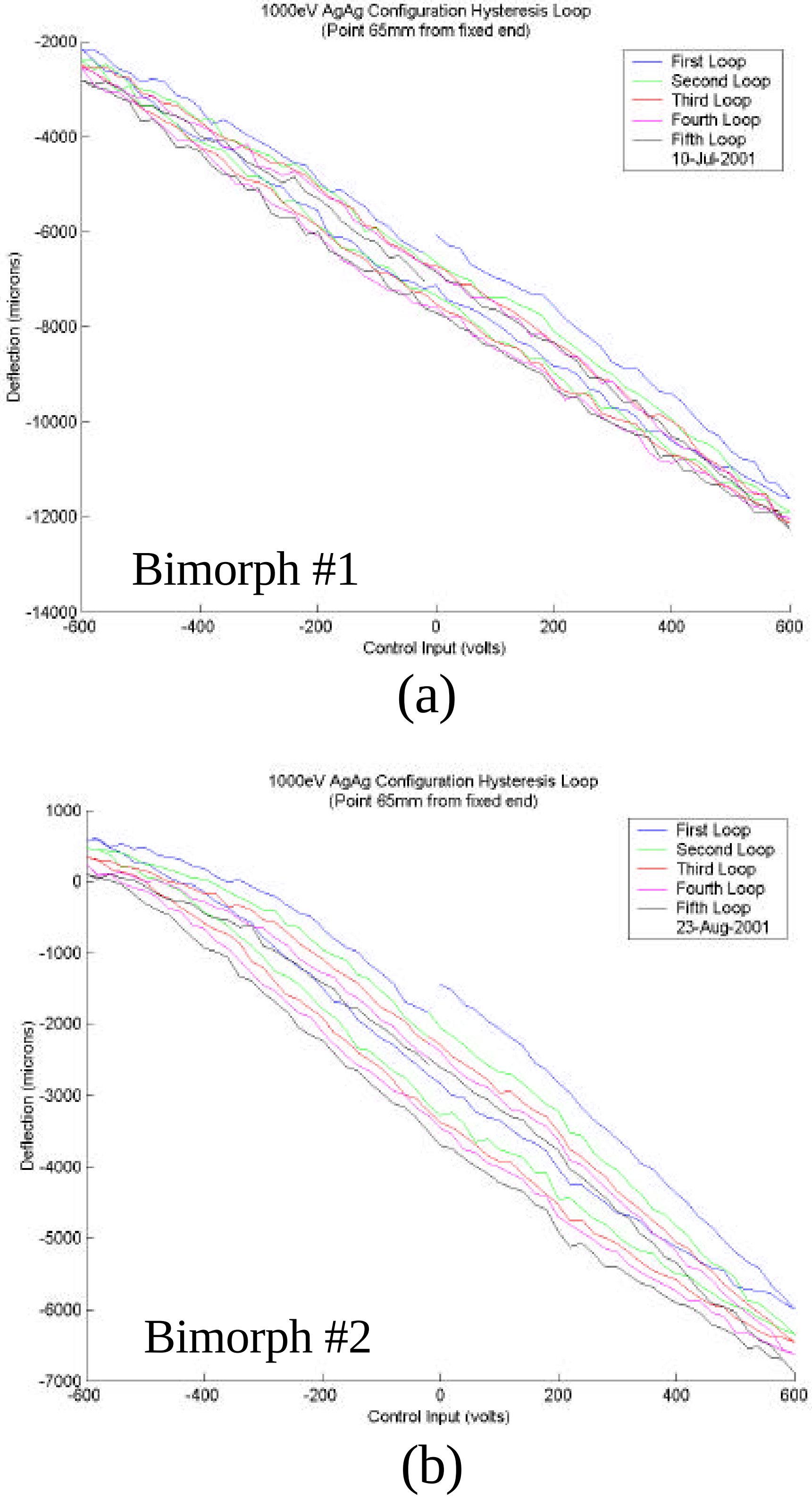

Figure 34. Tip deflection hysteresis plots of the actuation of Type B bimorphs by a 1000-eV electron beam.

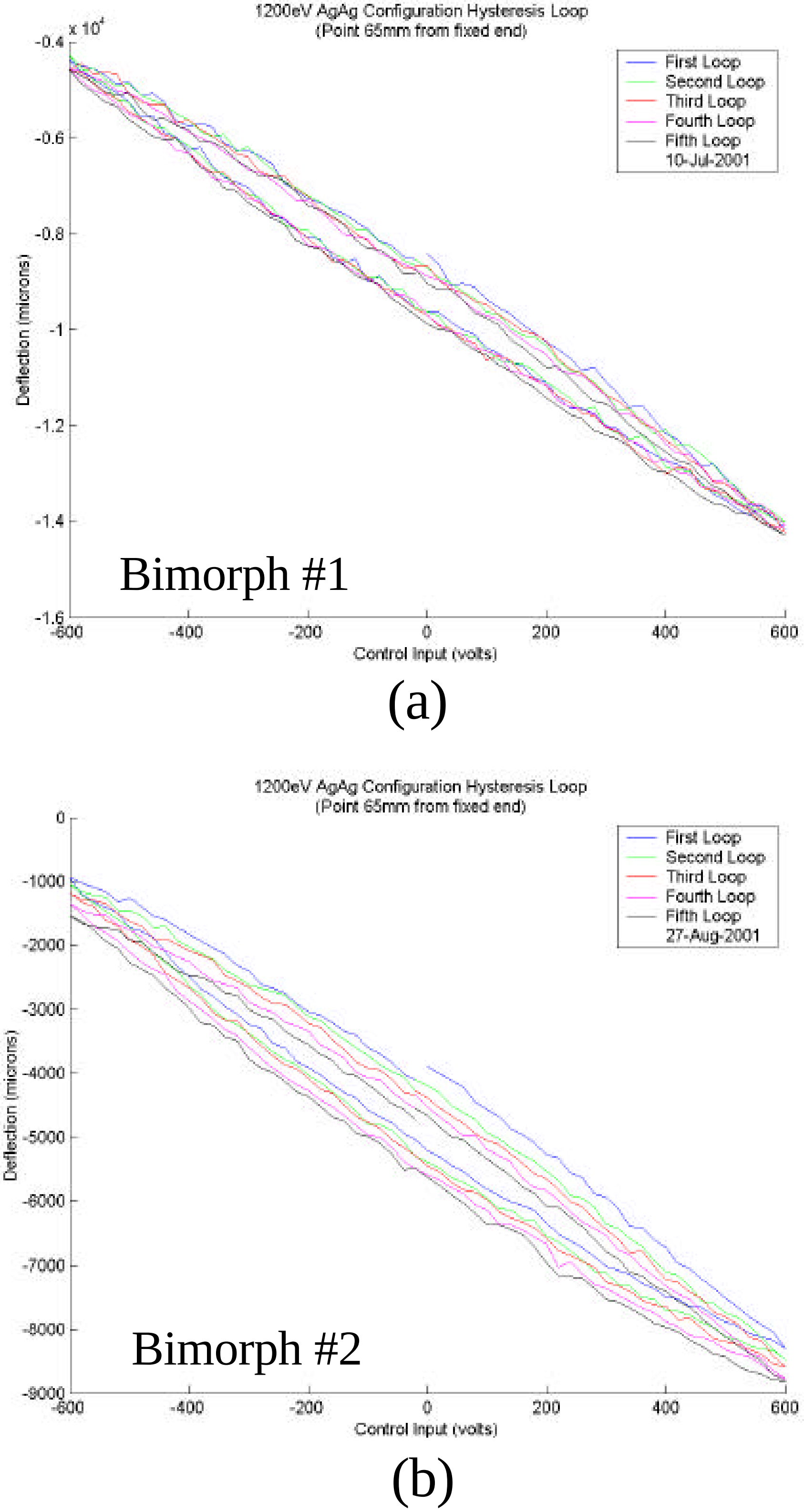

Figure 35. Tip deflection hysteresis plots of the actuation of Type B bimorphs by a 1200-eV electron beam.

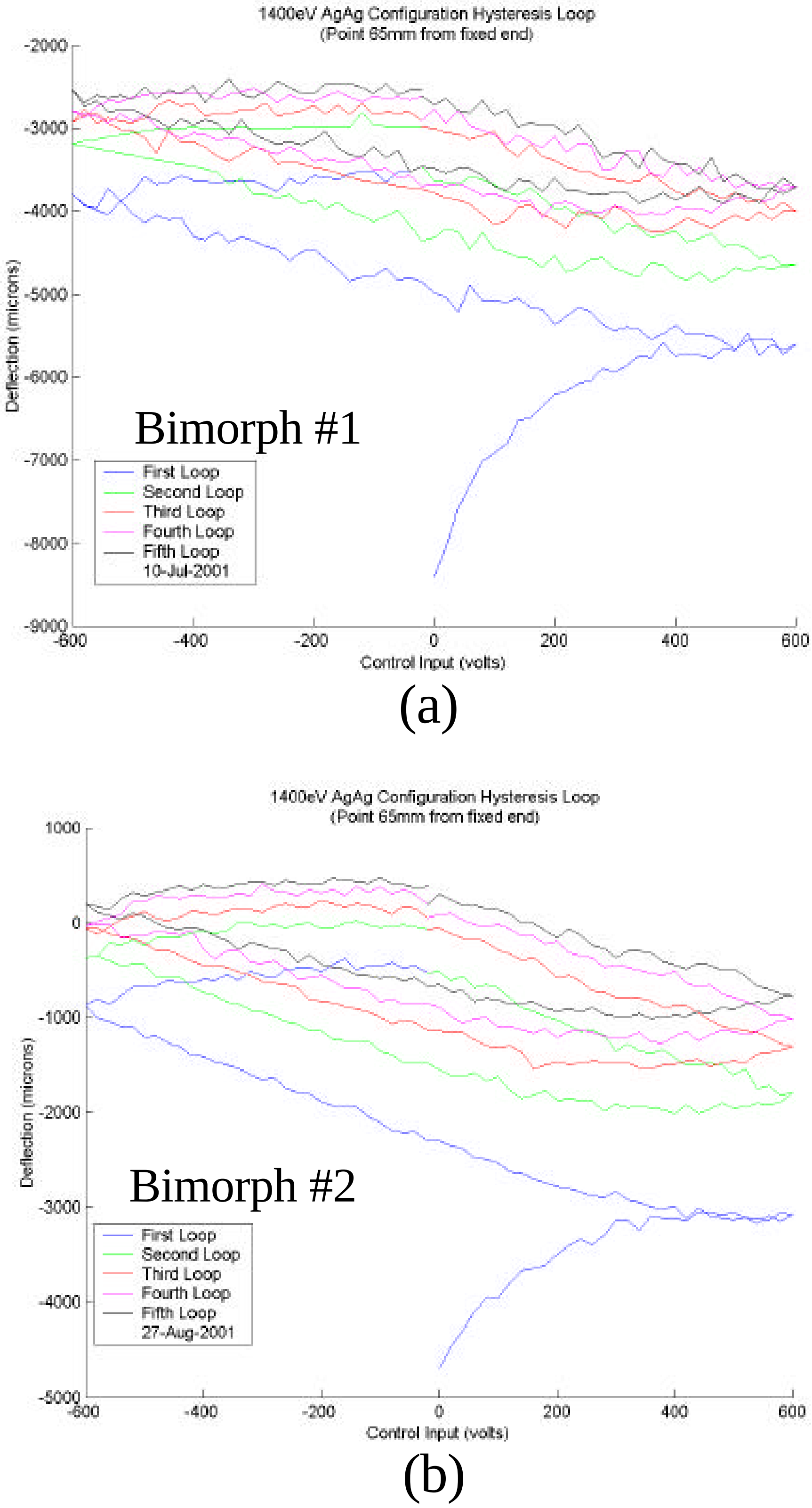

(a)

(b)

Figure 36. Tip deflection hysteresis plots of the actuation of Type B bimorphs by a 1400-eV electron beam.

Displacement Caused by the Electron Beam Current

This experiment was designed to show the relationship between the electron beam current and the actuation of the bimorph. While the control voltages were maintained at 0 V, constant electron beams of increasing energy level current excited the Type B bimorphs. The bimorph tip deflection was recorded as a function of time after each current change.

Because of the pyroelectric properties of PVDF, the electron gun output current was controlled through the use of the cathode grid voltage settings. This maintained a constant current through the cathode, which kept it at an approximately constant temperature while permitting the emitted electron stream current to be varied.

In Figure 37, the tip deflection and electron gun output current are plotted versus the cathode grid voltage for 400 eV. The deflections here are directly proportional to the electron current. Figure 38 is a similar plot for 600 eV. At this point, three distinct regions are starting to become evident (the optimum is shown in Figure 39). Region III has no input current. The electron gun cathode cools due to the effect of electrons removing energy as they are emitted. Region III represents this temperature drift between experiments (higher current at the end of one experiment, zero at the start of the next). When the current was stopped, the cathode temperature drifted to a new steady state. This temperature drift caused deflection in the bimorph as a result of the PVDF's pyroelectric properties. If given enough time between experiments, Region III would have started at a steady-state temperature and would have been flat in all these experiments.

Regions II and I are the important regions. At the start of Region II, there is a slight change in slope as the cathode temperature drops because of electrons being emitted and the pyroelectric effects are seen once again. When the temperature reaches steady state, the slope becomes completely linear. In Region II, the Type B bimorph surface, which has no charge yet, is filling up to capacity. One electron is attracted to each dipole in the material. After this balance is reached and all dipoles are filled, the field, as a result of the cloud of incoming electrons starts to become a major factor in the overall net field (Region I). At this point, a change in the slope of these curves is evident and represents a DC offset to the system. Figures 39, 40, 41, and 42 are these same plots for 800, 1000, 1200, and 1400 eV, respectively. These three regions become better defined with increasing energy. Displacement DC offset increases with increasing current in Region I. Lower currents (Region II) provide pure actuation response without the added DC offsets to the system.

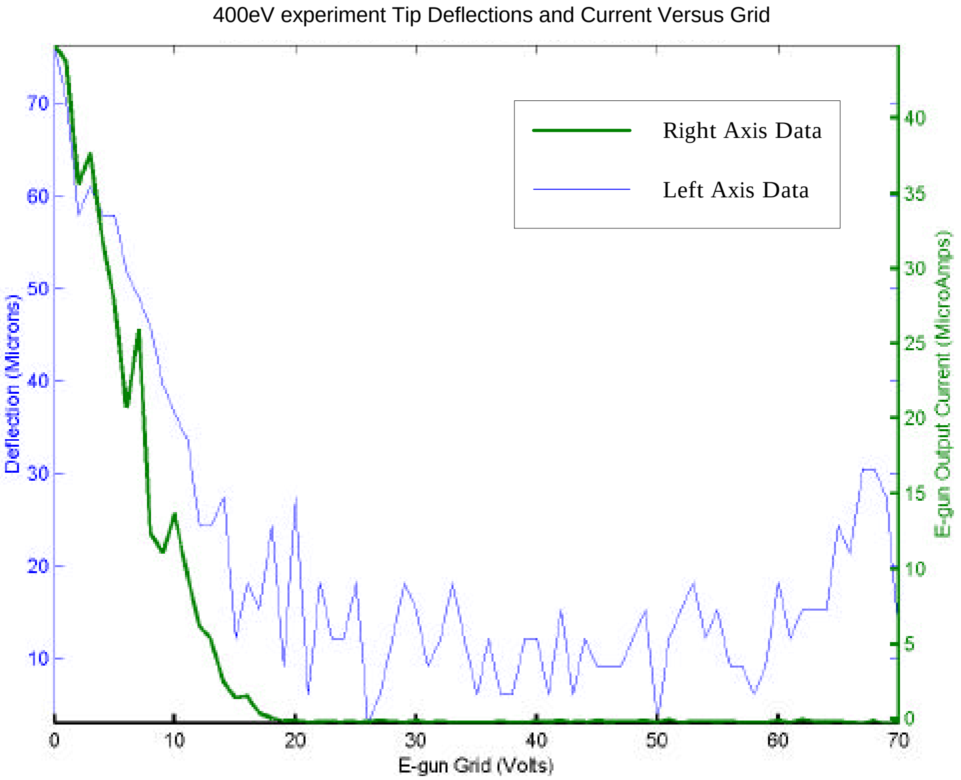

Figure 37. Tip deflection plot of the actuation of a Type B bimorph by a 400-eV current.

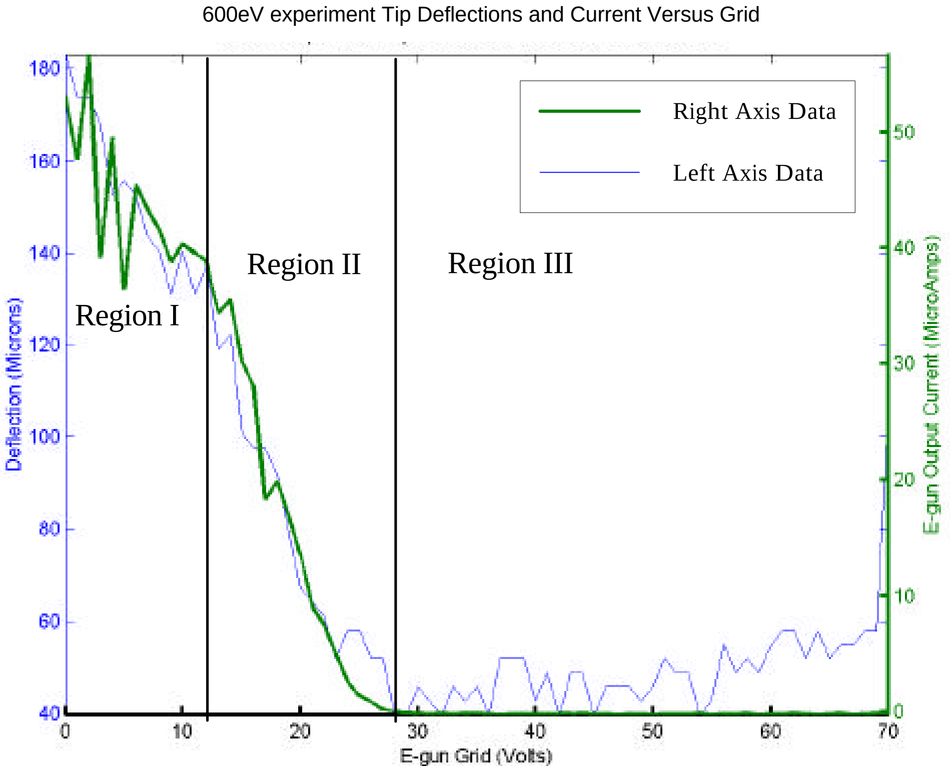

Figure 38. Tip deflection plot of the actuation of a Type B bimorph by a 600-eV current.

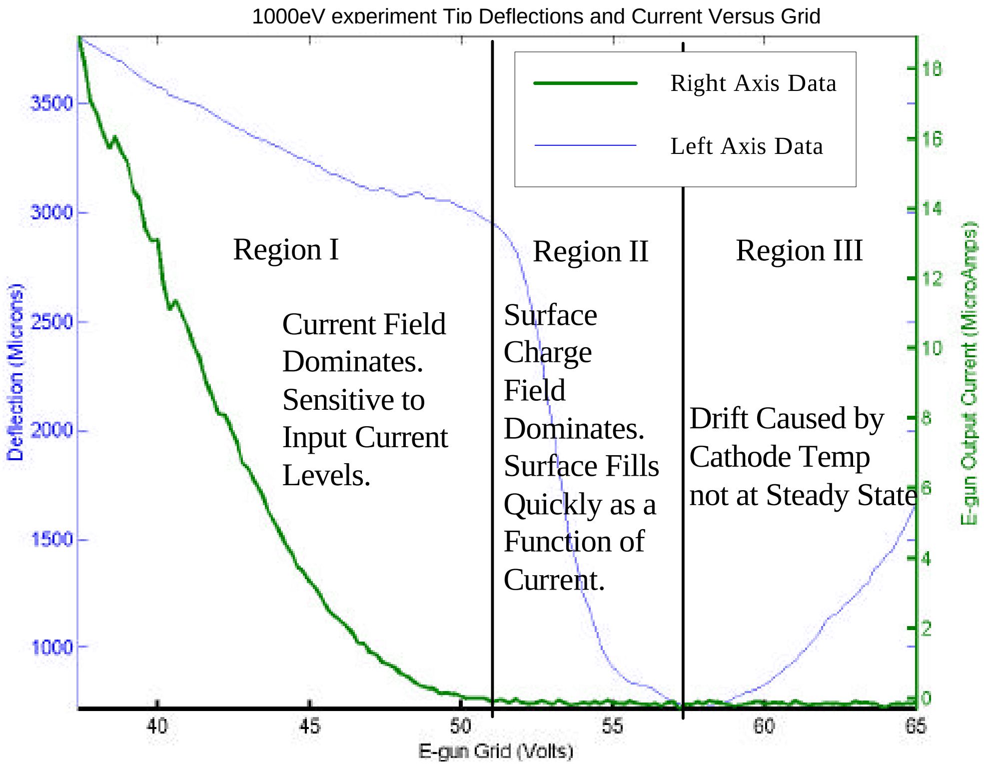

Figure 39. Tip deflection plot of the actuation of a Type B bimorph by a 1000-eV current.

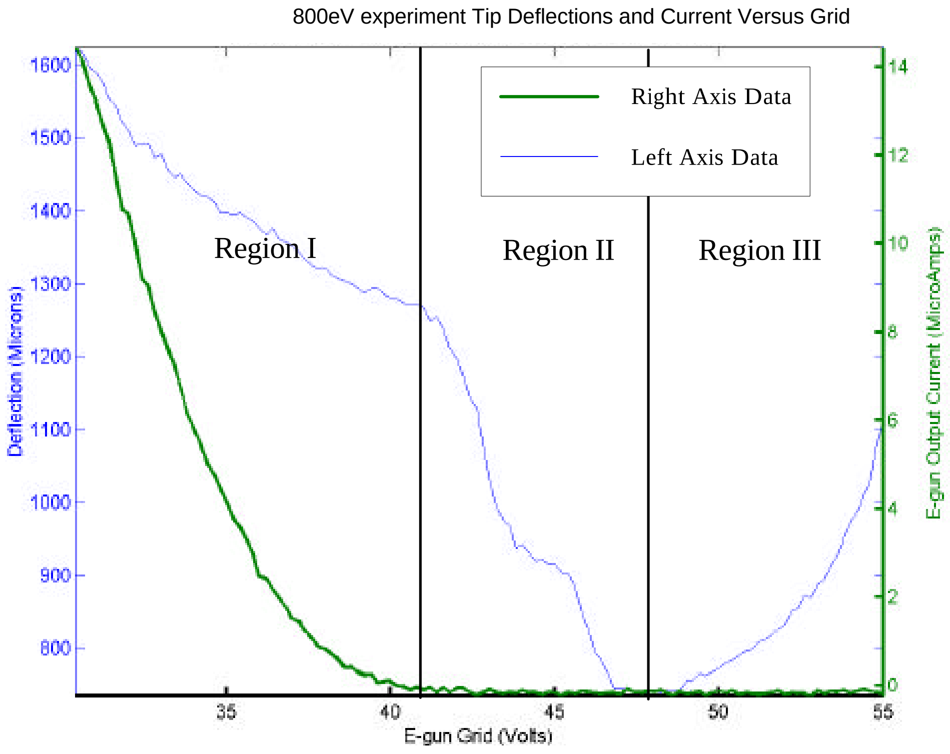

Figure 40. Tip deflection plot of the actuation of a Type B bimorph by an 800-eV current.

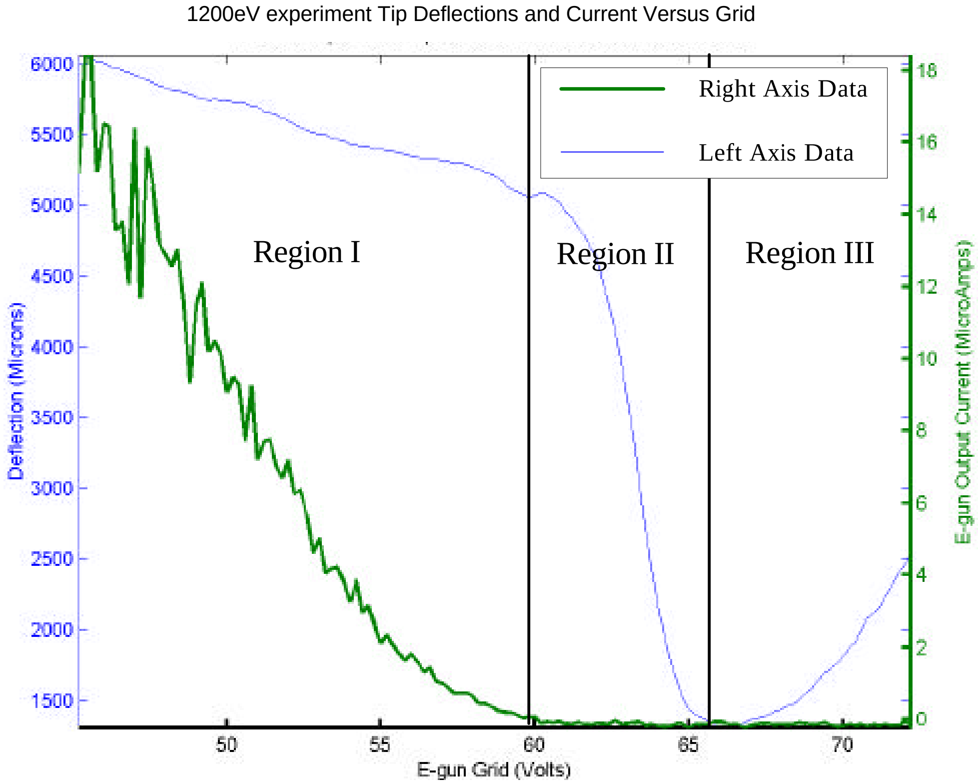

Figure 41. Tip deflection plot of the actuation of a Type B bimorph by a 1200-eV current.

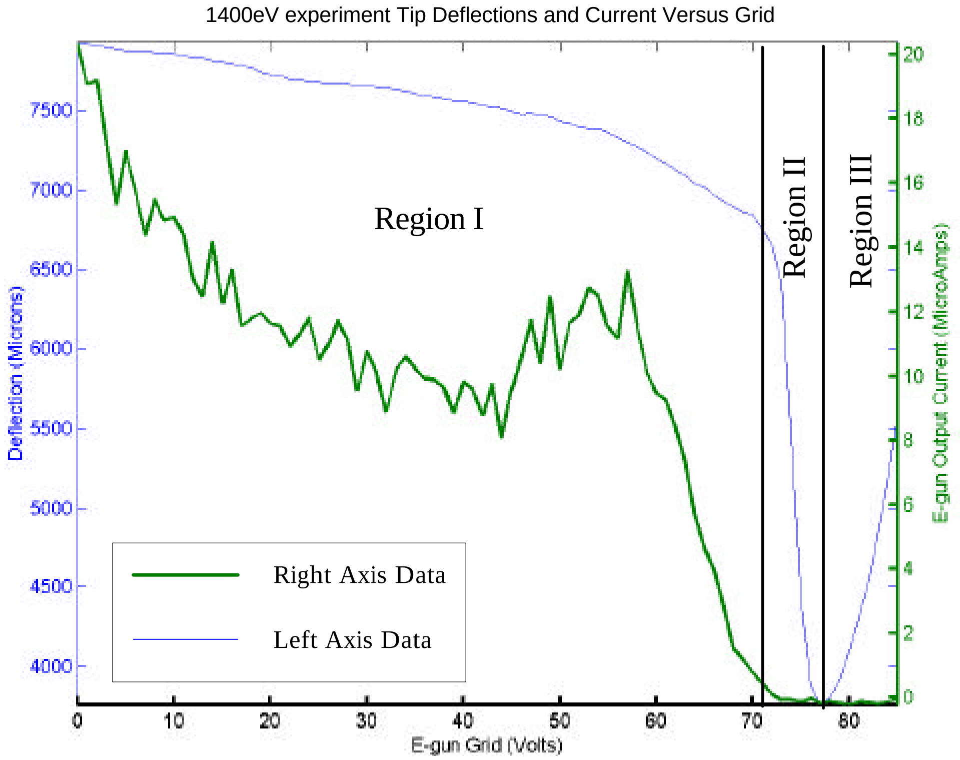

Figure 42. Tip deflection plot of the actuation of a Type B bimorph by a 1400-eV current.

Charge Bleed/Displacement Drift

Characterization of the charge dissipation was done by actuating a Type B bimorph at several energy levels with a constant control voltage from 30 cm away. Steady state was reached with the gun. The cathode grid was then changed to 150 V to stop the flow of electrons. Figures 43, 44, 45, 46, 47, and 48 show the Type B bimorph tip deflections plotted over time for 400-, 600-, 800-, 1000-, 1200-, and 1400-eV electron energy experiments, respectively. In each plot a 500-V control was used. The vertical red astrix line represents when the electron flow was stopped, and the vertical green diamond line represents when the control voltage was changed to 0 V. Each graph has a time dilated window that shows the instantaneous dissipation behavior that occurred when the electron flow was removed. In the time dilated windows of these graphs, the tip deflection dissipation was less than 10 µm (the resolution of the sensor) in a minimum of 5 seconds.

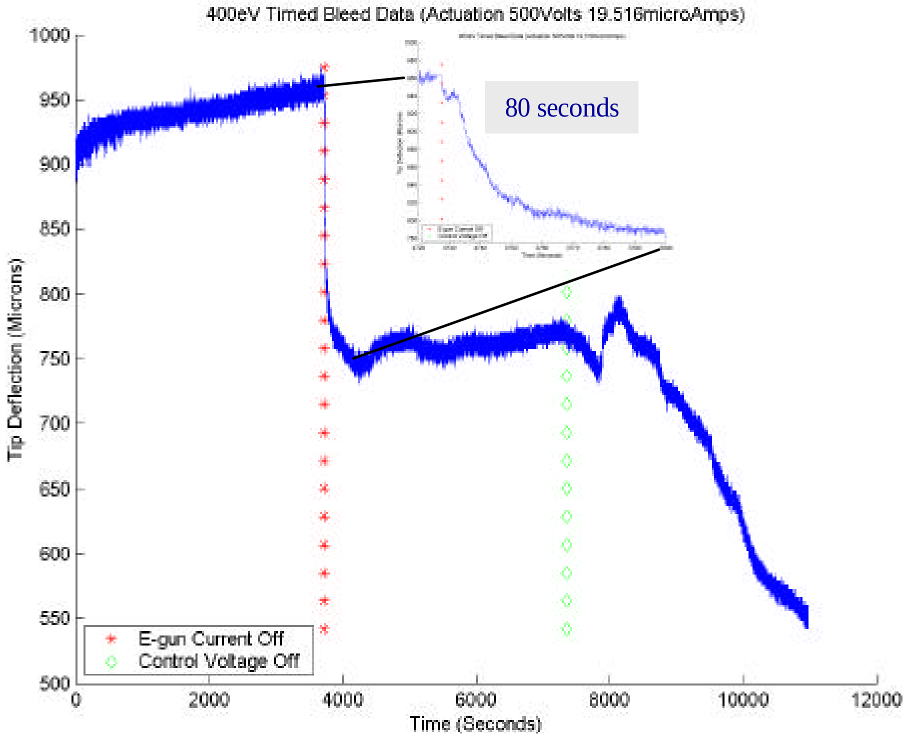

Figure 43. Plot of the actuation decay of a Type B bimorph by a 400-eV current after 19.5 mA and 500 control V.

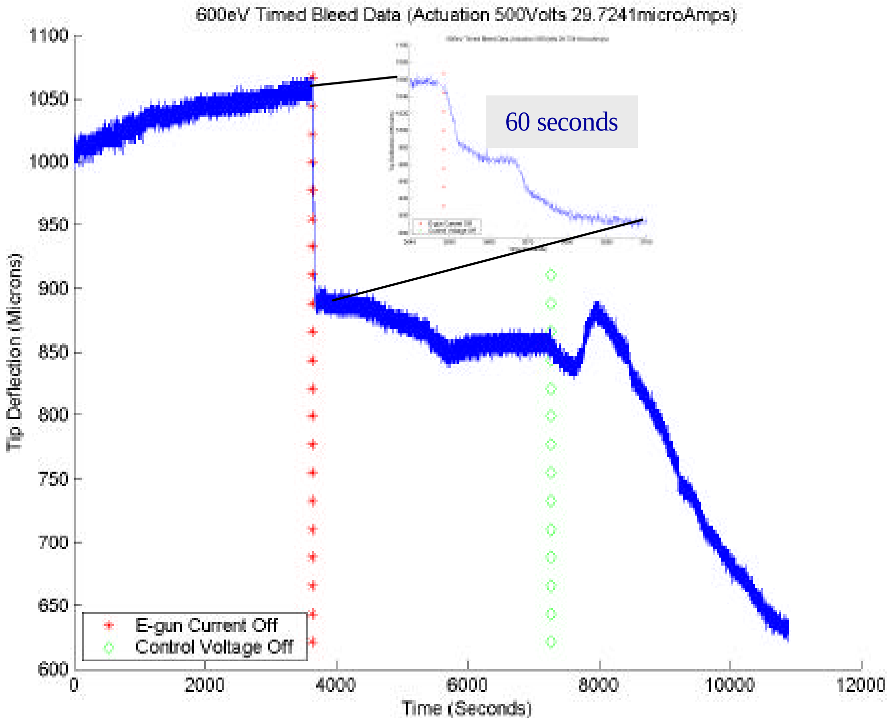

Figure 44. Plot of the actuation decay of a Type B bimorph by a 600-eV current after 29.7 mA and 500 control V.

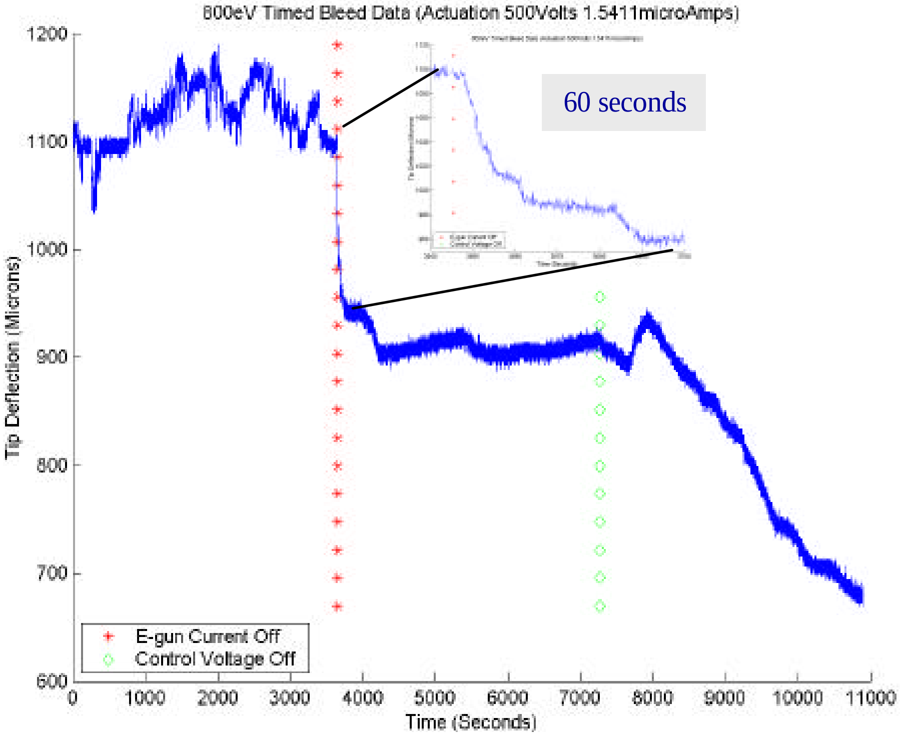

Figure 45. Plot of the actuation decay of a Type B bimorph by an 800-eV current after 1.5 mA and 500 control V.

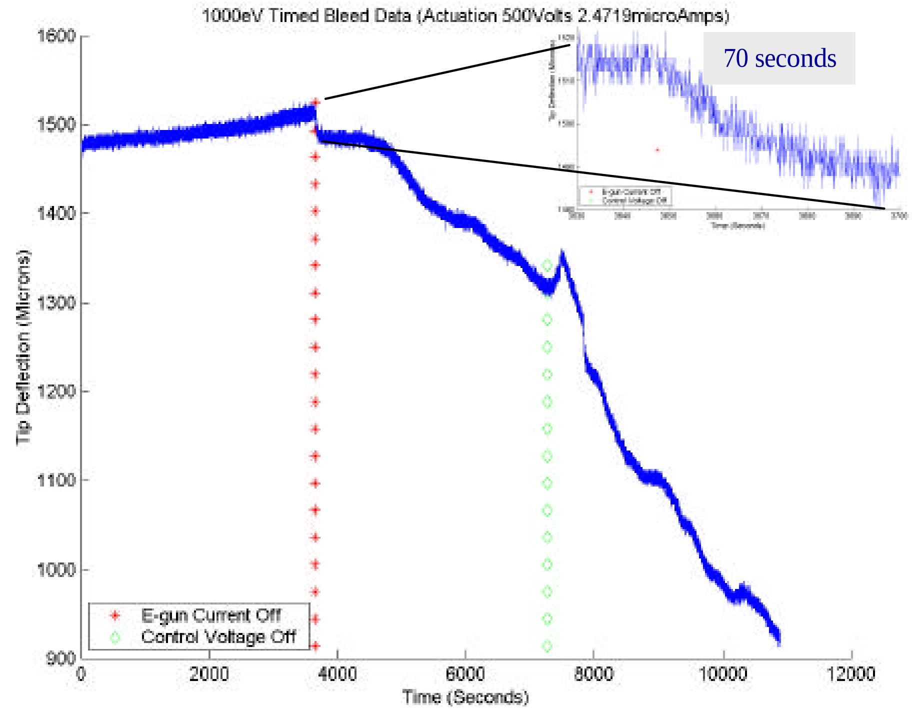

Figure 46. Plot of the actuation decay of a Type B bimorph by a 1000-eV current after 2.5 μA and 500 control V.

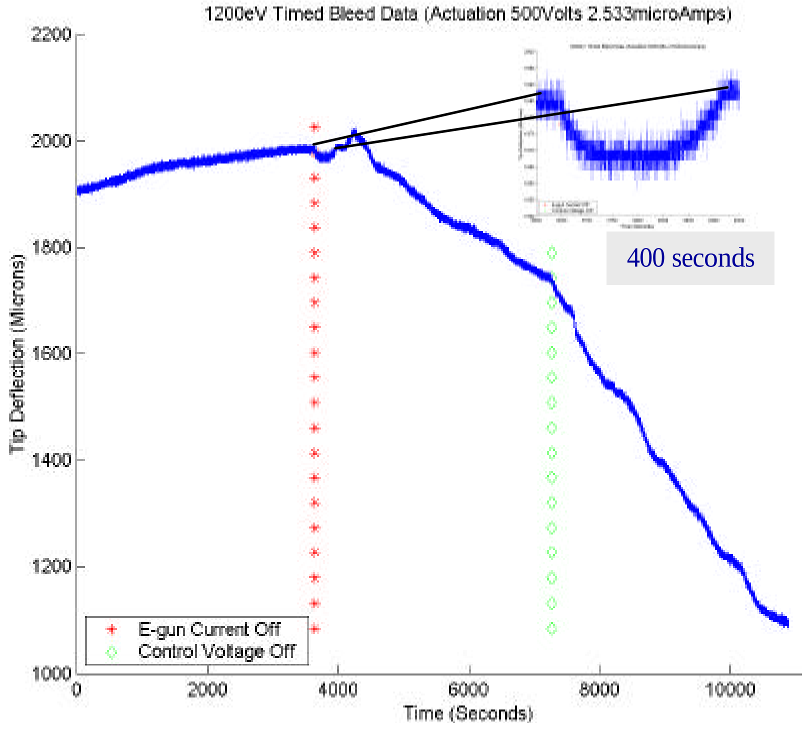

Figure 47. Plot of the actuation decay of a Type B bimorph by a 1200-eV current after 2.5 μA and 500 control V.

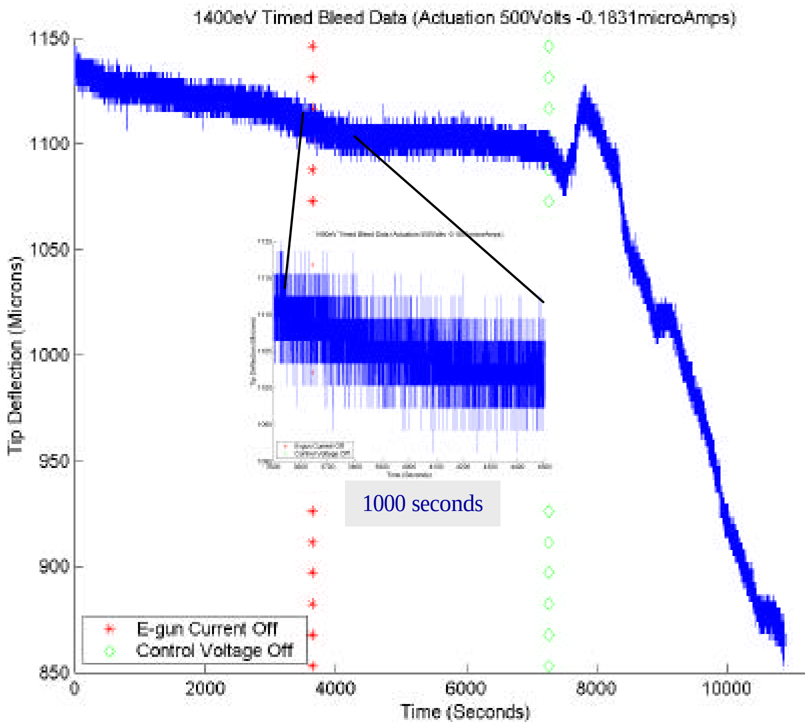

Figure 48. Plot of the actuation decay of a Type B bimorph by a 1400-eV current after 0.2 mA and 500 control V.

Control

The ability to make on-command adjustment is needed for a functioning closed-loop thin-film mirror system. The ability to control a bimorph and the characteristics of this control behavior were examined.

Figure 49 shows the PID controller design used for closed-loop experiments. The PID controller in Figure 50 was set up to allow the maintenance/adjustment of specified tip deflections by adjusting the control voltage on a Type A, B, or C bimorph. From 30 cm away, 800-eV electrons were used to actuate bimorphs in a flood pattern across the entire surface. The Proportional Integrator Derivative (PID) control settings were adjusted in an iterative fashion to achieve stable closed-loop tip control for each individual bimorph.

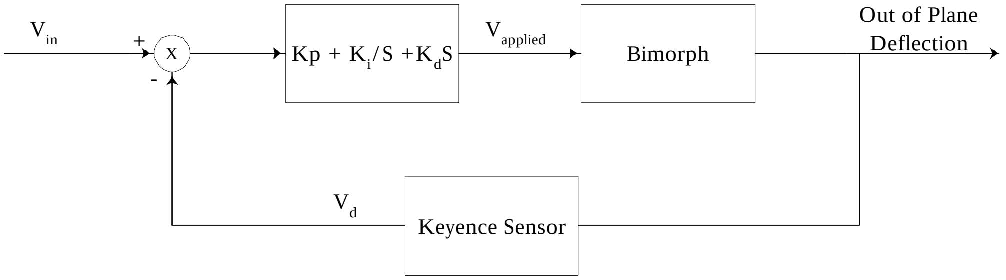

Figure 49. Diagram of PID control design used for bimorph regulation.

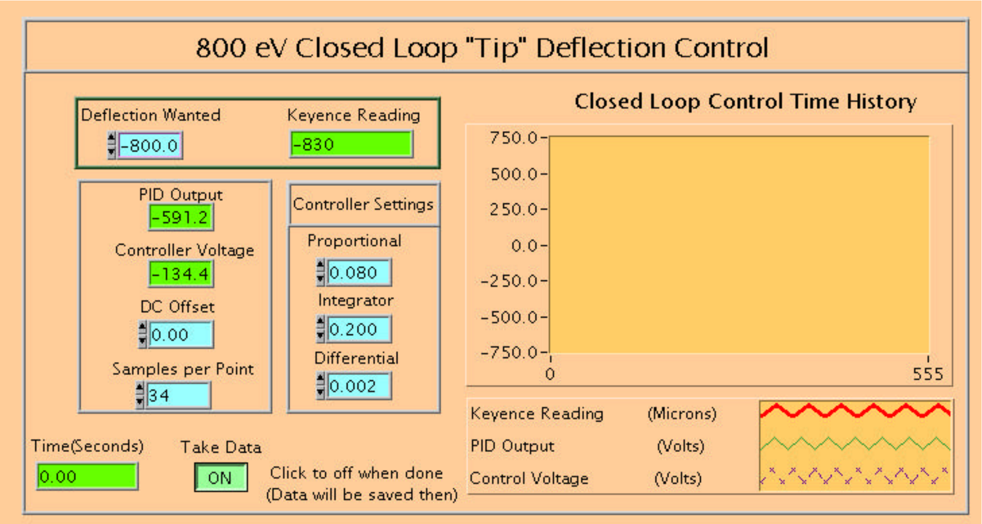

Deflection Wanted: -800.0
Keyence Reading: -830
PID Output: -591.2
Controller Voltage: -134.4
DC Offset: 0.00
Samples per Point: 34
Proportional: 0.080
Integrator: 0.200
Differential: 0.002
Time(Seconds): 0.00
Take Data: ON

Keyence Reading	(Microns)
PID Output	(Volts)
Control Voltage	(Volts)

Figure 50. Graphical User Interface (GUI) front panel of Type A, B, or C bimorph closed-loop tip control LabView VI.

Regulation and Secondary Electrons

Figure 51 shows the time histories of two different controller designs for a Type A and a type B bimorph. The Type A bimorph proved to have a much slower response (a time constant of 0.35/seconds) and needed a control with a less aggressive design. The Type B bimorph proved to have a faster steady state response (a time constant of 1.33/seconds) and responded well to aggressive control designs. These control responses show that the secondary electron emissions from bare PVDF are far less stable/controllable than the emissions from silver ink.

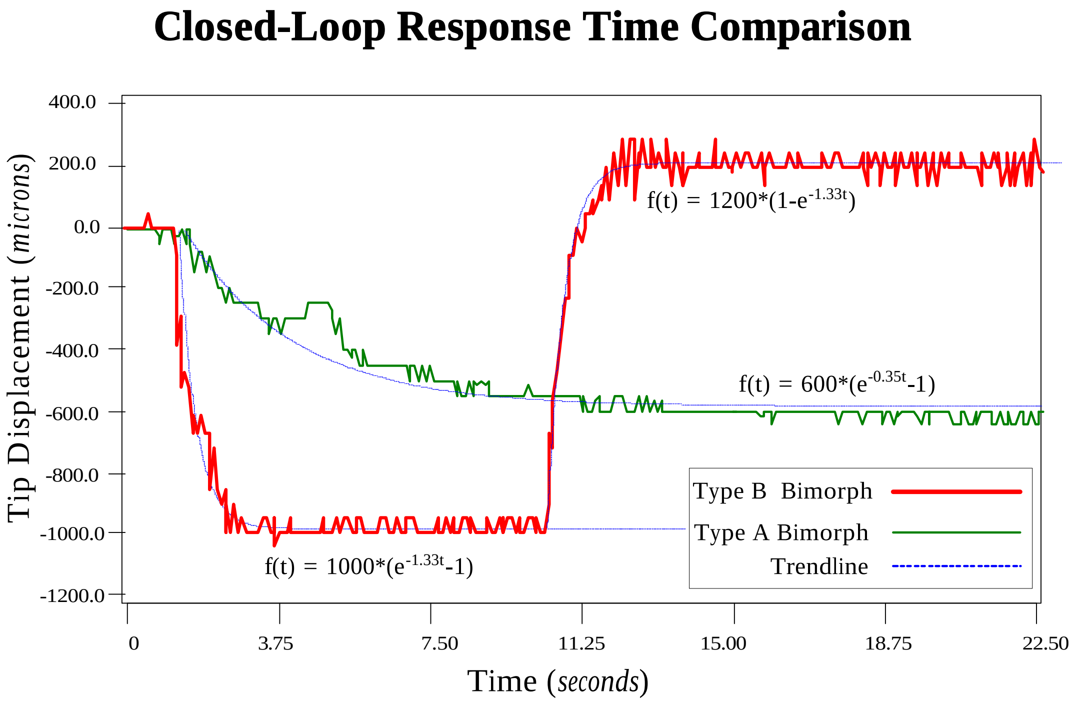

Figure 51. Closed-loop regulator response time histories of Type A and Type B bimorphs.

Controllability

The ability to perform closed-loop control on a bimorph was shown. The control performance characteristics were further analyzed through a series of amplitude- and frequency-dependent experiments to create general describing functions for an electron gun controlled PVDF bimorph system.

Mechanical Frequency Analysis

The structural dynamics of two Type C bimorphs were examined. Figures 52 and 53 show the structural response of the two bimorphs. The data were taken using the dSPACE control system to read the Keyence measured tip (28 mm from cantilever) displacement of the bimorphs. The bimorphs were "flicked" with the dSPACE set to trigger on a zero-crossover. This experiment was performed 10 times for both Type C bimorphs. Bimorph #1 had a first fundamental frequency of approximately 28.4 Hz. Bimorph #2 had a first fundamental frequency of 30 Hz. All control input frequency analyses of these Type C bimorphs were kept well below these frequencies to remove the structural effects in this controllability analysis.

Bimorph #1

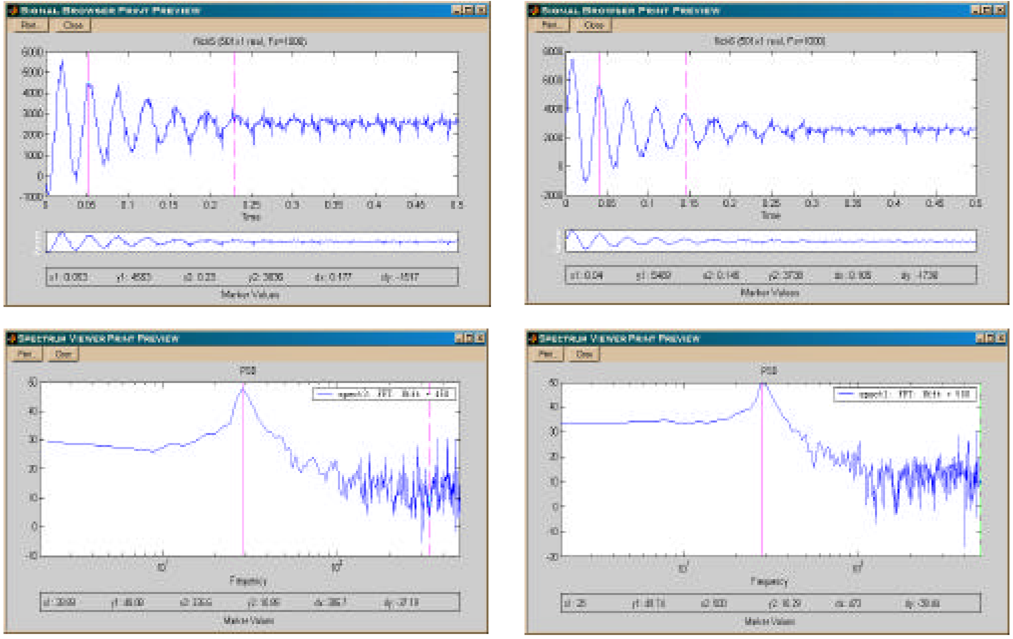

Figure 52. Frequency analysis of Type C bimorph #1.

Bimorph #2

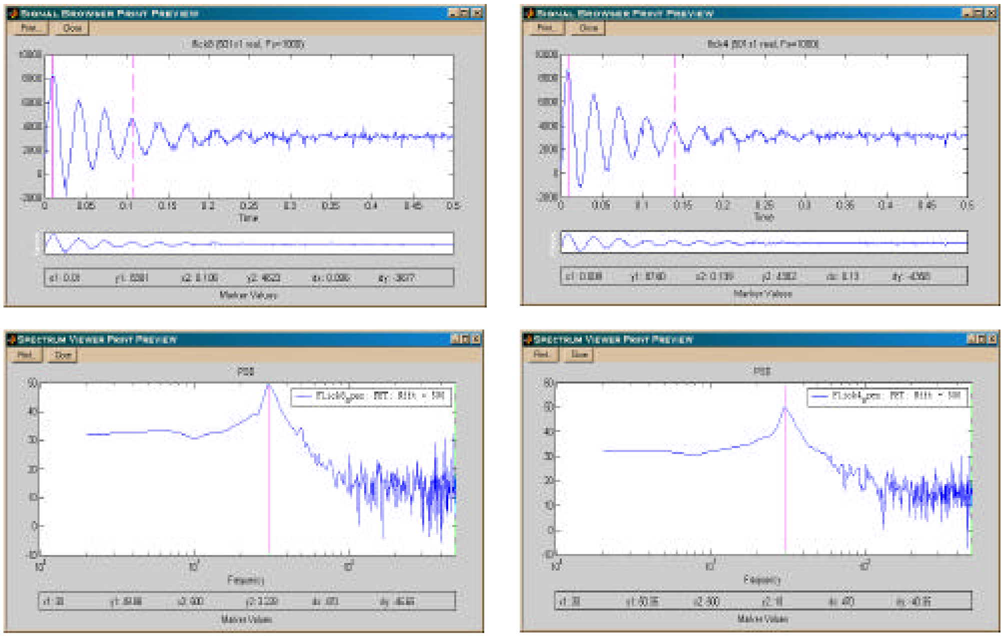

Figure 53. Frequency analysis of Type C bimorph #2.

Controllability Experiments

The general controllability of a PVDF bimorph actuated by a uniform electric field was examined. The controllability study was done using two Type C bimorphs. This is because (as previously shown) a Type C bimorph “forces” the electric field to be uniform regardless of the location of electron application.

In this research, the Type C bimorphs were mounted in a cantilever fashion 30 cm from the electron gun tip. They were then actuated using 800-eV electrons. The tip deflection was sampled at 1000 Hz in response to a sinusoidal control voltage of varying frequency and amplitude. Frequencies of 0.01, 0.05, 0.10, 0.50, 1.00, and 5.00 Hz and amplitudes of 10, 50, 100, 150, 200, 250, 300, 350, 400, 450, and 500 V were used. This frequency range kept the experiments well below the first mechanical fundamental frequency of both bimorphs. This experiment was repeated for three different electron current settings (0.10, 5.0, and 14.5 μA).

Figure 54 and Figure 55 show plots of the raw dynamic hysteresis and the raw time history for one experiment from this 3-D (current, frequency, amplitude) control matrix. These experiments were reduced to three parts: DC offset, response amplitude, and phase lag at each amplitude, frequency, and current. The DC offset and response amplitude data were then normalized to their maximum values (DC = 779 μm, current = 1447 μm), and all three were plotted.

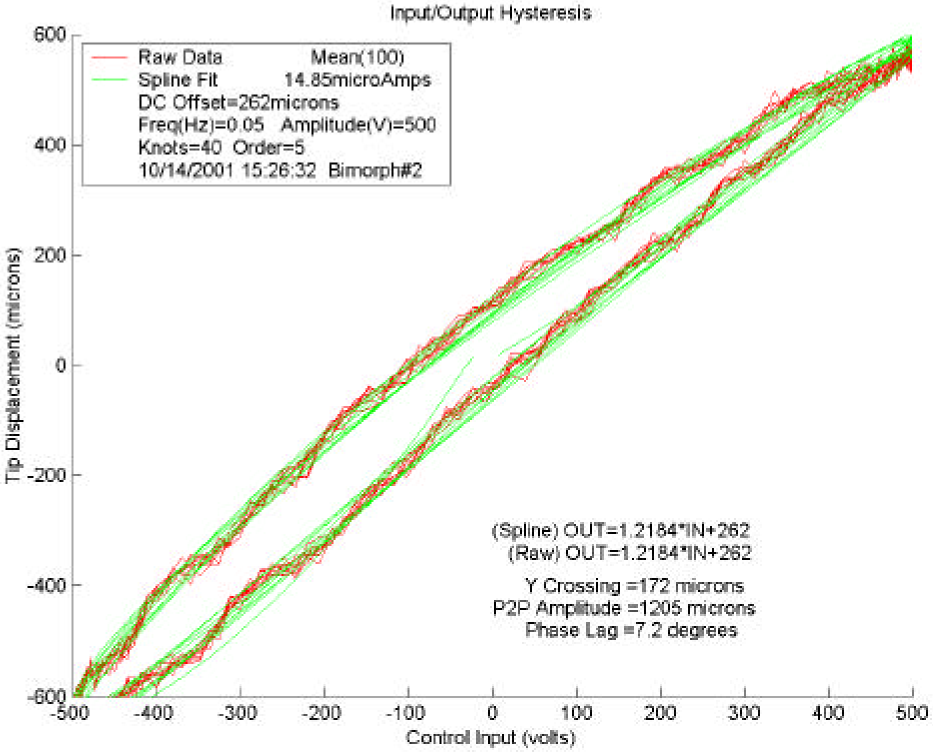

Figure 54. Plot of hysteresis example for a Type C bimorph actuated by an 800-eV, 0.50-Hz, 500-V, and 4.81-mA electron beam.

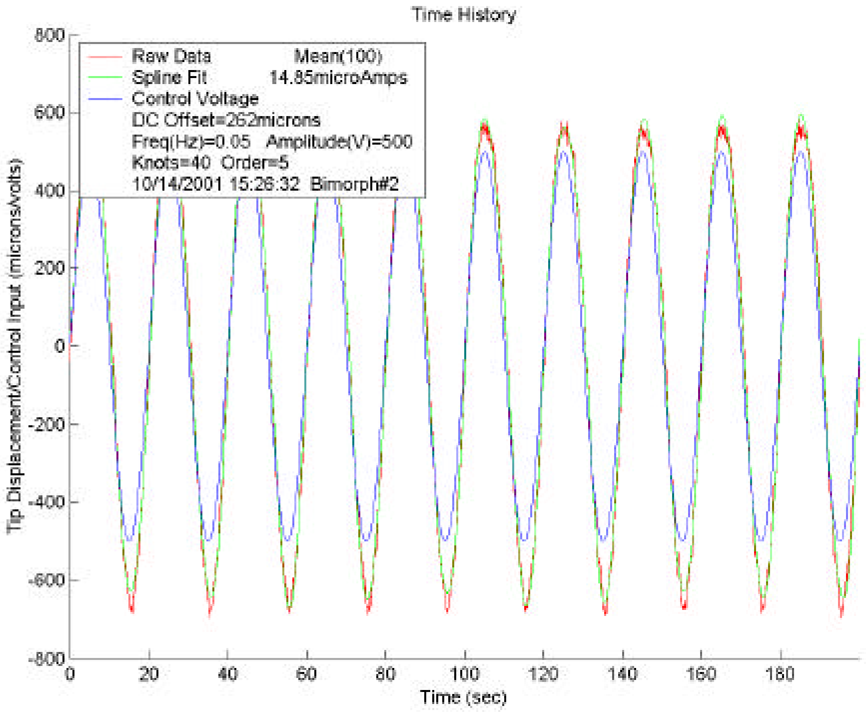

Figure 55. Plot of time history example for a Type C bimorph actuated by an 800-eV, 0.50-Hz, 500-V, and 4.81-mA electron beam.

Figures 56, 57, and 59 show the normalized DC offset control responses to 0.10-, 5.0-, and 14.5-µA electron beam currents, respectively. Certain trends can be seen: as control amplitude increases the DC offset increases, and as the control current increases, the DC offset increases with frequency. These data support the previous current versus deflection and DC offset data.

Figures 59, 60, and 61 represent the normalized amplitude control responses to 0.10-, 5.0-, and 14.5-µA electron beam currents respectively. Certain trends can be seen: the amplitude response increases with both control current and amplitude but rolls off as a result of increased frequency. Again, the displacement actuation is shown to increase with current just as in previous experiments.

Figures 62 (a blank due to bad data and plotting), 63, and 64 represent the phase lag response resulting from 0.10-, 5.0-, and 14.5-µA electron beam currents respectively. A slight trend can be seen (amplified in Figure 63b) that shows increased lag resulting from increased amplitude. The biggest trend is increased lag resulting from increased frequency.

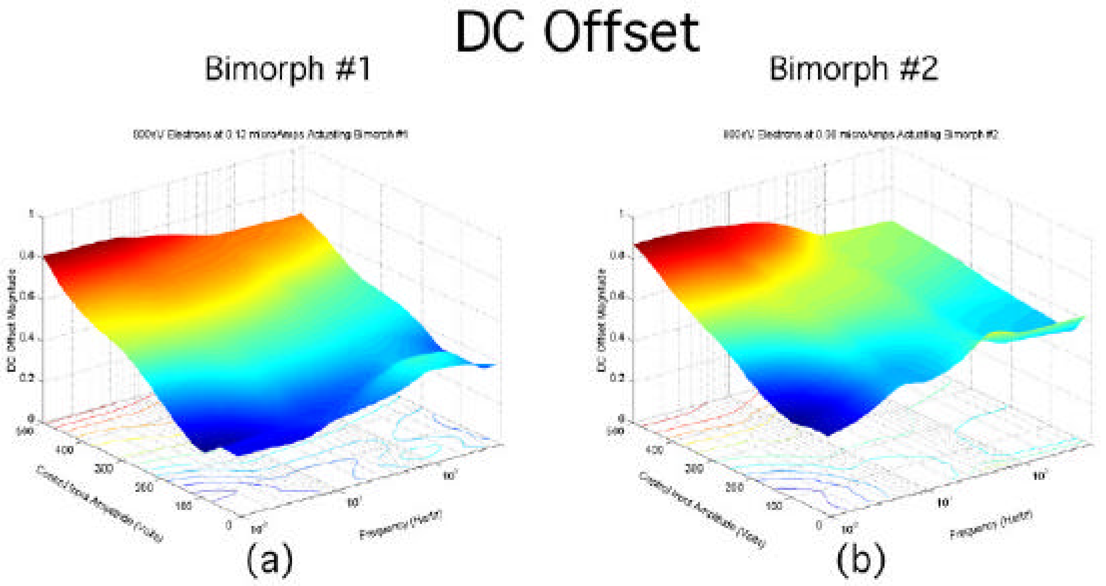

Figure 56. DC offset plots for a low-current actuation controllability experiment on a Type C bimorph.

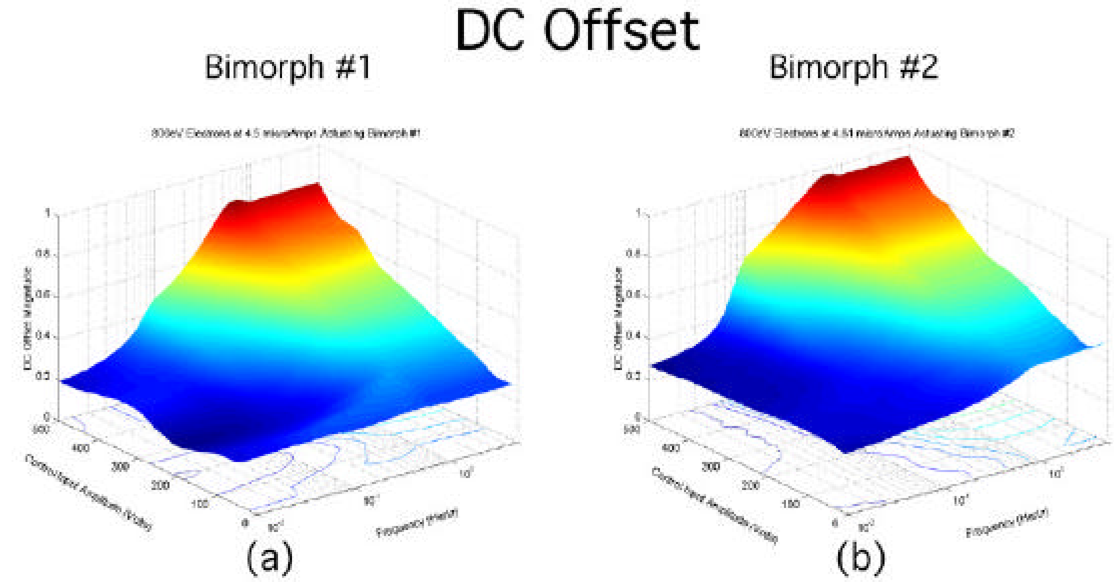

Figure 57. DC offset plots for a medium-current actuation controllability experiment on a Type C bimorph.

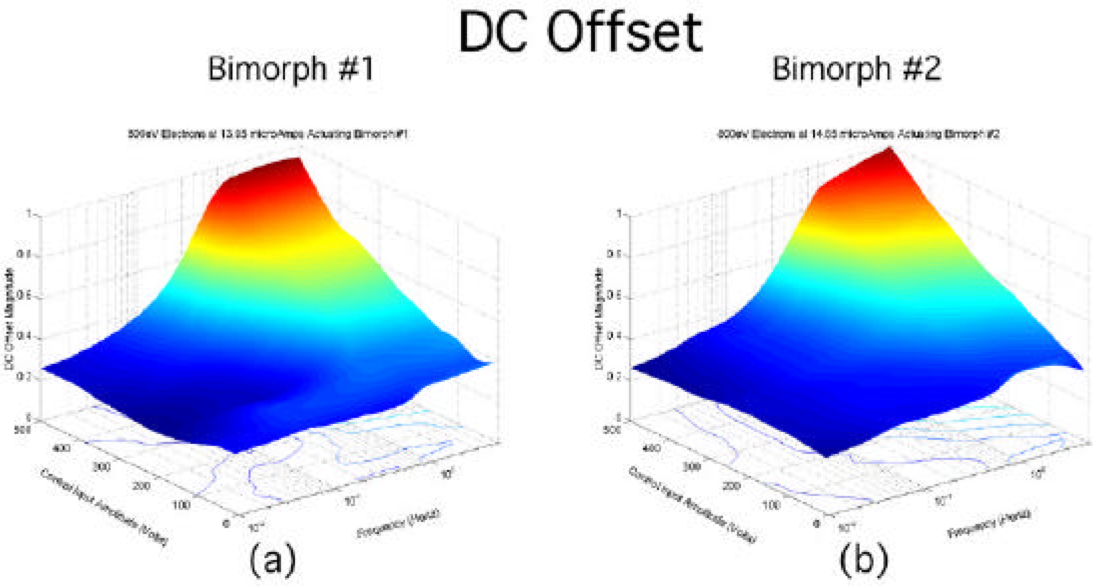

Figure 58. DC offset plots for a high-current actuation controllability experiment on a Type C bimorph.

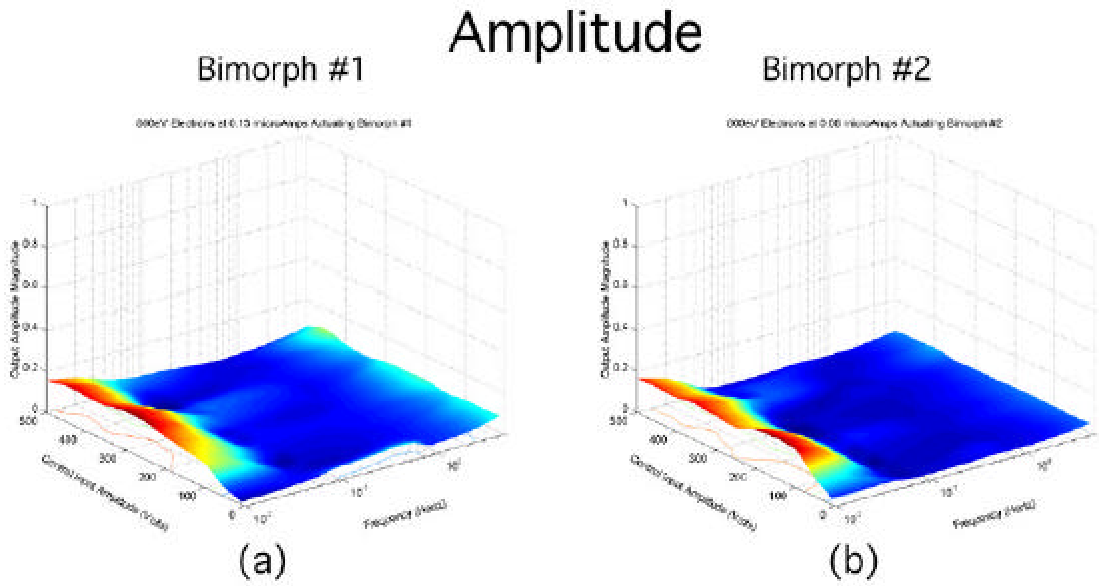

Figure 59. Amplitude plots for low-current actuation controllability experiment on a Type C bimorph.

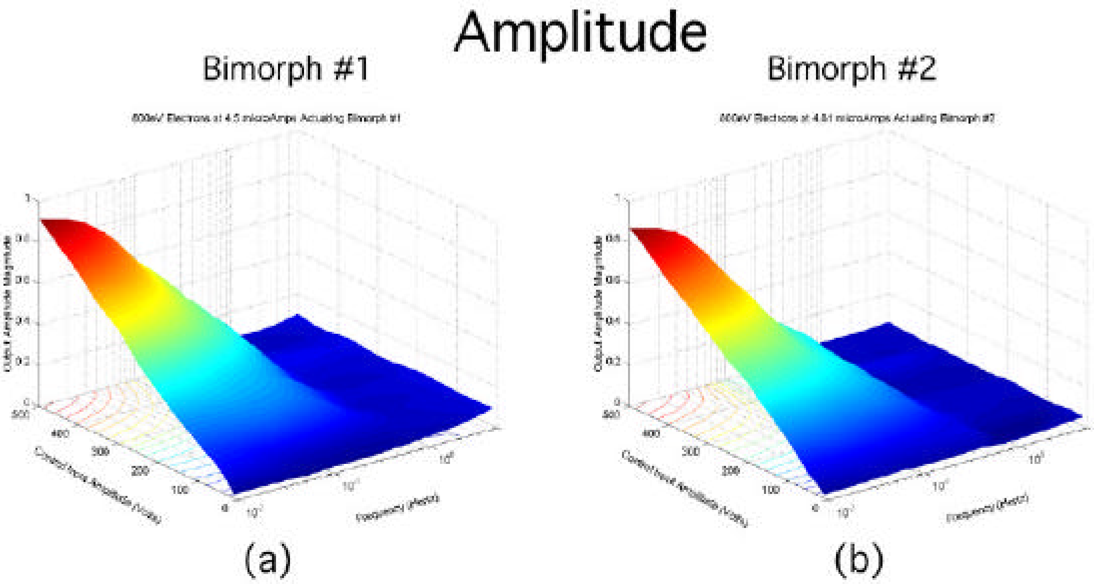

Figure 60. Amplitude plots for medium-current actuation controllability experiment on a Type C bimorph.

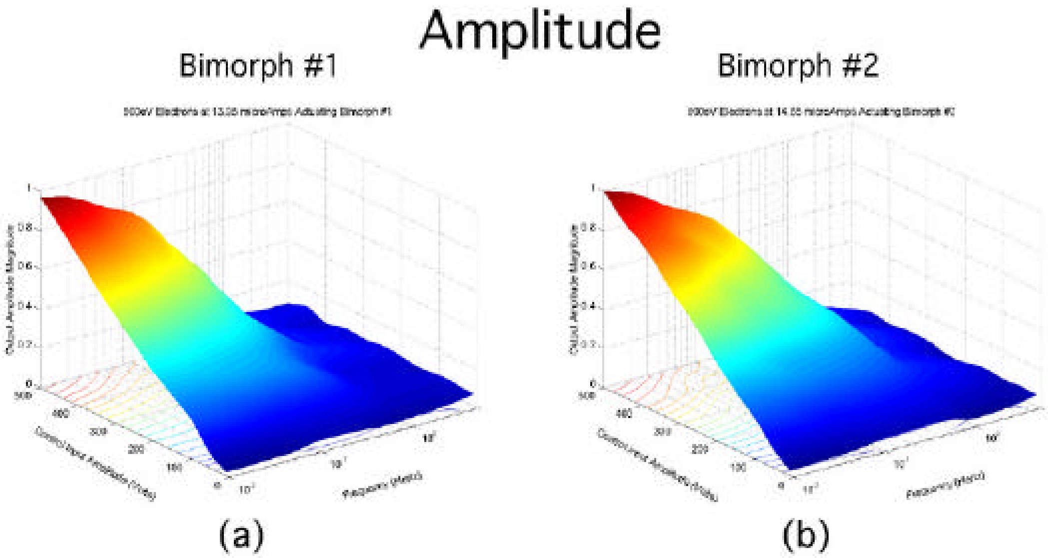

Figure 61. Amplitude plots for high-current actuation controllability experiment on a Type C bimorph.

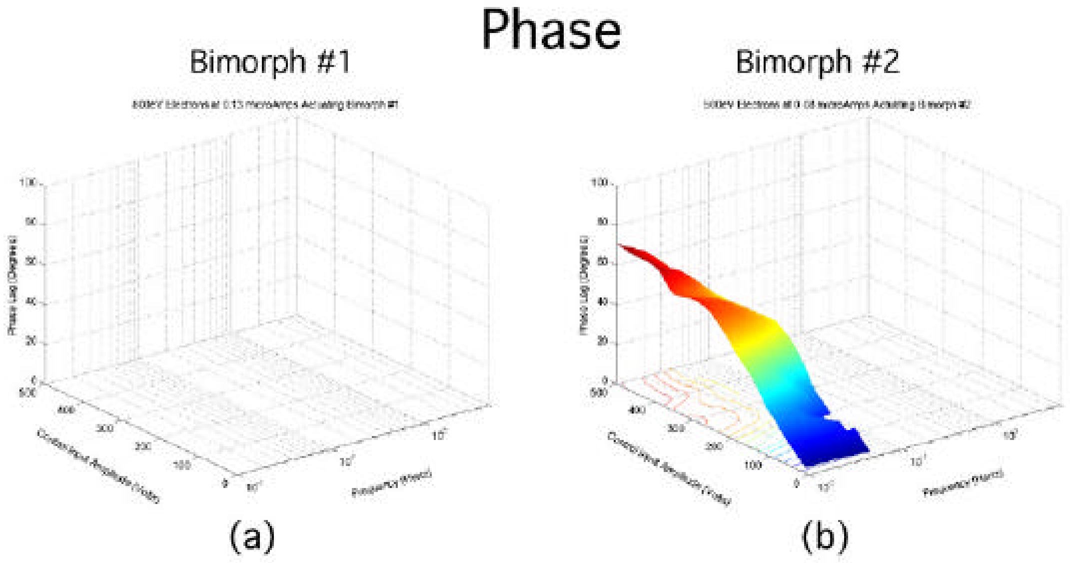

Figure 62. Phase plots for low-current actuation controllability experiment on a Type C bimorph.

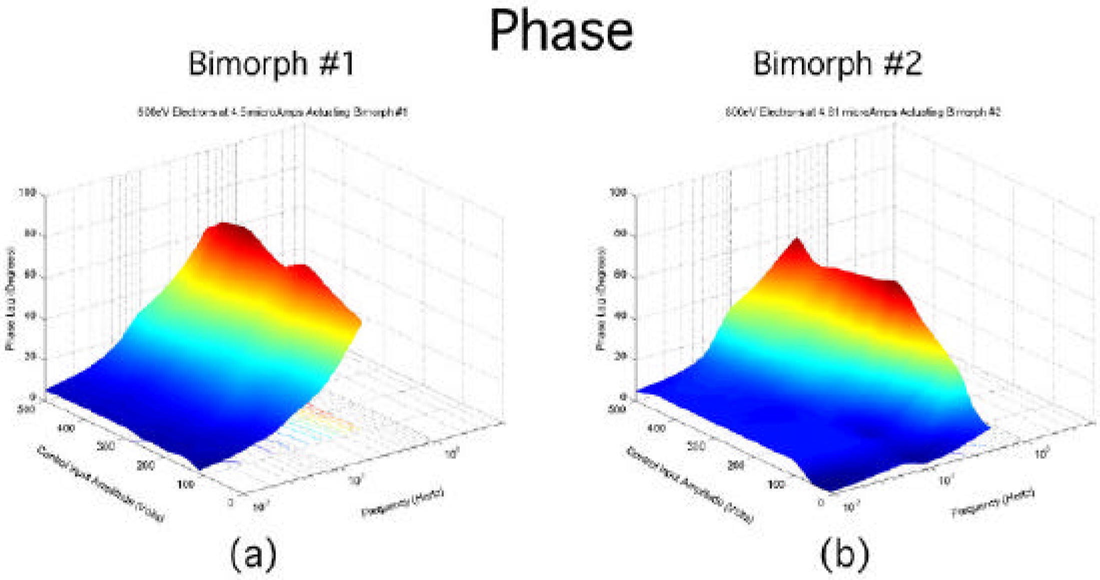

Figure 63. Phase plots for medium-current actuation controllability experiment. on a Type C bimorph

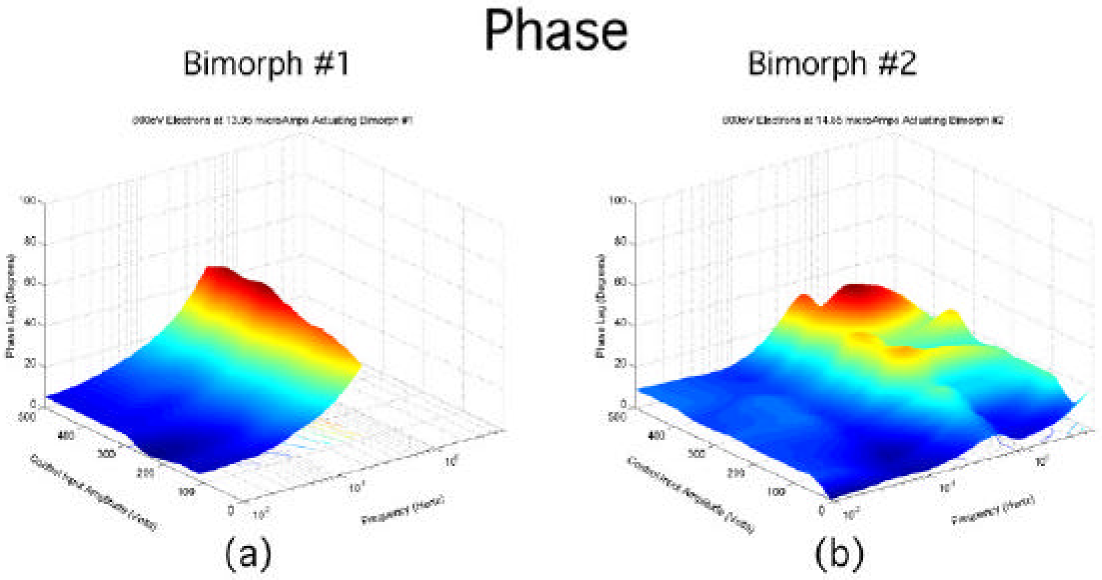

Figure 64. Phase plots for high-current actuation controllability experiment on a Type C bimorph.

Control Capabilities – Discussion of Results

The bimorph calibration data sets were all analyzed, and the local curvature changes were plotted in Figure 65. The figure shows that each energy level (400 eV through 1400 eV) is capable of localized curvature changes of >1.5 meters. The previously shown minimum actuation capabilities of 200 nm integrate well with these gross control abilities for both fine and coarse shape adjustments.

These results relate well with the optics community's need for nanometer-level control actuation. The macrochanges induced would allow thin-film mirrors to be coarsely deployed by optics (nanometer) standards and then finely tuned to final specifications. These data already support the likelihood that a lidar system's surface requirements (700 nm RMS) can be produced.

The actuation slopes (microns/microamps) resulting from control at each energy level are plotted in Figure 66. Bimorph initial charge-up (Region II from the graphs in the section on Minimum Current) occurs with the steepest slope. As energy levels increase, the initial charge-up, Region I, flattens out. At 1400 eV, the DC offset, Region II, becomes level. This directly supports the results from the controllability analyses. As the actuation energy increases, the displacement DC offset increases.

Figures 67, 68, and 69 show the energy transfer relationships from DC offset to amplitude as the frequency increases. Again, the same DC offset vs output amplitude relationship occurs here. The energy total in the control scheme is split into two portions: the constant DC offset and the variable amplitude response. As the frequency increases, the energy transfers from the output amplitude response to the DC offset. The effect of this is the same as that of the current alone. As frequency increases, less time is available for charge to flow (current), and

DC offsets increase as a result of a “cloud” of electrons forming near the surface, which induce weaker electric fields through the material.

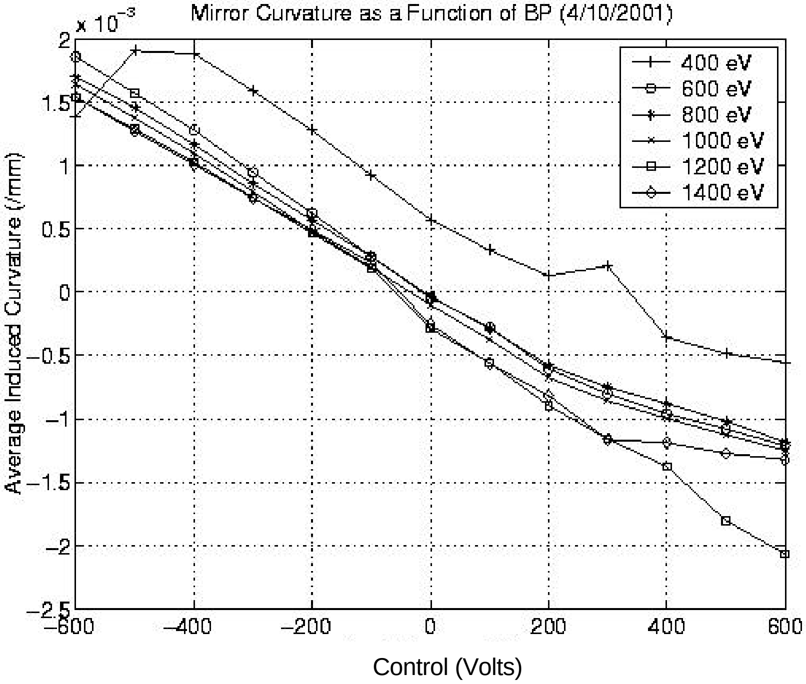

Figure 65. Plot of curvature correction capability of a Type A bimorph.

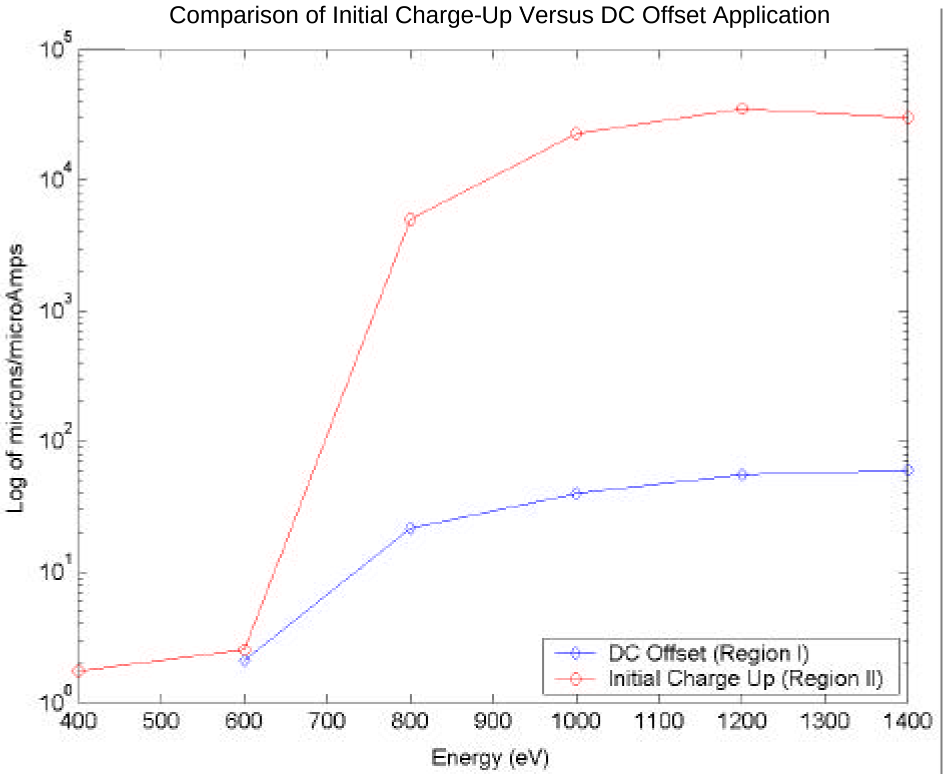

Figure 66. Plot of Region I and II bimorph charge-up as a function of energy.

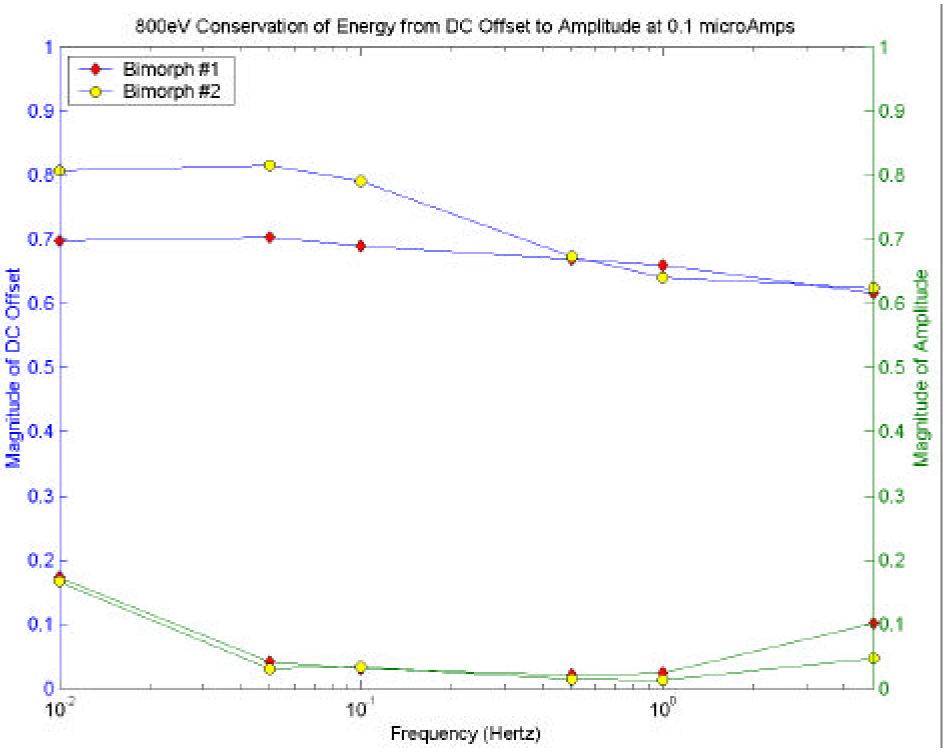

Figure 67. Energy transfer relationship of a low-current actuation controllability experiment using a Type C bimorph.

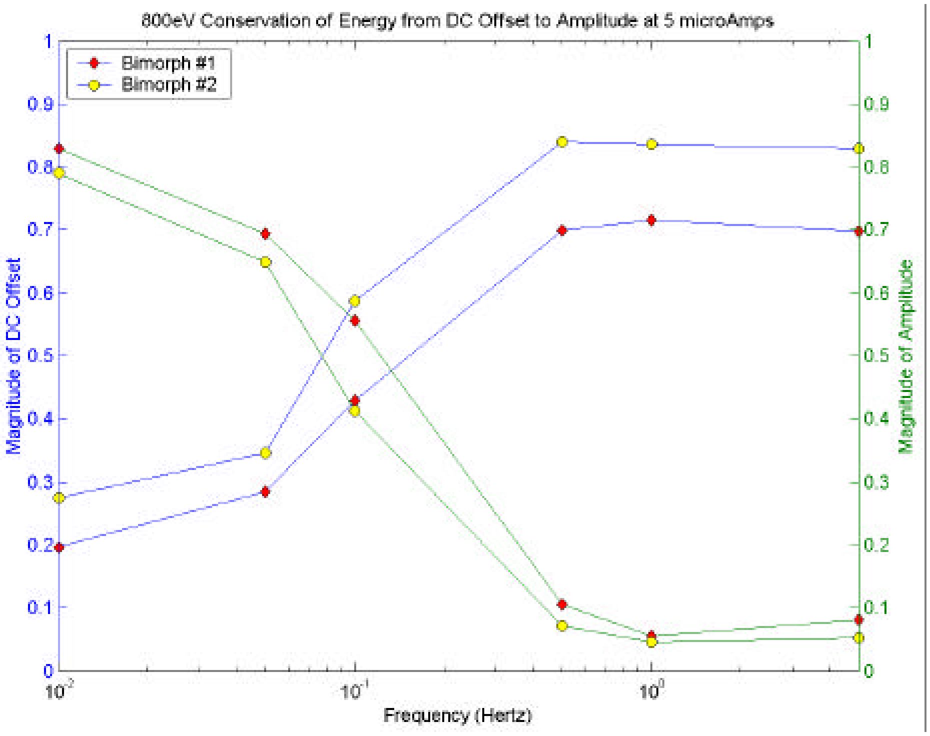

Figure 68. Energy transfer relationship of a medium-current actuation controllability experiment using a Type C bimorph.

Figures 70, 71, and 72 show the same DC offset transfer to amplitude for 0.01-, 0.10-, and 1.00-Hz actuation. The “crossover” currents increase with the input control frequency.

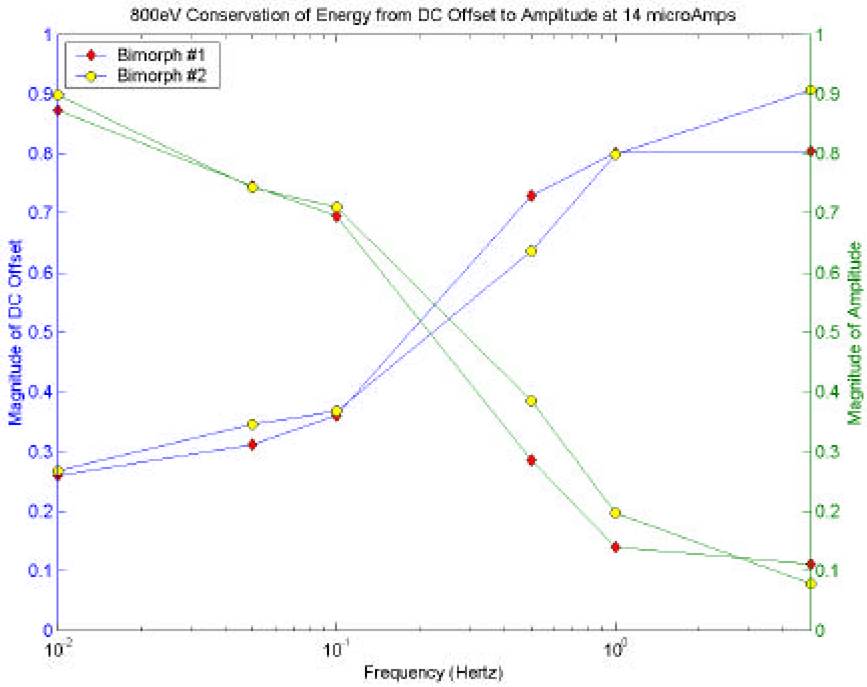

Figure 69. Energy transfer relationship of a high-current actuation controllability experiment using a Type C bimorph.

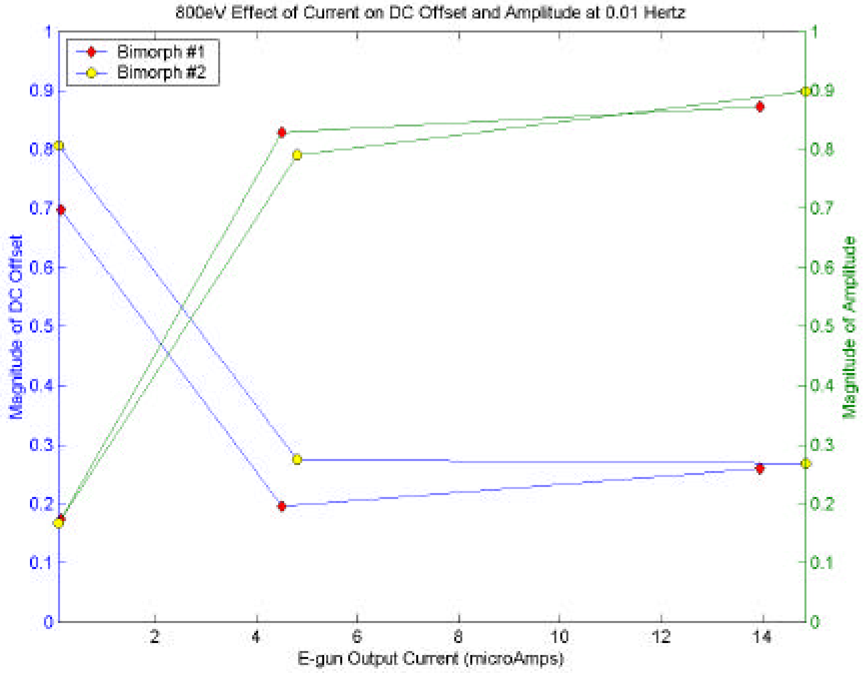

Figure 70. Energy transfer relationship of 0.01-Hz actuation controllability experiment of a Type C bimorph.

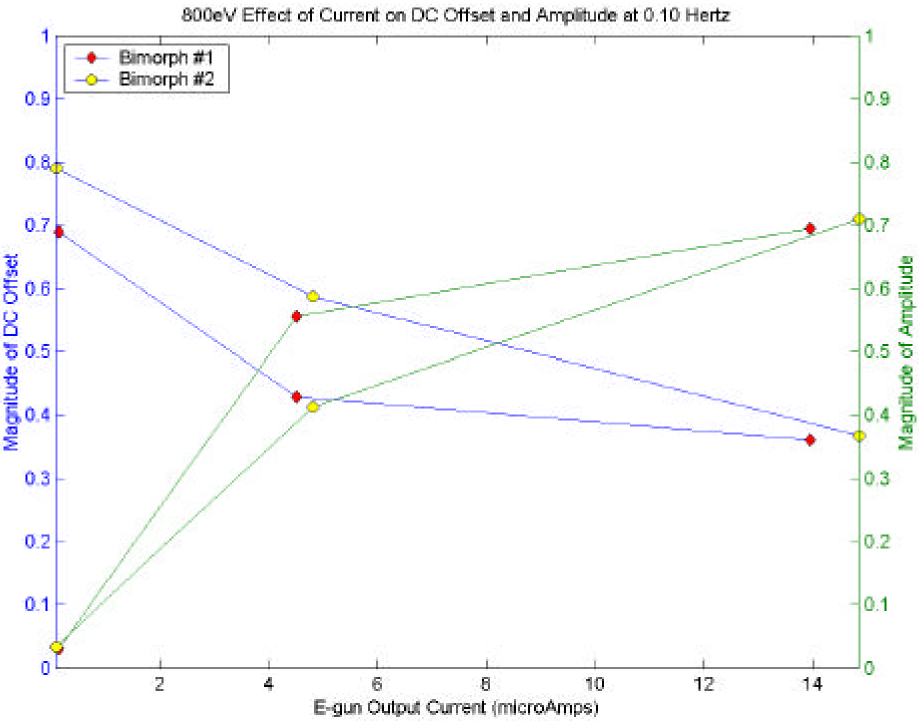

Figure 71. Energy transfer relationship of 0.1-Hz actuation controllability experiment of a Type C bimorph.

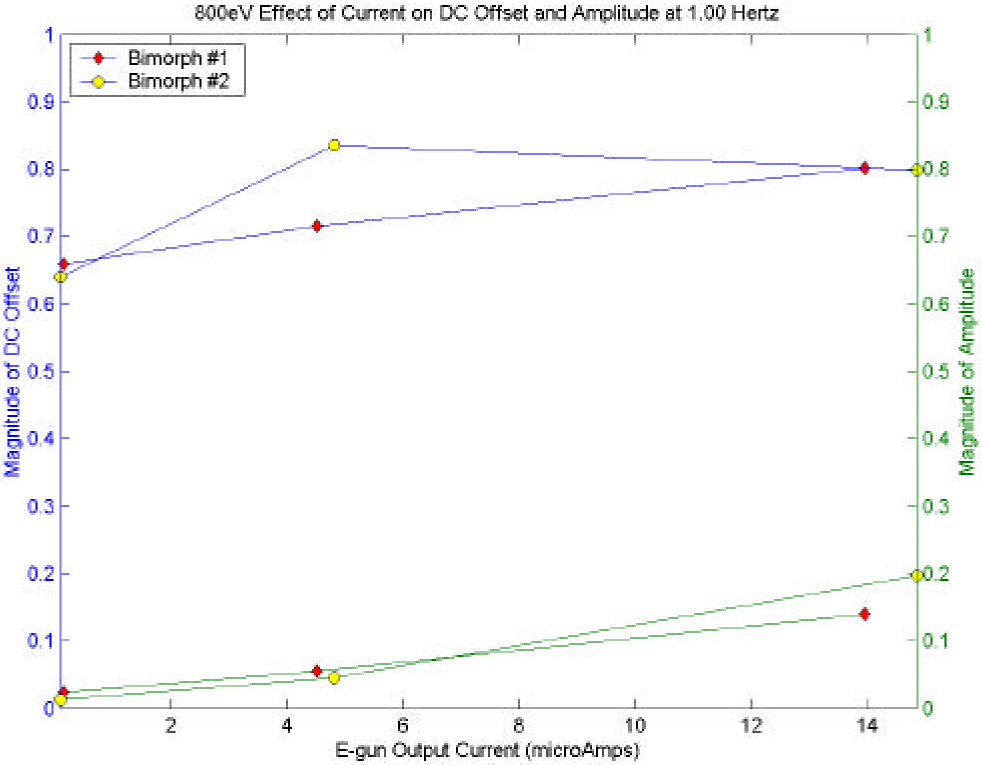

Figure 72. Energy transfer relationship of 1-Hz actuation controllability experiment of a Type C bimorph.

The behavior that occurred in the other experiments occurs here as well. As more charge becomes available to “stick” to the bimorph, the output displacements increase, and the DC offset (deflection resulting from the electron “cloud”) decreases.

Controllability of PVDF Thin Film with Multiple Regions of Control

Two main sets of experiments, programmed with LabVIEW programming software, were directed at determining how controllable a PVDF thin film is when it has multiple spatial regions of control. Toward that end, an empirical set of experiments investigated the effects of focusing an electron gun on one region of the thin film to actuate it. The electron gun was focused as well as possible and then the voltage on the backside of the film was altered in large (600-V) and small (<200-V) increments.

The second set of empirical experiments studied the mechanical response of one region as the electron gun was focused with varying electron energies onto each of five spatial regions of the thin film; the response of the region closest to the cantilevered support was measured. For each region, seven different electron energies were used: 800–1400 V in 100-V increments. For each electron energy and region, the voltage on the backside of the film was incremented in 4-V increments from 0 to –600 V, then from –600 to +600 V, and finally from +600 V back to 0 V. The data collected were thus a hysteresis loop describing the response of the region nearest the fixed support to the combination of the altering voltage on the back of the film and the electron gun focusing onto the given region. Each hysteresis loop was run five times for a given region of focus and electron energy to see how repeatable the data sets were. The results of the dataset are in 175 data plots.

Focusing onto One Region

Optimizing the Spot Size

When focusing the electron beam onto the film, it is impossible to perfectly focus the electrons to one point. In fact, because electrons, like photons, have particle-wave duality, the primary electrons leaving the electron gun exhibit a diffraction pattern (Hadinata 2001), as shown in Figure 73. Instead of showing the contour across the film surface, Figure 73 shows the contour as a function of x- and y-deflection voltages, which correlates to an angular spread emanating from the electron gun tip. This allows the plot to not depend on the distance from the electron gun tip to the film surface.

Although the grid voltage, in conjunction with the focus voltage, can be used to remove most of the surrounding haze, primary electrons will always strike more than one region, and some regions will receive more electrons than others.

To see where the electrons would strike the surface, the front side of the film was coated with phosphor, which gave off blue light when struck by electrons. This light was visible to the naked eye only when the electron beam current density on the film surface was great enough.

For example, 20 electrons striking the surface did not give off enough light to be seen. But when the beam current was large enough, the electron haze could be seen. This allowed the user to increment the grid and focus voltages until the smallest and faintest spot was seen. For these experiments, the optimal beam current was ~1 ± 0.5 μA.

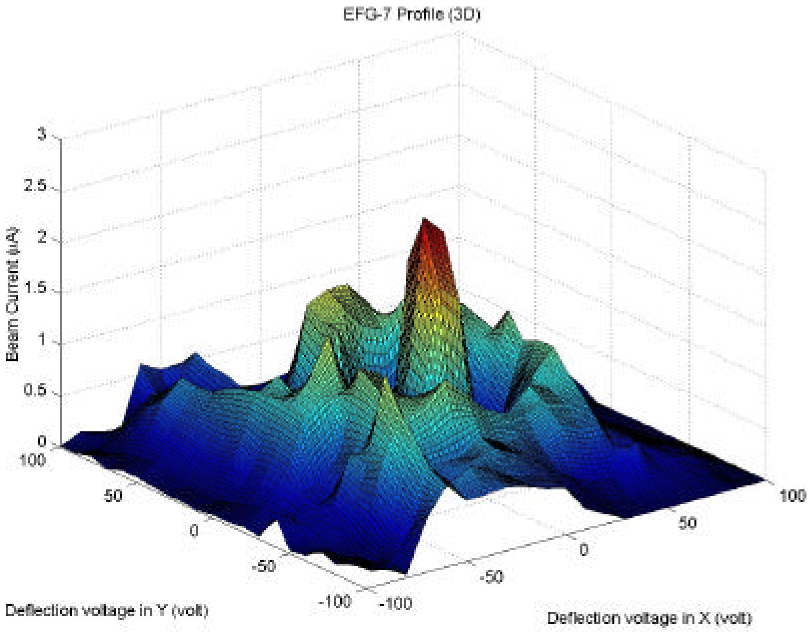

Figure 73. Primary electron distribution pattern (Hadinata 2001).

Raising the grid voltage creates a greater negative charge to slow down or repel the electrons leaving the electron gun cathode. It will prevent all electrons having up to a certain energy from leaving the electron gun (see Figure 74).

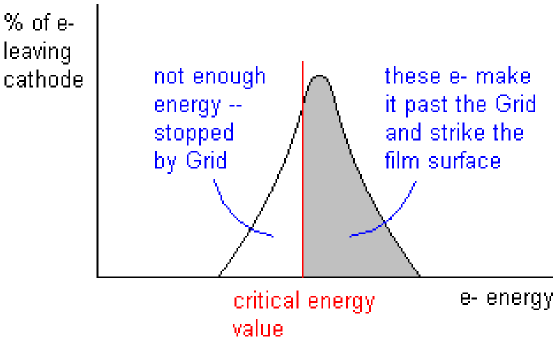

Figure 74. Sample electron energy distribution with grid cutoff.

Electrons with energy greater than the specified energy will still strike the surface, making it impossible to remove all of the haze. To get very close to removing the *visible* haze, this critical energy value can be shifted up so only the highest-energy electrons can hit the film (see Figure 75).

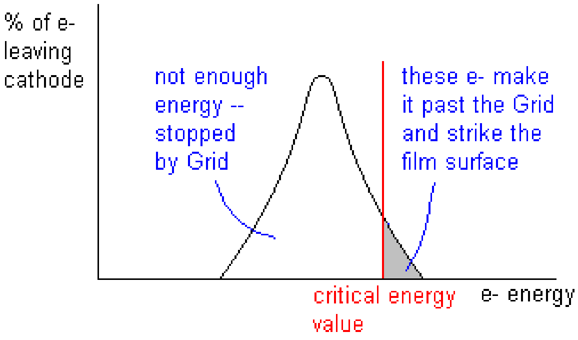

Figure 75. Sample electron energy distribution with grid cutoff shifted up.

This method removes most of the visible haze when the electrons are focused as well as possible. However, too much or not enough focusing will also cause problems, as shown in Figure 76.

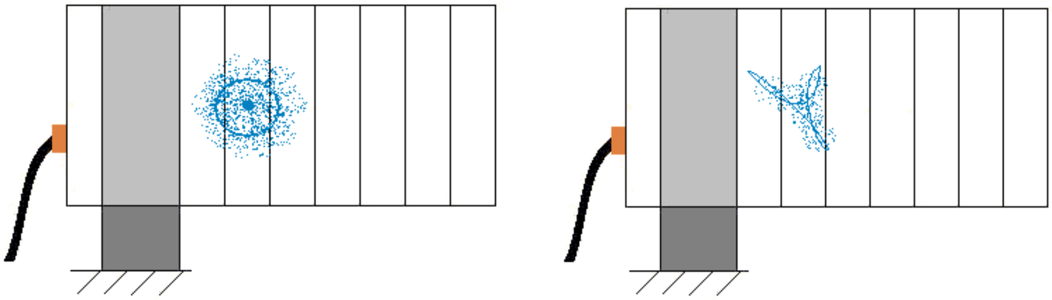

(a) (b)

Figure 76. Electrons not focused enough (a) and focused too much (b).

It is important to keep in mind that Figure 76 depicts the visible haze—it cannot be assumed that the visible haze represents all electron interactions with the surface. It must be assumed that there is a haze of electrons always striking the whole film, because it cannot be proved otherwise in this research. Furthermore, secondary electrons, or electrons escaping the film surface, are likely to land on other regions of the film as well. The physics of this setup make it impossible to prevent electrons intended for the actuation of one region from striking another.

Spot Movement

Focusing the optimal electron spot to the desired position depends on many variables: grid, focus, x- and y-deflection voltages; electron energy; and control voltage. The x- and y-deflection voltages were set so that the central electron spot would strike the centroid of each region, while the grid and focus voltages focused the electron beam as much as possible. All of these values are dependent on the electron energy and control voltage, and though it is not immediately apparent, the control voltage affects the electron energy by causing primary electrons to be either attracted to or repelled by the film. Thus the electron energy set by the electronics is not necessarily the final electron energy when the primary electrons strike the film; they may have sped up or slowed down between leaving the electron gun and reaching the surface.

For example, an optimal electron spot for 1200 eV and 0 control volts will change when the control voltage is abruptly changed to +600 V. A black-and-white filtering camera connected to a PC was used to get actual footage of the spot-changing location. It was set to take a series of images as rapidly as the electronics would allow (it was programmed to take the images with no time delay between them, but the computer system had considerable data-taking delay). Figure 77 shows two images of the film, one immediately before changing the control voltage to +600 V, and one immediately afterward. Figure 78 shows the same thing for a different film. It can be seen for both films that the emitted phosphorescent spot of light gets brighter and moves slightly. It gets brighter because the primary electrons gain energy when the control voltage increases, so more electrons reach the film and with more energy. The spot moves slightly because the x- and y-deflection voltages, which should have been altered to compensate for the energy change, were not altered in this experiment.

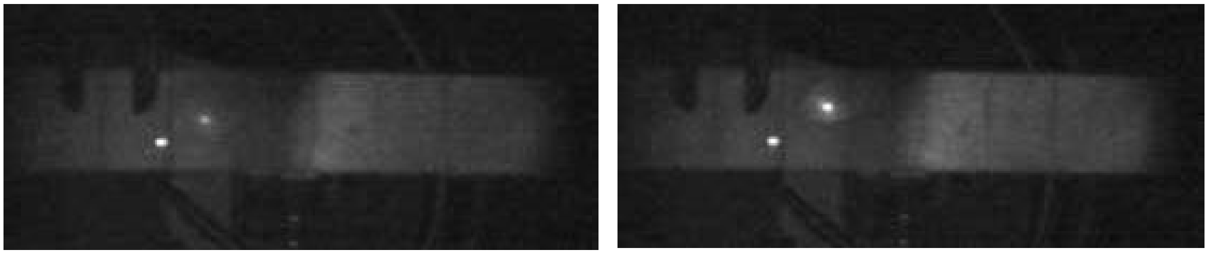
(a) (b)

Figure 77. Small film before (a) and after (b) changing control voltage from 0 to 600 V.

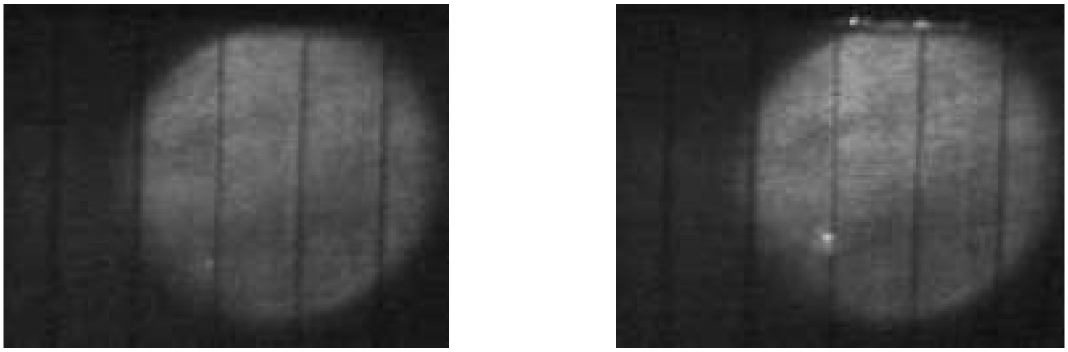
(a) (b)

Figure 78. Large film before (a) and after (b) changing control voltage from 0 to 600 V.

Because a sequence of images in this paper would not adequately display the spot movement, a plot of the spot was made in Figure 79. Here the x- and y-axes are physical dimensions of the film surface itself, and the plot shows how the spot moved in time—*x* and *y* are both functions of time here.

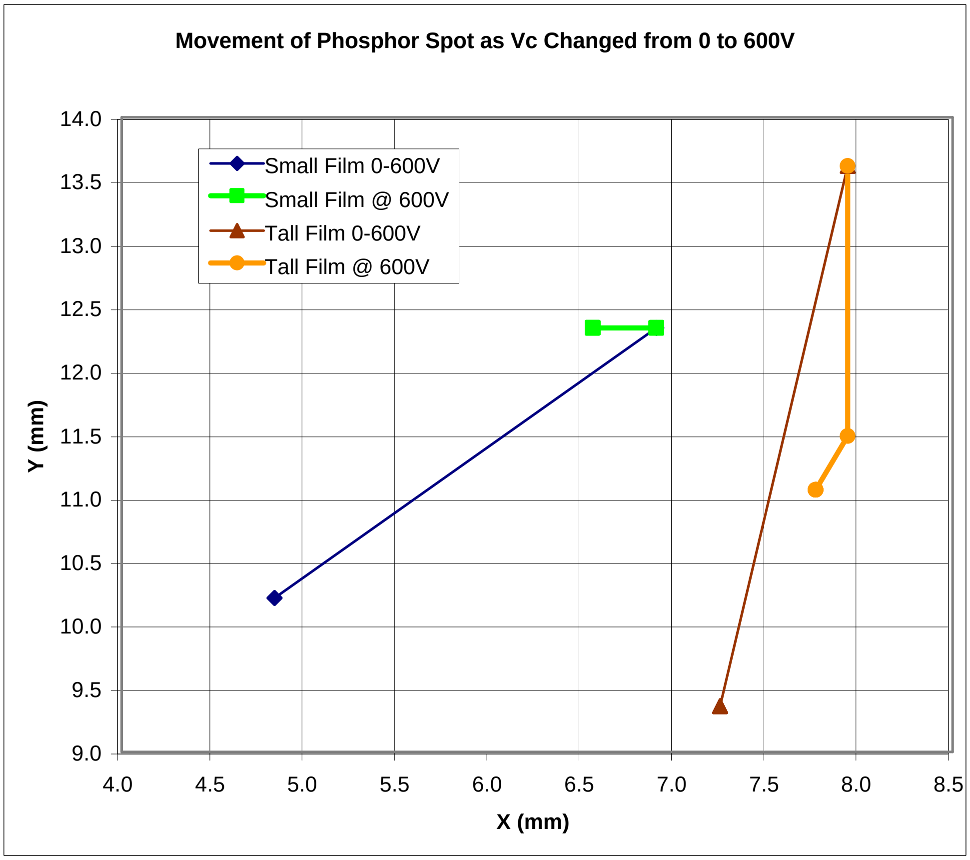

Figure 79. Movement of phosphor spot during control voltage change from 0 to 600 V.

This plot shows data for two different films. The blue/green plot is the spot movement for the film discussed in the third section of this report. The brown/orange plot is the spot movement for an identical film, except that the film has a height of 6 cm and has only one region along its 12-cm length. The blue and brown lines represent the movement of the spot when the control voltage was abruptly changed from 0 to 600 V. The green and orange lines represent the movement of the spot as the control voltage was kept constant at 600 V; in other words, they show transient data of how the spot tended toward its steady-state position. The relative slopes of these four curves are not significant in this data, because the spots were initially focused at very different x and y locations; therefore, when the voltage was changed, the spots would not necessarily move in the same direction. Also, the relative positions have no significance here, as they have been shifted to optimally fit on the same plot.

Two important observations can be found from Figure 79. First, the length of the brown line is greater than that of the blue line. Second, the length of the orange curve is much greater than that of the green curve. Both observations can be attributed to end effects—because the first film was only 20 mm tall while the second film was 60 mm tall, it can be assumed that the electric field lines around one film were very different from those around the other film. It seems that end effects limit the movement of the spot. This distinction may help in deciding if a thin-film mirror that is controlled using this approach should leave a rim of "inactive" material to prevent end effects.

Focusing Incorporated into the Controls

The fact that the location and size of the electron spot on the film was dependent on several variables meant that equations had to be found for programming the controls. The independent variables used were electron energy and control voltage. These were set to a certain value, and then the other variables were altered until the optimal spot size and location were obtained. Then control voltage was incremented between –600 V and +600 V, and again, the dependent variables were altered, resulting in one equation. The electron energy was changed to its next value, and the whole process was repeated.

The relationships found were not exactly linear but were very nearly so; therefore, a linear regression was used to find an equation. This meant that the spot would change slightly; however, later observations showed that the spot change was nearly inconspicuous and would not cause issues with the control. After these relationships were programmed into the controls, the electron spot would remain nearly optimal for each new electron energy and/or control voltage.

Multiple Regions

The Effect of All Regions on Region 1

The following set of experiments was designed to see how one region of the film would be affected by the other regions. Clearly, actuating one region will affect the displacement of all regions closer to the free end. But it was unclear how such actuation would affect the regions between the fixed end and the actuated region. According to elementary beam theory, these regions should be unaffected, assuming the piezoelectric effect can be modeled by application of a pure moment. However, such analysis does not account for the distribution pattern of primary electrons, nor does it account for secondary electron emission—where these electrons land and how they would influence other regions that were not meant to be actuated. The goal of these experiments was to see how Region 1 was influenced when the electron beam spot was focused on each of Regions 1 through 5, in turn.

The Keyence laser displacement sensor was set up to measure the displacement of the far edge of Region 1 (i.e., the edge not fixed, adjacent to Region 2). Hereafter, this point will be referred to as Point 1. Originally, the center of Region 1 was measured, but this choice was altered so more deflection could be observed. Indeed, according to elementary beam theory, Point 1 should experience four times more displacement than the center of Region 1 because it is twice the distance from the fixed support. A program was written in LabVIEW to set the control voltage, then to fire electrons at a given region for a set time of 400 ms, and finally to take several measurements of the displacement of Point 1. The time of 400 ms was chosen because it is the time it takes for noticeable actuation to begin (Hadinata 2001), as this research confirmed. This sequence was run in a “for loop” while the control voltage was incremented in 4-V increments from 0 to –600 V, –600 to +600 V, and finally +600 to 0 V. This process was run five times for each electron energy level, from 800 to 1400 eV in 100-eV increments. Going to negative voltage first and then incrementing into positive voltage works better because, when using positive voltage, the charge built up on the surface remains much longer than when using negative voltage. Therefore, it seemed that by using negative voltage first, more displacement would be observed.

Before continuing the discussion on the data collected, five figures must be described that are used throughout the following. For each data set given, one or more additional figures will be shown to visually describe where the primary electron peak was focused and where measurement occurred. The measurement location, indicated by an “M” in the figure, will always remain the same (Point 1), while the actuation location, indicated by an “X” in the figure, will change for each data set. Figure 80 shows all five scenarios and describes where the primary electron peak was focused.

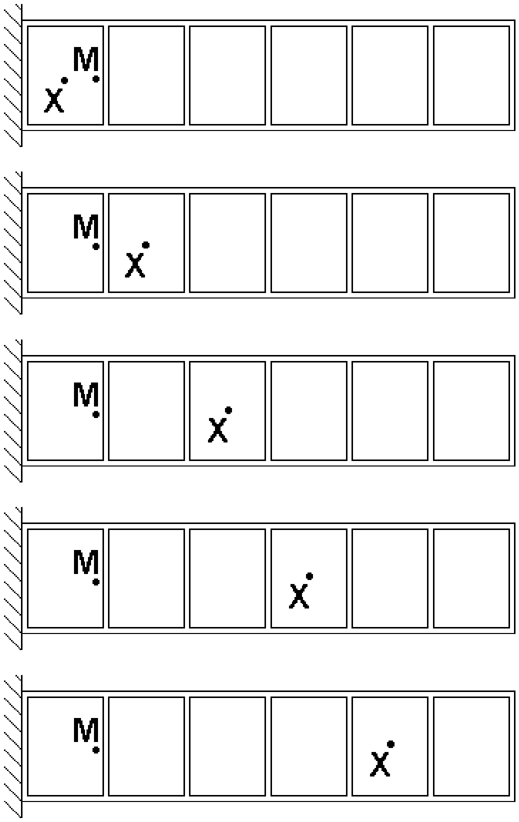

Primary actuation (X) of **Region 1**

Primary actuation (X) of **Region 2**

Primary actuation (X) of **Region 3**

Primary actuation (X) of **Region 4**

Primary actuation (X) of **Region 5**

Figure 80. Actuation (X) and measurement (M) for each scenario.

Now, continuing the discussion of data collected, a sample of the data is shown in Figure 81a below. Here Region 3 is being actuated with 1200 eV while the displacement of Point 1 is measured. These data have considerable noise because several measurements were taken at each increment. To reduce the noise in the data, the average displacement at each control voltage was found and plotted versus control voltage. Also, to more effectively see the hysteresis loop, the plot was colored blue when the control voltage was decreasing and red when the control voltage was increasing. The same plot from Figure 82a was refined with these techniques and is shown in Figure 81b below. Note the actuation (X) and measurement (M) locations indicated in the figure in the top right corner.

Actuation (X) and Measurement (M):

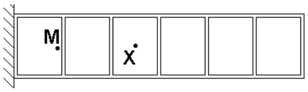

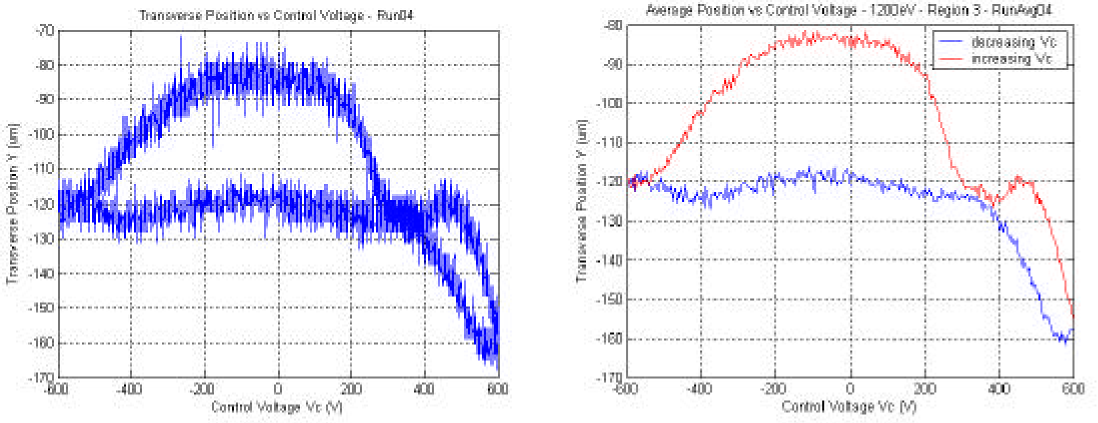

(a) (b)

Figure 81. (a) Raw data and (b) refined plot examples of interregion interaction.

The improvement in clarity from Figure 81a to 81b is obvious. In the raw plot, it is difficult to distinguish whether the top of the second "loop" continues from the top or bottom of the first loop. By refining the data, it is clear that it continues from the top of the first loop. This is one justification for the refinement of the data; it is not always advantageous to alter raw data, but in this case it is. This refinement also distinctly shows when the control voltage is increasing or decreasing, making the hysteresis determination evident. Because of these advantages, the raw data is not presented hereon; rather, the rest of the data presented has been refined using the method described above

Charge-Up Effects

The five plots shown below are all plots of transverse displacement of Point 1 verses control voltage while Region 1 was actuated with 800-eV electrons. The purpose of showing all five plots is to see how time influences the data—time is the only change from one plot to the next. Figure 82a (RunAvg00) was run first and is quite different from the rest because no charge had yet been applied to the surface before this data was taken. Figure 82b–e (RunAvg01 through RunAvg04) all look very similar. Thus there is clearly a charge-up effect taking place here. Also, one very subtle trend is that the plots slowly shift to the left. In Figure 82b, the center of the peak occurs at a control voltage of –200 V. However, by Figure 82e, this peak has gradually moved to –230 V. This same tendency occurs for all electron energies used and when actuating all five regions.

This trend can be explained by considering the electric fields that are built up on the film. The shift to the left means that, to obtain the same displacement, a lower control voltage, or more negative charges on the back of the film, is needed. To get the same displacement, negative charges on the front of the film as well. In other words, the number of electrons that however, the electric field through the film must be the same. Therefore, there must be more

Actuation (X) and measurement (M):

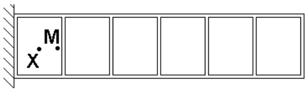

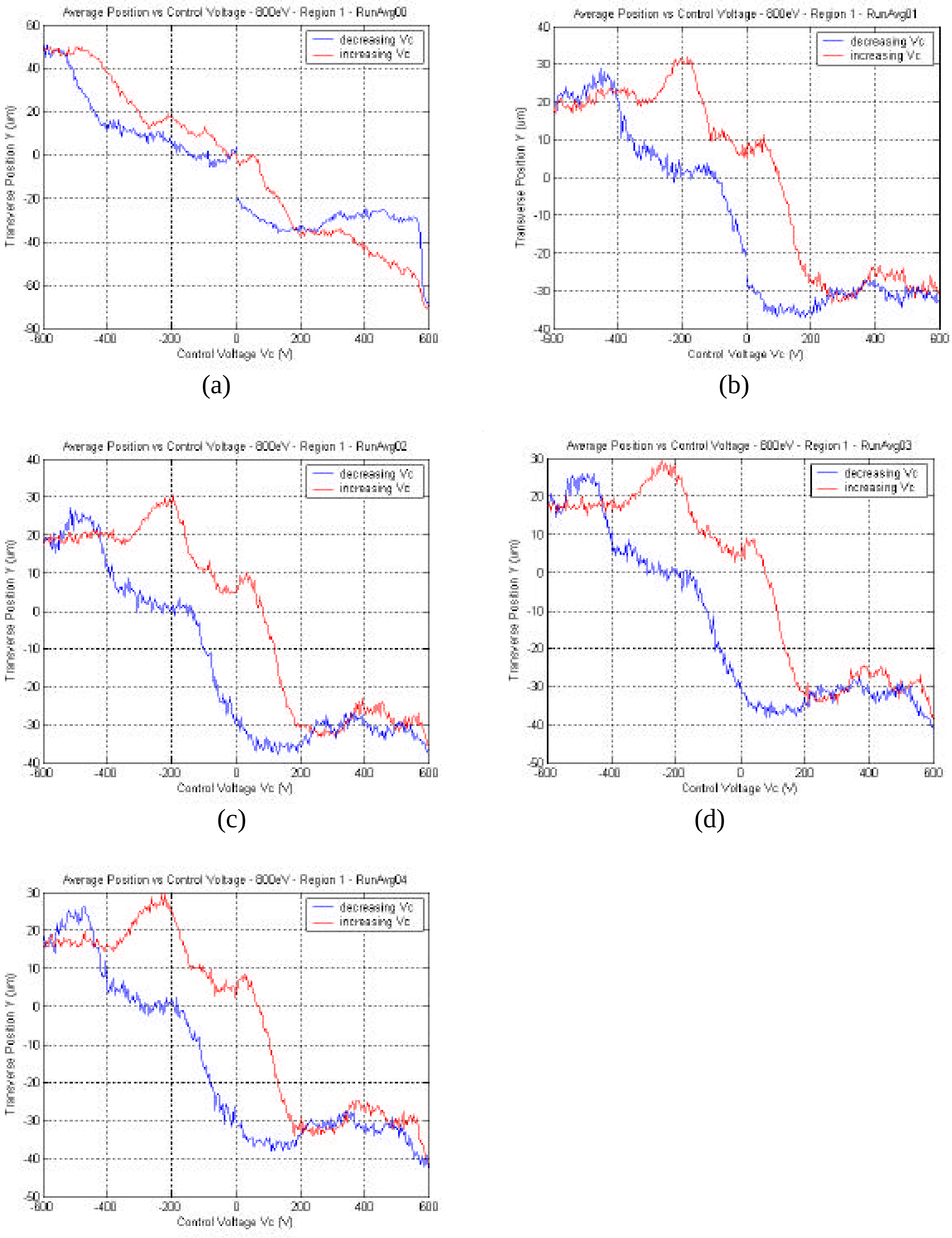

(a)

(b)

(c)

(d)

(e)

Figure 82. Displacement vs control voltage when actuating Region 1 with 800-eV electrons.

negative charges on the front of the film as well. In other words, the number of electrons that can be held on the film surface (both front and backside) increases gradually with time as the film is continuously actuated.

The Effect of Electron Energy

The plots in Figure 83 show the effect of changing electron energy while actuating the same region, Region 1 (the only variable between plots is electron energy). These plots are each RunAvg04 (refer to previous plots), or the last of five plots taking the same data. *Note that from figure to figure, the vertical scale is not the same*; the axes were scaled automatically to see maximum data in the allotted space. This is important because the total range of motion for each figure is not the same. As will be shown, the range of motion generally increases with electron energy when the electron beam is focused onto Region 1.

Figure 83 shows that as electron energy is increased between 800 and 1400 eV, the hysteresis loops become tighter. In other words, hysteresis becomes less prominent as electron energy increases toward 1400 eV. Such a trend indicates that controllability becomes more plausible as electron energy increases toward 1400 eV, because the controller has to “jump around” less to reach the desired position.

Similar plots were obtained when actuating each of the five regions and again measuring the response at Point 1. The minimum, maximum, and range values of these plots were obtained, entered into a table, and graphed to more easily compare the effect of each region’s actuation on Region 1 (see Table 4, Figure 84, and Figure 85).

Actuation (X) and measurement (M):

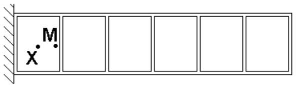

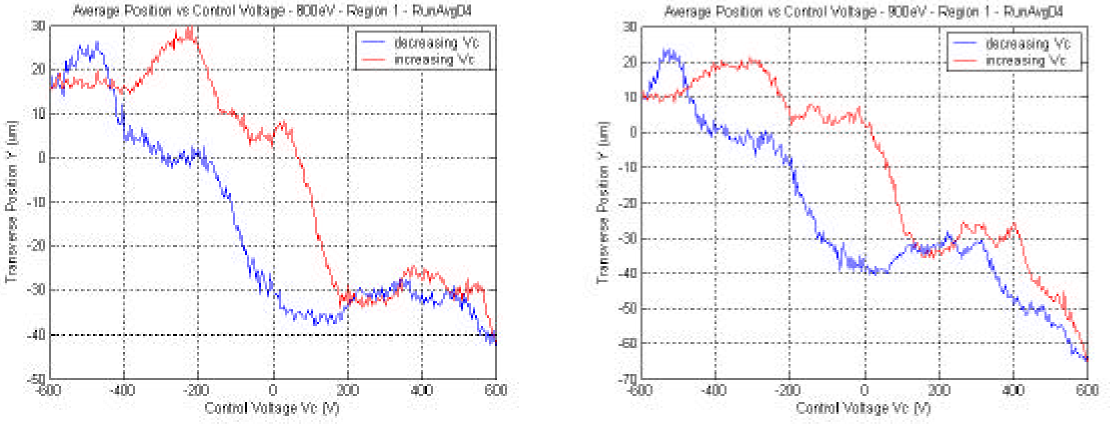

(a) (b)

Figure 83. Displacement vs control voltage when actuating Region 1 with various eV electrons.

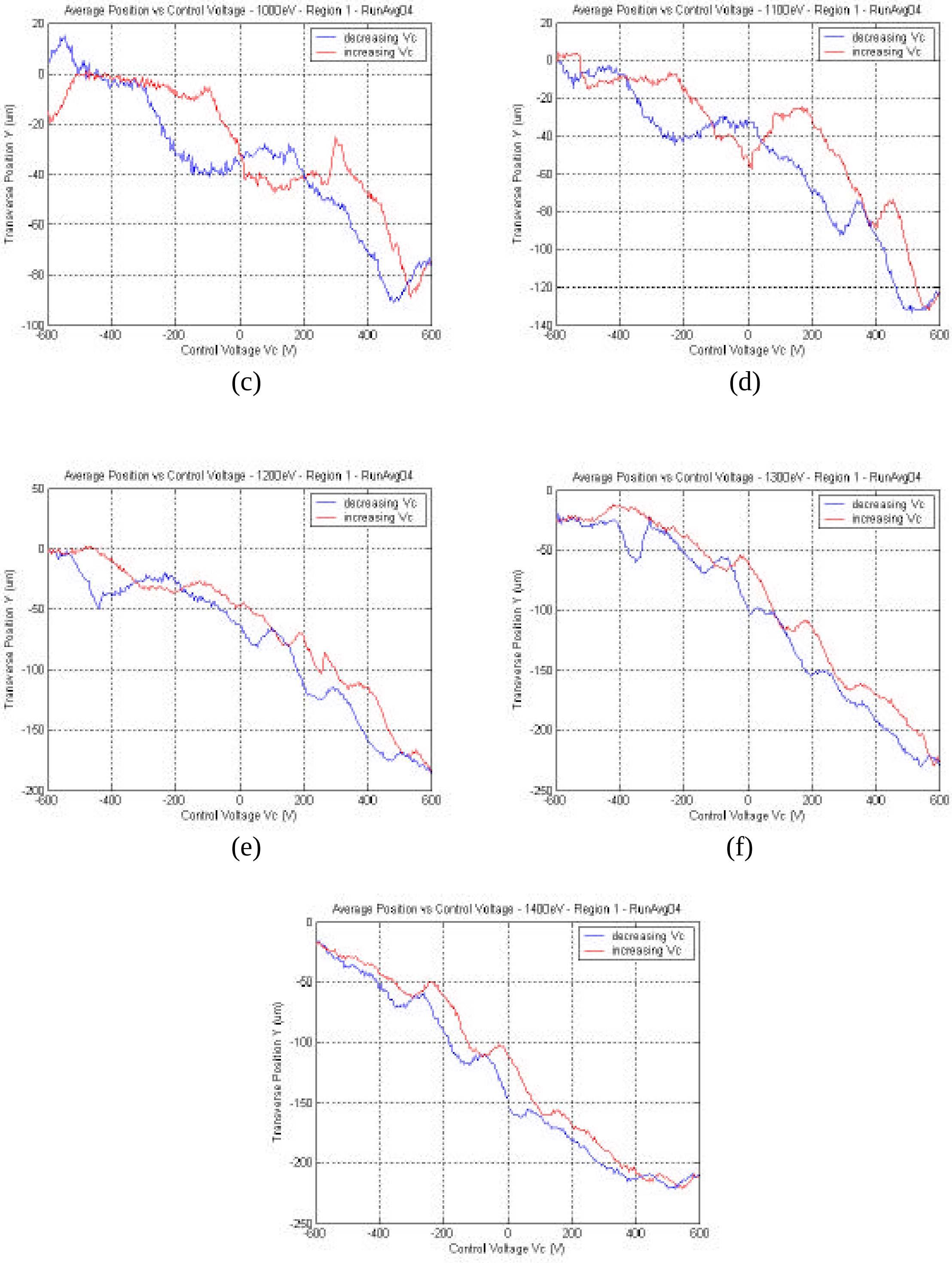

(c) (d)

(e) (f)

(g)

Figure 83 (cont.). Displacement vs control voltage when actuating Region 1 with various electron voltages.

Table 4. Minimum, Maximum, and Range for Each Plot of Displacement vs Control Voltage

	Region 1			Region 2			Region 3			Region 4			Region 5		
eV	min	max	range (µm)	min	max	range (µm)	min	max	range (µm)	min	max	range (µm)	min	max	Range (µm)
800	-42	30	**72**	-46	26	**72**	-148	-39	**110**	-135	-70	**65**	-138	-90	**48**
900	-65	24	**89**	-58	46	**104**	-147	-56	**91**	-130	-61	**69**	-133	-64	**69**
1000	-91	15	**106**	-21	30	**51**	-151	-59	**92**	-131	-60	**71**	-134	-65	**69**
1100	-134	4	**138**	-18	34	**53**	-158	-64	**94**	-133	-58	**75**	-135	-66	**69**
1200	-186	2	**188**	-21	31	**52**	-162	-81	**80**	-139	-58	**81**	-135	-66	**69**
1300	-230	-12	**218**	-21	24	**45**	-163	-94	**68**	-147	-59	**88**	-135	-72	**63**
1400	-221	-17	**204**	-24	19	**43**	-169	-115	**55**	-149	-64	**85**	-134	-88	**46**

Actuation (X) and measurement (M) locations:

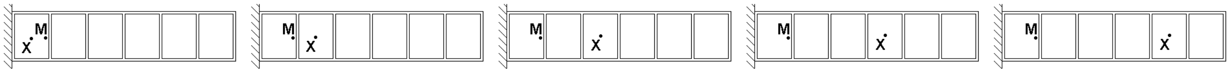

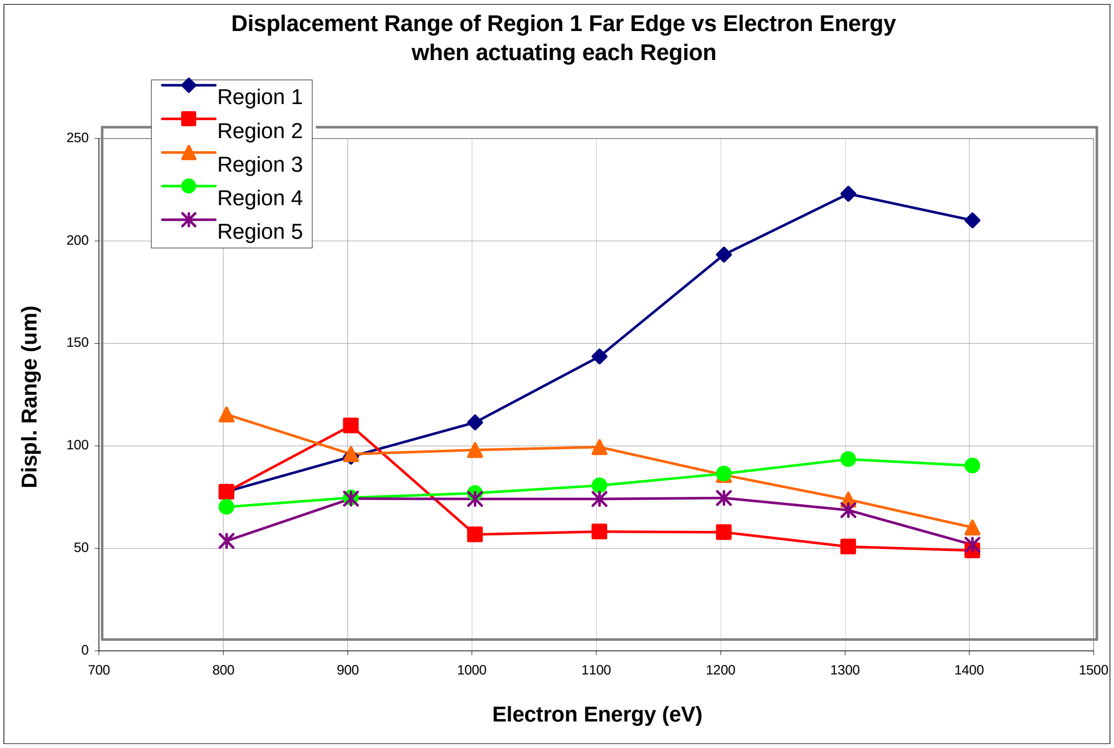

Figure 84. Displacement range vs electron energy for each region.

Actuation (X) and measurement (M) locations:

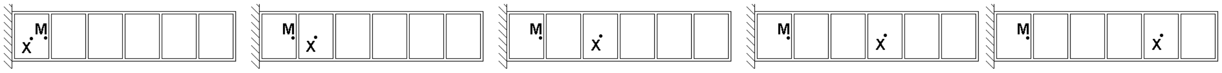

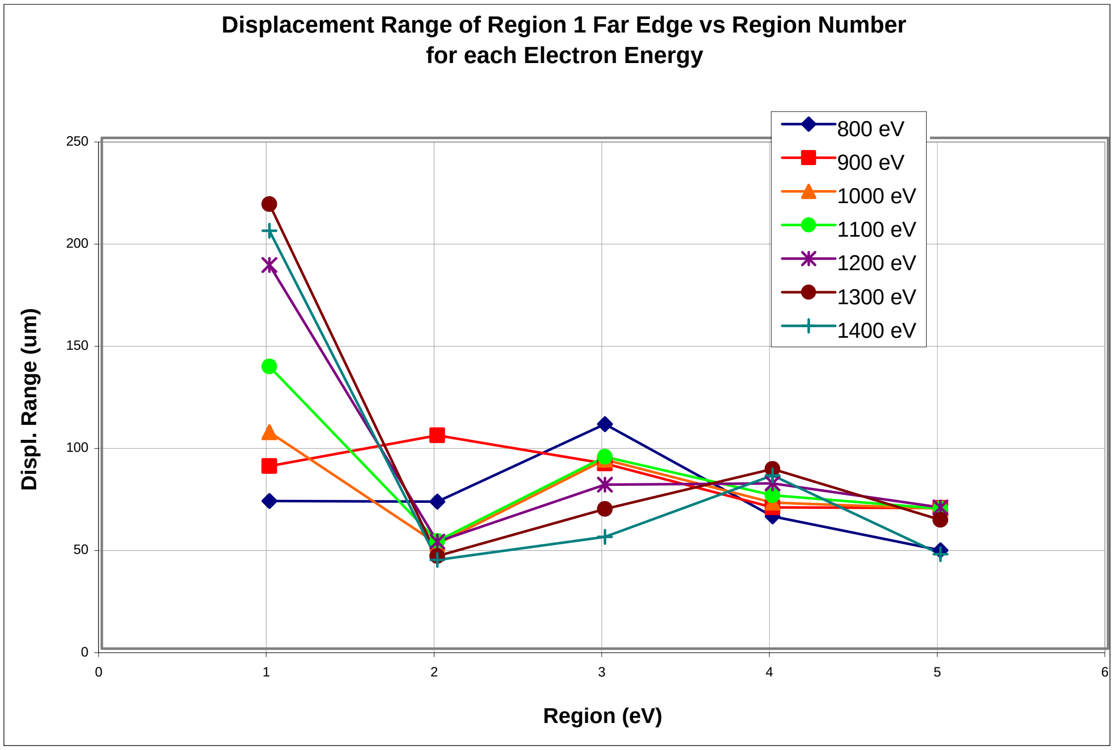

Figure 85. Displacement range vs region for each electron energy.

It is evident from these plots, particularly Figure 85, that the displacement of Point 1 is affected most by actuation of Region 1 directly. This first observation is the most obvious trend and is clearly to be expected. However, this is only the case after the electron energy exceeds 1000 eV, which is not necessarily to be expected. In fact, actuating Region 3 with 800-eV electrons seems to affect the displacement of Point 1 more than actuating Region 1 directly with 800-eV electrons.

This striking result is not the only unexpected result—the displacement of Point 1 seems to be influenced similarly by *all* regions; that is, for some energies, Region 5 has as much influence on the displacement of Point 1 as does Region 2. For 1000- to 1400-eV electron energies, Point 1 moved *more* when Region 5 was actuated than it did when Region 2 was actuated. This is counterintuitive for engineers who are used to linear systems in which superposition applies. If superposition were applicable, Region 2 would have a much greater influence on the displacement of Point 1 than would Region 5.

These results can be attributed to the primary electron distribution pattern in Figure 74. From Figure 85, it seems that the main peak in the diffraction pattern shifts as the electron energy changes. For example, the main peak for 800-eV electrons seems to occur not at Region 1 but ~22 mm away, at Region 3. The main peak for 900-eV electrons has shifted to occur at Region 2. All other energies have their main peak at Region 1 but seem to also have secondary peaks in other regions. For example, a secondary peak occurs at Region 3 for 1000- and 1100-eV primary electrons. The secondary peak for 1200-eV electrons occurs somewhere between Regions 3 and 4, while that for 1300- and 1400-eV electrons moves out even further to Region 4.

When considering how secondary electrons influence this data, it is helpful to compare this to electric field lines in a capacitor (see Figure 86). Here, an electron placed close to the plates will be more influenced by the electric field than will an electron placed far away.

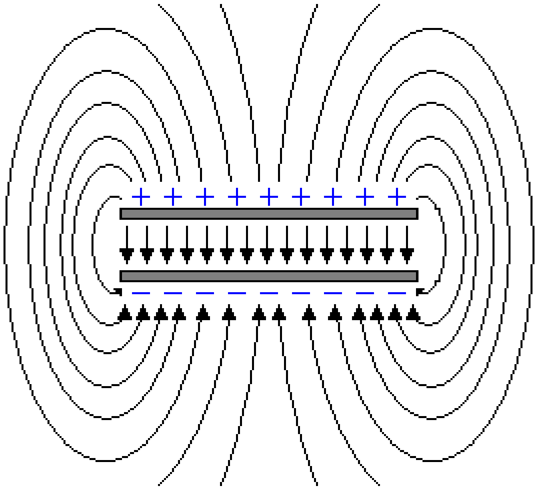

Figure 86. Electric field lines around a parallel-plate capacitor.

Consider now an electron on the surface of this capacitor that is given energy by an electron that strikes the surface. It will *not* follow the electric field lines. These lines show the path an electron will take if it is placed in this electric field *at rest*. However, it will follow a magnified version of this path because the only difference is that this electron has some initial kinetic energy. An electron leaving the surface will follow an even larger path. The distance a secondary electron travels without being intercepted depends on its kinetic energy when leaving the surface.

Consider the same situation, but now place an insulating block somewhere in this field (see Figure 87). The electric field lines do not change (assuming that no charge builds up on the surface).

An electron having energy in a certain range will follow the electric field lines that strike this insulating block. If the electron has too much or too little energy, it will miss the insulator. This is the same situation in which secondary electrons leaving the PVDF film find themselves. A secondary electron that leaves the center of Region 3 with a particular energy will follow the electric field lines until it is intercepted by an object, say Region 2. But another electron with a specific greater energy that leaves the same spot will travel further, striking Region 1.

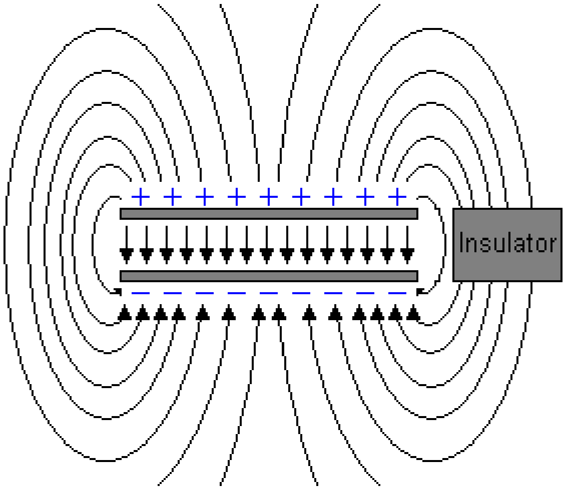

Figure 87. Electric field lines around parallel-plate capacitor with insulator in field.

Given an even distribution of electron energies leaving the center of Region 3, the probability of an electron striking Region 1 is equal to the probability of an electron striking Region 5 because it has equal surface area and is an equal distance away. Because they are closer to Region 3, Regions 2 and 4 are *more* likely to be struck by such electrons than are Regions 1 and 5.

This idea is the same as that used for radiation calculations—radiation leaving one surface and striking another surface depends on the incident body's surface area and distance from the source of the electromagnetic wave, as well as the electromagnetic field lines. This is also true of secondary electrons.

But the electrons leaving the center of Region 3 do not have an even distribution of energies. The secondary electron energies depend on the energies of the primary electrons striking the PVDF film. These primary electrons have a Gaussian distribution of energy, with the mean value as that proscribed by the control system, as discussed earlier in this report. Thus, the secondary electrons will also have a Gaussian distribution of energy, with the mean value considerably less than that of the primary electrons. So, a secondary electron leaving Region 3 may be more likely to reach Region 5 than to reach Region 4, based on its energy. Both the secondary and primary electrons influence the data shown in Figures 84 and 85.

Locations of Predictability

One goal of this research is to determine if piezoelectric thin films can be used for lightweight deployable mirrors. As such, it is helpful to get an idea of what the spatial resolution of such a mirror would need to be. Though the following data does not *determine* the spatial resolution of a piezoelectric thin-film mirror, it does indicate *possibilities* regarding spatial resolution.

Figure 88 shows the response of Point 1 to actuation of Region 4 with the indicated electron energies. Because it was decided earlier in this analysis that only electron energies above 1000 eV were desirable, the plots below are for 1100 to 1400 eV only.

Actuation (X) and measurement (M):

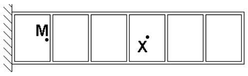

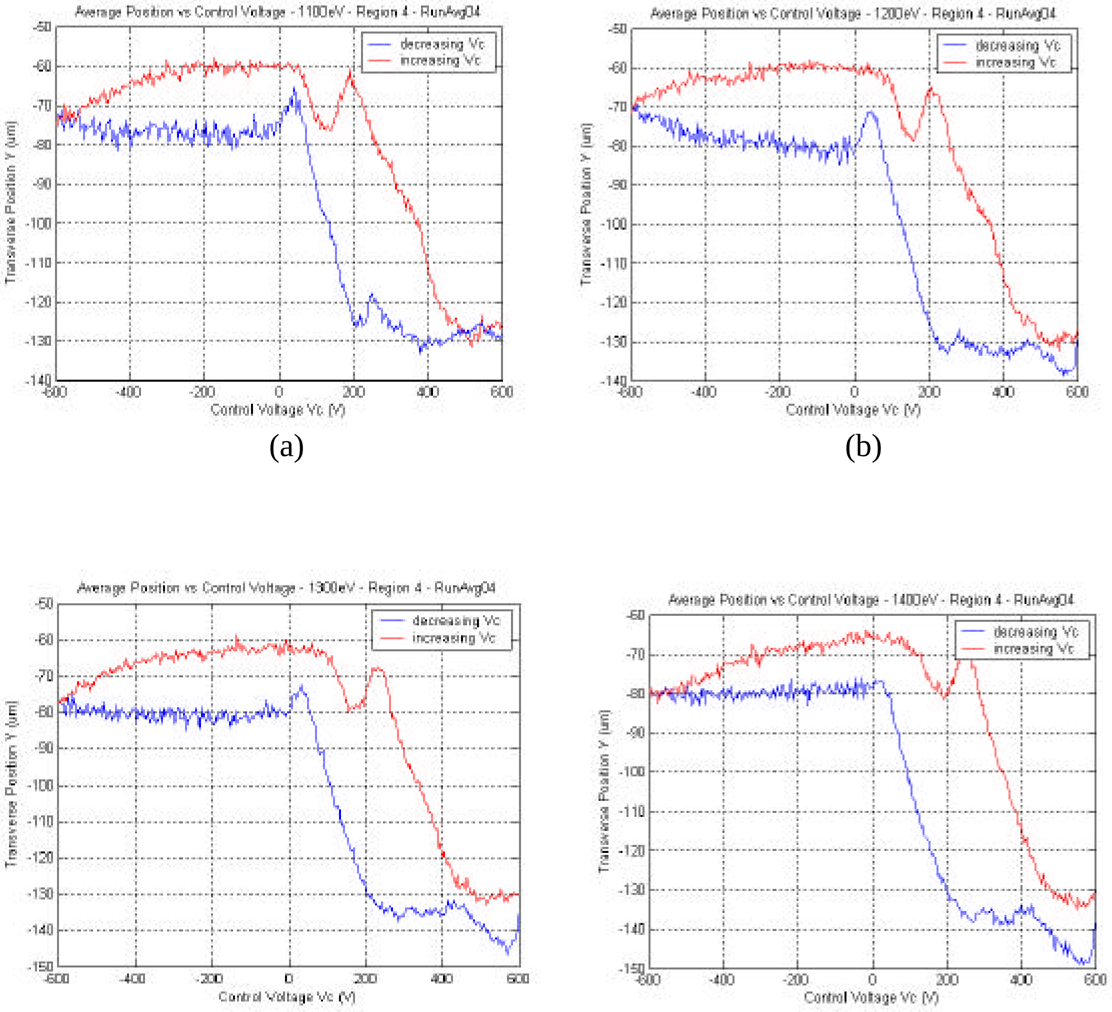

(a) (b)

(c) (d)

Figure 88. Displacement of Point 1 when actuating Region 4.

The most important aspect in all four plots is the response when negative control voltage is applied—it is quite small compared to the response when positive control voltage is applied. To see the range of motion of Point 1 when actuating each region with only negative control voltage, a table and plot were created (see Table 5 and Figure 89).

It is clear from Figure 89 that overall, Point 1 responds the most when Region 1 is actuated. Perhaps a more important finding, however, is that Point 1 responds the least for electron energies of 1100 to 1400 eV when Region 4 is actuated. It seems, in fact, that 1400 eV is the best electron energy to use for this purpose because it yields the greatest response (130 μm) to Region 1 actuation and the smallest response (19 μm) to Region 4 actuation. Using the distance between Region 1 and Region 4 (~33 mm), it is possible, then, to determine the optimum wavelength of light that could be focused with a mirror made of this material.

Table 5. Range of Motion of Point 1 When Actuating Only with Negative Control Voltage

	Region 1			Region 2			Region 3			Region 4			Region 5		
eV	min	max	range	min	max	range	Min	max	Range	min	max	range	min	max	range
			(μm)			(μm)			(μm)			(μm)			(μm)
1100	-53	4	**57**	-17	34	**51**	-129	-64	**65**	-82	-58	**24**	-113	-66	**47**
1200	-64	2	**66**	-21	31	**52**	-127	-81	**46**	-85	-58	**27**	-127	-67	**61**
1300	-100	-12	**88**	-20	24	**44**	-125	-94	**30**	-85	-59	**26**	-132	-72	**61**
1400	-146	-17	**130**	-23	19	**42**	-140	-115	**26**	-83	-64	**19**	-134	-89	**46**

Actuation (X) and measurement (M) locations:

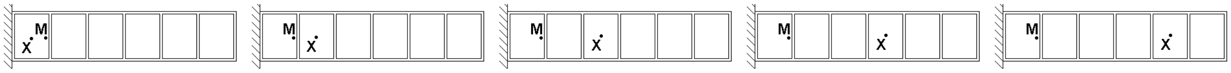

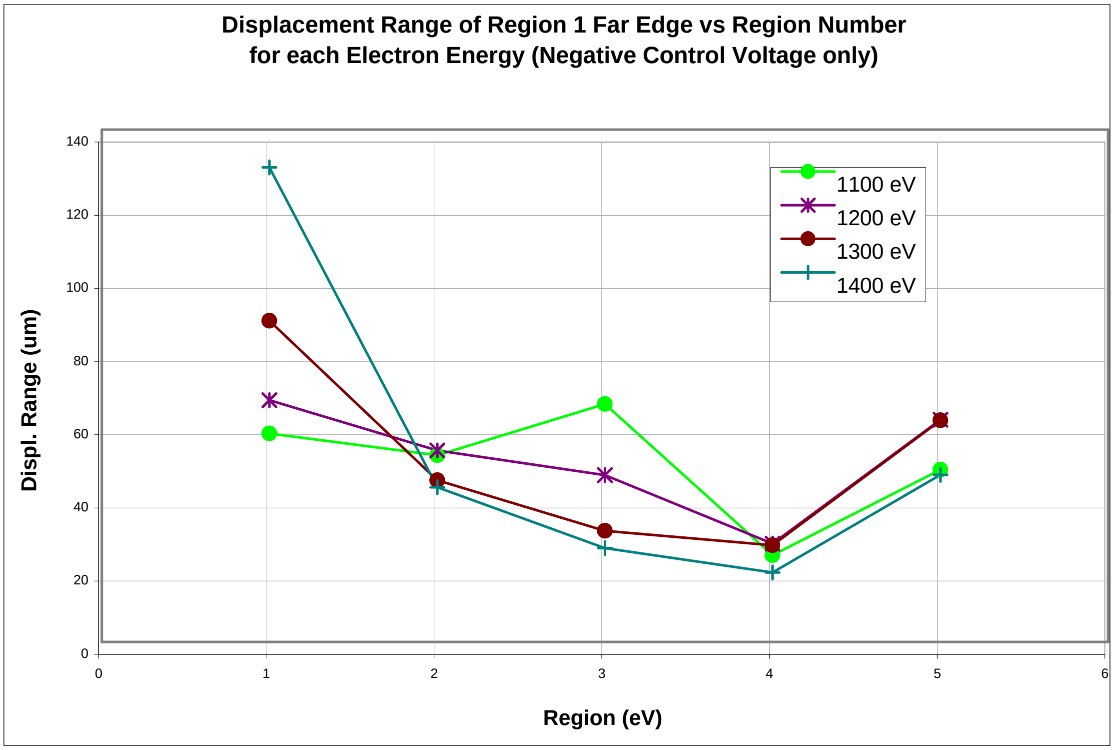

Figure 89. Range of motion of Point 1 when actuating only with negative control voltage.

It is useful to also compare the primary electron profile to the film response. The data for Figure 73 was found using the same model of electron gun (Kimball Physics EFG-7) as was used for the data in this research. According to Figure 73, the minimum number of primary electrons occur at a ring of radius ~25 deflection volts away from the central peak (here the electron energy was 400 eV). According to the data in Figure 89, the minimum film response occurs at approximately Region 4. The difference in x-deflection voltage between Region 1 and Region 4 for this experiment was 4.1–5.6 V for electron energies of 1000–1400 eV, respectively. At first glance, it seems that these results differ by a factor of ten. However, Figure 73 was created using a power supply that was first sent to a controller that had a built-in gain of 1/10 and then to the electron gun inputs, as verified by the creator of Figure 73, Dr. Hadinata. The maximum allowable deflection voltages into the electron gun were +/–10 V.

Thus the 25 deflection volts in Figure 73 actually occurred at 2.5 V. Now, considering a nearly linear relationship between electron energy and deflection voltage, the uncertainty in determining where the minimum number of electrons occurs, and the range of minimum film response, it follows that the minimum film response occurs where fewest primary electrons strike the film.

This result leads to a significant conclusion: given negative control voltage and electron energy between 1100 and 1400 eV, two locations have been discovered at which the film response is predictable. The first location is where the primary electron peak is focused—the response here has been predictable in previous works as well (Hadinata 2001), so this finding is not surprising. A more significant finding, however, is that *another* location has been found where film response is predictable. In this work, the location of predictability is ~33 mm away from where the primary electron peak is focused, where very little response occurs. In fact, because the region is 10 mm wide, there is a 10-mm-thick ring of predictability about the central focal point of average radius 33 mm. In previous works, such a location could not be found. It was previously believed that the uncertainty in response, attributed mainly to secondary electron emission, made predictability impossible. And for other experimental setups, that was indeed the case. This work has simply found a setup that allows the controller to know more locations of predictable response.

This predictability is indicative of another strong conclusion: secondary electron emission does not have a significant impact on film response at these locations of predictability. Indeed, the nature of secondary electrons is such that any influence by them on film response creates unpredictability. It follows, then, that predictability of film response indicates that secondary electrons influence the film response very little. Thus, any application using this setup need not utilize alternate methods of capturing secondary electrons (because the vacuum chamber is grounded, it may act as a secondary electron collector).

Conclusions

Electron gun control has been demonstrated to induce surface profile changes in PVDF structures at both a macroscale (optically) and a nanoscale. Data have shown macroscale deflections as large as 1.4 mm at 65 mm from the tip of the PVDF Type B cantilever bimorph. The PVDF Type D copolymer in the ring clamp had center displacements on the order of 200 nm.

Optimum energy levels to minimize hysteresis irregularities in the Type B bimorph behavior were found to be between 800 and 1200 eV. In addition, a breakdown in PVDF bimorph actuation appeared at 1400 eV. Actuation of the bimorph using negative control voltages also induced more nonlinearities in the 400- to 800-eV ranges than did positive control voltages.

Decay of electron gun control actuation after the electron beam was removed from the Type B bimorph was shown to be on the order of 10 μm in >5 seconds at 400 eV, and 10 μm in >1000 seconds at 1400 eV. The electric field in the Type B bimorph was shown to be uniform regardless of the application location of electrons. The Type A and B bimorphs were shown to function in closed-loop PID tip control. The Type B bimorph proved to have a faster response.

Controllability analysis has shown that stable control of the Type C bimorph is possible through the use of low-frequency (0.01 Hz), high-amplitude (500-V) changes or higher-frequency (1-Hz) low-amplitude (50-V) adjustments. The response lag was smaller for the lower-frequency control inputs than for the higher-frequency inputs. The following relationship was shown: higher currents induced the largest DC offsets and response amplitudes. Overall, the Type C bimorph responded best to high-current, low-frequency input. This minimized both the energy in the DC offset and the response lag and maximized the output amplitude response.

The following additional conclusions can be drawn from the data gathered in investigating the effect of focusing an electron gun on a thin film comprising multiple spatial regions.

When the region of interest is directly actuated, the PVDF film exhibits hysteresis, but that hysteresis becomes less pronounced as the electron energy increases to between 800 and 1400 eV. Despite the hysteresis, however, the film seems controllable because, at the higher electron energies, the hysteresis loops become tighter.

There is a charge-up effect when actuating the film and finding a hysteresis loop. Thereafter, the hysteresis loops are repeatable.

Edge effects play a significant role in the response of the film and focusing. Therefore mirror applications may need a rim of “inactive” material to avoid these end effects.

It is desirable to use electron energies >1000 eV where the response of the region of interest is greatest. At these energies, the response of other regions does not increase dramatically.

It is preferable to use only negative control voltage to get the desired response. When using only negative control voltage and electrons with energy >1000 eV, the response of Region 1 to actuation of Region 4 is minimal (~20 um) while other regions’ responses are typically at least double that amount. This leads to a ring of predictable film response with the center at the electron beam focal point, a radius of ~33 mm, and a thickness of ~10 mm. Such parameters could be used to determine the spatial resolution of a PVDF thin-film bimorph mirror.

The minimum film response occurs where fewest primary electrons strike the film. Given that, secondary electrons do not significantly contribute to film response.

Future Work

One limitation in performing this research was the inability to measure the whole contour of the film at once. Therefore, a new measurement system, specifically a Shack-Hartmann Wavefront sensor, could be incorporated for future research.

Further work includes the testing of a larger PVDF thin-film bimorph that would be preformed into a desired surface shape and size, then adjusted piezoelectrically to remove aberrations. Such testing would require new mounting and measurement techniques, as well as complicated algorithms of control. For example, a 0.5-m-diam spherically curved thin film, separated into individual regions as in the latter portion of this research, would increase the complexity of the control system by orders of magnitude.

Bibliography

Adelman, N. T., 1977, Spherical Mirror with Piezoelectrically Controlled Curvature, *Applied Optics*, Volume 16, Number 12, p. 3075.

Bell, K. D., R. Boucher, J. Leitner, M. Powers, E. C. Hackney, L. R. Robertson, and K. Schrader, 1998, UltraLITE Program Overview, Air Force Research Laboratory ULTRALITE Program Summary.

Bin-Nun, E., and F. Dothan-Deutsch, 1972, Mirror with Adjustable Radius of Curvature, *The Review of Scientific Instruments*, Volume 44, Number 4, p. 512.

Brown, P. H., and R. F. Sivyer, 1974, Cathode Ray Tube Acoustic Transducers, United States Patent #3,899,709, June.

Bruining, H., 1957, *Electronics and Waves Series: Physics and Applications of Secondary Electron Emission*, McGraw-Hill Book Company Inc., New York.

Clark, G., 1997, World’s Largest Mirror Cast By UA Scientists, *University of Arizona Daily Wildcat*, September 15.

Ealey, A. M., and J. A. Wellman, 1991, Deformable Mirrors: Design Fundamentals, Key Performance Specifications, and Parametric Trades, SPIE, *Active and Adaptive Optical Components*, Volume 1543, p. 36.

Feinleib, J., S. G. Lipson, and P. F. Cone, 1974, Monolithic Piezoelectric Mirror for Wavefront Correction, *Applied Physics Letters*, Volume 25, Number 5, p. 311.

Forbes, F., F. Roddier, G. Poczulp, C. Pinches, G. Sweeny, and R. Dueck, 1989, Segmented Bimorph Deformable Mirror, *Journal of Physics E: Scientific Instruments*, Vol. 22, pp. 402–405.

Freeland, R. E., G. D. Bilyeu, and G. R. Veal, 1996, Development of Flight Hardware for a Large, Inflatable-Deployable Antenna Experiment, *Acta Astronautica*, Volume 38, Numbers 4–8, p. 251.

Goldstein, J., H., and Yakowitz, 1977, Electron Beam – Specimen Interaction, *Practical Scanning Electron Microscopy*, Plenum Press, New York.

Hadinata, P. C., 2002. Strain Control of Piezoelectric Materials Using an Applied Electron Flux. Dissertation, University of Kentucky, College of Engineering.

Henson, T. D., J. C. Wehlburg, J. M. Redmond, J. A. Main, and J. W. Martin, 2001,Thin-Skin Deployable Mirrors for Remote Sensing Systems, Sandia National Laboratories Report, #SAND2001-0101, January.

Hubbard, J., 1992, Active Mirror Assembly, United States Patent #5,159,498, October 22.

Ikramov, A. V., S.V. Romanov, A. G. Roshchupkin, A. G, Safronov, and A. O. Sulimov, 1992, Bimorph Adaptive Mirror, *Soviet Journal of Quantum Electronics*, Volume 22, Number 2, p. 163.

Isaacson, W., 2001, A Day of Infamy, *TIME Magazine*, Special Issue, September 14.

Keck-Observatory, W. M., 1996, www2.keck.hawaii.edu:3636, General Information.

Kokorowski, S. A., 1979, Analysis of Adaptive Optical Elements Made of Piezoelectric Bimorphs, *Journal of the Optical Society of America*, Volume 69, Number 1, p. 181.

Koshida, N., and S, Yoshida, 1983, Secondary Electron Emissions from Polyvinylidene Fluoride (PVDF) Film, *Journal of Applied Physics*, Volume 22, Number 11, p. 1744.

Main, J. A., 1997a, Smart Material Control Without Wire Leads or Electrodes: New Methods and Devices, in *Conference Proceedings, ASME Design Engineering Technical Conferences*, held on September 14–17, Sacramento, CA. ASME Paper DETC97/VIB-3933.

Main, J. A., G. C. Nelson, and J. W. Martin, 1998b, Precise Maintenance of Inflated Structure Shape Using Electron Gun Controlled Piezoelectric Materials, in *Conference Proceedings, AIAA Structures, Structural Dynamics and Materials*.

Main, J. A., and G, C. Nelson, 2001, Smart Material Control System and Related Method, United States Patent #6,188,160, February 13.

Martin, J. W, 1998, Noncontact Shape Control of a Membrane Mirror, Masters Thesis, University of Kentucky, College of Engineering, December.

Martin, J.W., (2001). Non-contact Electron Gun Control of Piezoelectric Polymer Thin Film Structures. Dissertation, University of Kentucky, College of Engineering.

Martin, J. W., J. A. Main, J. M. Redmond, and T. D. Henson, 2001b, Large Aperture Space Based Optics, in *Conference Proceedings, Space and Missile Materials Symposium*, Monterey, California, June 24.

Martin, J. W., J. A. Main, J. M. Redmond, T. D. Henson, and R. D. Watson, 2001c, Electron Gun Controlled Smart Structure, United States Patent #6,297,579, October 2.

Mikoshiba, S., and B. Ahlborn, 1972, Laser Mirror with Variable Focal Length, *The Review of Scientific Instruments*, Volume 44, Number 4, p. 508.

NASA, 1994, The Natural Space Environment: Effects on Spacecraft, Publication 5-341-2, March.

Natori, M., H. Furuya, S. Kato, Y. Takesita, and T. Sakai, 1988, A Reflector Concept Using Inflatable Elements, in *Proceedings: 16th International Symposium on Space Technology and Science*, Sapporo, Japan, pp. 459–467.

Nelson, G.C., and J. A. Main, 2001, Non-contact Electron Gun Strain Control of Piezoceramics, *AIAA Journal*, Volume 39, Number 9, September, pp. 1808–1813.

Rapp, Donald, 1996, Prospects and Limitations of Technical Approaches for Ultra Lightweight Space Telescopes, *JPL Report* D-13975, September 30.

Rigaut, F., R. Arsenault, J. Kerr, D. Salmon, M. Northcott, Y. Dutil, and C. Boyer, 1994, The Canada-France-Hawaii Adaptive Optics Bonnette II: Simulations and Control, *SPIE*, Meeting 2001.

Sato, T., Y. Ueda, and O. Ikeda, 1981, Transmission-Type PVDF 2-D Optical Phase Modulator, *Applied Optics*, Volume 20, Number 2, p. 343.

Space Imaging Inc., 1999, www.spaceimaging.com/aboutus/satellites/ikonos/ikonos.html, IKONOS Statistics.

Steinhaus, E., and S. G. Lipson, 1979, Bimorph Piezoelectric Flexible Mirror, *Journal of the Optical Society of America*, Volume 69, Number 3, p. 478.

Susini, J., D. Labergerie, and L. Zhang, 1994, Compact Active/Adaptive X-Ray Mirror: Bimorph Piezoelectric Flexible Mirror, *The Review of Scientific Instruments*, Volume 66, Number 2, p. 2229.

Tzou, H. S., 1989, Development of a Light-Weight Robot End-Effector Using Polymeric Piezoelectric Bimorph, in *Proceedings: IEEE International Conference on Robotics and Automation*, pp. 1704–1709.

Utku, S., C, F, Kuo, J. A. Garba, and B. K. Wada, 1995, Shape Control of Inflatable Reflectors, *Journal of Intelligent Material Systems and Structures*, Volume 6, July, p. 550.

Whetten, N. R., 1981, Secondary Electron Emission, *CRC Handbook of Chemistry and Physics*, 62nd Edition, CRC Press, Inc., pp. E373-E374.

Distribution:

1	MS0972	Andy Boye, 05710
1	MS0972	Tammy Henson, 05712
1	MS0570	Jody Smith, 05712
5	MS0968	Jeffrey Martin, 05714
5	MS0968	Benjamin Macke, 05714
1	MS0968	Dan Schmitt, 05714
1	MS0971	Dennis Miller, 05730
1	MS1205	Sidney Gutierrez, 05900
1	MS0847	Hal Morgan, 09120
5	MS0893	Pavel Chaplya, 09123
1	MS0893	John Pott, 09123
1	MS0847	Jim Redmond, 09124
5	MS1310	Jordan Massad, 09124
5	MS1310	Anton Sumali, 09124

5
John Main
Department of Mechanical Engineering
Mechanical Building
University of Kentucky
Lexington, Kentucky 40508

2
Jennifer Graham
Technically Write
9524 Palomas NE
Albuquerque, NM 87109

1	MS9018	Central Technical Files, 8945-1
2	MS0899	Technical Library, 09616
1	MS0323	LDRD Office, 01011